Optical and ultrasonic methods for the detection of dental disease

A thesis submitted to

The Department of Bioengineering

University of Strathclyde

for the degree of

Doctor of Engineering

by

David Allan Hughes

September 2011

Declaration of author's rights

This thesis is the result of the authorâs original research. It has been composed by the author and has not been previously submitted for examination which has led to the award of a degree.

Signed:

Date:

"May all we do be all for our delight" - Erik Petersen

Acknowledgements

First and foremost I would like to thank my wife Lisa-Marie for the continued personal and emotional support through the completion of this research project. I also send my gratitude and thanks for the support given to me by my immediate family and close friends.

I would also like to thank my supervisors John and Sandy for the huge contribution of guiding me through this body of work. I also recognise the staff and students at the Institute of Photonics and DTC in Medical Devices for their help. I also acknowledge the contribution of Chris Longbottom and Valerie Smith at the University of Dundee in preparing dental samples for this work.

I would like to extend thanks to Scott, Dave, Simon, Caroline, Jonathan, Untzizu and Amanda for their continued friendship that started at the University of Strathclyde. And finally, I would not have been able to complete this work without the continued personal and musical support of my band, which kept me sane during the hours that were spent outside of the lab.

Abstract

This thesis reports on an investigation into detecting two types of dental disease with light and sound. Dental caries is the localised demineralisation of dental enamel through the acidic by products of bacteria. If detected at an early stage, this disease is reversible. Dental acid erosion is the irreversible loss of dental material by an acidic environment, such as that in the mouth after consumption of fizzy drinks.

Currently the most common tools that the dentist uses for the detection of these diseases are a sharp metal probe, visual inspection and X-rays. All three of these techniques are subjective and in the case of dental erosion, are hampered by the lack of a suitable reference point on the tooth surface. The early stages of dental caries manifest as subsurface lesions, which are unable to be quantitatively detected using these methods.

In the first part of this work, we report on the development of a fibre optic confocal microscope which makes use of miniature optics in order to record depth profiles through the tooth surface. A technique known as Principal Component Analysis (PCA) is then used to compare these depth profiles to a known set of depth profiles in order that a diagnosis can be made.

An optical resolution of 19.58μm was achieved, allowing for the detection of early caries lesions. A set of excised teeth were used to test the system, and PCA gave a sensitivity and specificity of 0.96 and 0.9 respectively

The latter part of the work reports on a novel high frequency focussed ultrasound transducer as being suitable for measuring the thickness of the enamel layer to within 10% of the total enamel layer thickness. This device was also shown to be useful for the imaging of early caries lesions.

Contents

1 Introduction **1**

1.1 Introduction 2

1.2 Published work 5

1.2.1 Papers 6

1.2.2 Proceedings 6

1.2.3 Refereed Meeting Presentations 6

2 Teeth and dental disease **10**

2.1 Introduction 11

2.2 Teeth 11

2.2.1 Enamel 12

2.2.2 Dentine 13

2.2.3 Other components of the tooth 13

2.3 Introduction to dental disease 14

2.3.1 Dental caries 14

2.3.2 Acid erosion 20

2.4 Conclusions 24

2.4.1 Requirements for a diagnostic device 25

3 Optical techniques for dentistry **34**

3.1 Introduction 35

3.2 The nature of light 35

3.3 Optical properties of dental tissues 38
3.3.1 Reflection 39
3.3.2 Scattering 39
3.3.3 Absorption and fluorescence 41
3.4 Current optical techniques 43
3.4.1 Optical coherence tomography 43
3.4.2 Fluorescence based technologies 44
3.4.3 Fibre optic trans-illumination (FoTI) 46
3.4.4 Absorption spectrophotometry 46
3.5 The need for a new technology 47
3.6 Microscopy 49
3.6.1 Resolving Power 53
3.6.2 The confocal microscope 55
3.6.3 Summary 61
3.7 Fibre optic confocal microscopy 62
3.7.1 Single mode fibre as a pinhole 62
3.7.2 Application to dental disease 65
3.7.3 A fibre optic system for the detection of dental disease . . 66

4 Micro-optics for the oral cavity 73

4.1 Introduction 74
4.2 Traditional Lenses 74
4.3 Aspheric Lenses 75
4.4 GRIN lenses 77
4.4.1 GRIN Profile 77
4.4.2 Pitch 78
4.4.3 Ray Tracing 79
4.4.4 Computer simulation 83
4.5 Experimental characterisation of lenses 86

4.5.1 Results 89
4.6 Discussion 97
4.7 Conclusions 100

5 Principal Component Analysis 103
5.1 Introduction 104
5.2 Principal components 104
5.2.1 Mathematics 106
5.2.2 Principal components of real data 107
5.2.3 Covariance Matrix 108
5.2.4 Computing eigenvectors and eigenvalues of C 109
5.2.5 Making sense of the new set of axes 111
5.2.6 Recap 112
5.3 Applications of PCA 113
5.4 Example: Using PCA to segment an Ultrasound Image 115
5.5 Conclusion 122

6 FOCOM for the detection of caries 126
6.1 Introduction 127
6.2 Methodology 128
6.2.1 FOCOM 129
6.2.2 Principal component analysis 130
6.2.3 Dental samples 131
6.3 Results 132
6.4 Discussion 135
6.4.1 Reference scan set 135
6.4.2 Test scan set 140
6.5 Conclusions 141

7 Ultrasound and dentistry 144

7.1 Introduction . . . 145

7.2 Ultrasonic waves . . . 145

7.2.1 Ultrasonic propagation . . . 146

7.2.2 Ultrasonic pulses . . . 147

7.3 Imaging considerations . . . 148

7.3.1 Resolution . . . 149

7.3.2 Signal to noise ratio . . . 150

7.4 Transducers and the generation of ultrasound . . . 151

7.4.1 Ultrasound system . . . 153

7.5 Ultrasound as a diagnostic tool . . . 153

7.6 Ultrasound behaviour in dental materials . . . 155

7.7 Ultrasound as a diagnostic technique in dentistry . . . 157

7.7.1 Introduction . . . 157

7.7.2 Early work . . . 158

7.7.3 Mid-work . . . 159

7.8 Current developments . . . 160

7.9 Summary . . . 163

8 High frequency ultrasound and dental erosion 172

8.1 Introduction . . . 173

8.2 High frequency transducer and advantages . . . 174

8.3 Experimental method . . . 176

8.3.1 Signal processing . . . 179

8.3.2 B-scan and Water fall plots . . . 181

8.3.3 Sequential Grind and Image technique . . . 182

8.3.4 Thickness from A-scan data . . . 183

8.3.5 Caries investigation methodology . . . 184

8.4 Results and Discussion . . . 185

8.4.1 Enamel Thickness Results 185
8.4.2 3D imaging results 192
8.4.3 Caries results 192
8.5 Conclusions 198

9 Conclusions and Further Work 203
9.1 Research Outcomes 206
9.2 Further developments 207

10 Appendix 1: GRIN simulation C code 211

Chapter 1

Introduction

1.1 Introduction

In 1728, Pierre Fauchard pioneered modern dentistry with his text entitled "The surgical dentist". In this book, Fauchard described how a dentist should verbally greet their patients, and also how they should stand to operate to maximise visibility. It can therefore be hypothesised that, as long as there have been people practising dentistry, they have been using light and sound for the detection, diagnosis and treatment of dental complaints.

As civilisations spread and lifestyles changed through the centuries, the range of dental problems encountered by a clinician would increase. One would expect that the range of tools to deal with these problems would also improve with technological advances and discoveries. However, if one was to compare the tools in common use in a modern dental clinic with those described by Fauchard in 1728, they would notice a large amount of similarities between the array of pliers, screws and drills described.

That is not to say that the field of dentistry has been completely stuck in the dark ages in terms of the tools available. The dental drill has also undergone extensive improvements over the centuries, from the crude implements used by neolithic tribes (Coppa et al., 2006) to the electric and air powered models in common use now. Laser technologies have also be introduced to the dental clinic as methods of removing diseased dental tissues (Featherstone and Fried, 2001), and not to mention the growth in the cosmetic market.

Preventative dentistry however has not had such a growth. The dentist still mainly relies on using his eyes and a metal probe known as an explorer in order to detect dental disease (Hall and Girkin, 2004). The discovery of X-rays did however give rise to a new technique for observing the inner structure of teeth, albeit in a method that exposed the patient to ionising radiation. There has been much work carried out over the last decades into new technologies for detecting dental disease, however, the lack of an established quantifiable and safe tool shows

that there is still work to be done (Pretty, 2006; Hall and Girkin, 2004).

This forms the motivation for this body of work. In this thesis the modalities of light and sound shall be investigated as methods for detecting different types of dental disease. The dental diseases that will be investigated are that of dental caries and dental erosion. Both diseases are widespread amongst the world's population and neither have an established quantifiable tool available for their detection. Dental caries, commonly known as tooth decay, is the localised demineralisation of tooth material through the acidic by-products of bacterial activity (Selwitz et al., 2007). If it is detected in its earliest form, dental caries can be treated. Dental erosion is the irreversible progressive thinning of the tooth materials through non-bacteria mediated action (Amaechi and Higham, 2005). This could be through exposure to acidic liquids (such as fizzy drinks) or environments (Jarvinen et al., 1991). The biggest problem in monitoring dental erosion is the lack of a suitable reference point on the tooth surface for measuring the thickness of the enamel. Both diseases shall be discussed in the following chapter in order to lay groundwork before introducing the optical and ultrasonic techniques.

After teeth and dental diseases have been introduced and discussed, attention shall be turned to developing a miniature optical system for the detection of dental caries. The system is based on a confocal microscope system, except that the pinhole has been replaced by a single mode fibre. Such a system has already been shown to be useful for detecting dental caries (Rousseau et al., 2007), however, the reported system made use of bulk optics to record high resolution depth profiles.

This work concentrates on the miniaturisation of the optics by investigating GRIN and aspheric lenses for the purpose, before deciding on using aspheric lenses. In order to compare the two lenses, a computer simulation is written that models ray propagation through a GRIN lens. While this is a common place method, much of the literature concerns itself with using the GRIN lens for

imaging from multi-mode fibres. In this simulation, the GRIN lens is assessed for its axial and lateral resolution when coupled to a single mode optical fibre. This simulation was subsequently verified with an experimental set up. The aspheric lens is experimentally characterised in a similar set-up to the GRIN lens and found to have a higher resolution capability. However, the resolutions obtainable with the reduced miniature lenses are lower in comparison with the previously reported system and therefore a new method of analysing the data is required.

For this purpose, this work introduces the application of principal component analysis (Joliffe and Morgan, 1992) for analysing the one dimensional fibre optic confocal microscope (FOCOM) data. Principal component analysis is a form of eigen-decomposition whereby a large data set, for example that which makes up a single FOCOM scan (over several thousand data points), is reduced to a much smaller dimension vector. This vector is derived from the similarities of a known set of FOCOM scans (in this case these scans are from healthy enamel) and allows the computer to determine whether or not a new FOCOM scan is of the same characteristics as a FOCOM scan from a healthy area of enamel.

After this technique has been established, a study is carried out using excised teeth in order to demonstrate the system as a method of detecting inter-proximal lesions in a safe and non-invasive manner. In this study, a fibre optic confocal microscope operating in the near infrared is constructed utilising the miniature aspheric lenses investigated previously. A set of reference scans from health and lesioned teeth are recorded and the principal component model is derived from these. Afterwards, a different set of scans from sound and lesioned teeth are recorded and these are compared to the model. It is shown that principal component analysis is able to differentiate between scans of healthy enamel and scans of lesioned enamel. This has implications for creating a device that is able to detect lesions on areas of the tooth that are difficult to visually inspect, such as in the inter-proximal region.

The rest of this thesis is devoted to a short investigation into using high frequency ultrasound primarily for the detection of dental erosion. Ultrasound has been investigated as a diagnostic tool for dentistry since the mid 1960's, however, a clinical tool has still to emerge (Ghorayeb et al., 2008). Previous reports have shown that it is possible to measure the thickness of enamel layers using ultrasound, but the resolution of the systems have shown to be the limiting factor in the measurements (Huysmans and Thijssen, 2000). There have been reports into using scanning acoustic microscopy at higher frequencies for characterising dental tissues (Peck et al., 1989), however, this work incorporates destructive sample preparation which reduces its applications in the clinic. The work presented here uses a novel focussed high frequency (35 MHz) ultrasound transducer to produce B-scan images of dental samples in order to bridge this gap. The thickness measurements taken from this data set are shown to agree with the gold standard technique of sequential grinding and imaging.

Another set of B-scan images were recorded using the novel transducer in order to investigate its use as a method of imaging early dental caries. Excised teeth that exhibited caries lesions were submerged in water and B-scans were recorded. As expected, the caries lesions showed up in the recorded images as areas of decreased reflection intensity due to the lower acoustic impedance of the lesion compared to the healthy enamel (Lees et al., 1970). This shows promise for using the high frequency transducer in a non-invasive array based diagnosis device.

1.2 Published work

The majority of the main results from this investigation have appeared in refereed publications. A list is now presented.

1.2.1 Papers

- D.A. Hughes, J.M. Girkin, S. Poland, C. Longbottom, T.W. Button, J. Elgoyhen, H. Hughes, C. Meggs and S. Cochran, *"Investigation of dental samples using a 35 MHz focussed ultrasound piezocomposite transducer"*, Ultrasonics, 49(2), February 2009, Pages 212-218

1.2.2 Proceedings

- D.A Hughes, S. Poland, C. Longbottom, S. Cochran, JM Girkin, *"A fibre optic system for the detection of dental caries"*, Journal of Medical Devices 3(2), Minneapolis, USA, April 2009

- D.A. Hughes, T.W. Button, S. Cochran, J. Elgohoyen, J.M. Girkin, H. Hughes, C. Longbottom, S. Poland, S. Sundaresh, *"5B-2 3D Imaging of Teeth Using High Frequency Ultrasound"*, Ultrasonics Symposium, IEEE, November 2007, pages 327-330, 10.1109/ULTSYM.2007.92

1.2.3 Refereed Meeting Presentations

- D.A Hughes, S. Poland, C. Longbottom, S. Cochran, J.M Girkin, *"A fibre optic system for the detection of dental caries"*, Poster presentation, Design of Medical Devices conference, Minneapolis, USA, April 2009

- D. Hughes, *"The whole tooth: Shining a light on tooth decay"*, IONS 5: Barcelona, Optical Society of America, February 2009

- D.A. Hughes, *"A fibre optic system for the detection of dental caries"*, University of Strathclyde Research Presentation Day, January 2009

- J.M. Girkin, T.W. Button S. Cochran, J. Elgohoyen, D.A. Hughes, H. Hughes, C. Longbottom, S. Poland, S. Sundaresh, *"NDT: Novel diagnostics for teeth"*, Invited Plenary talk at BiNDT 2007, Glasgow

Bibliography

B T Amaechi and S M Higham. Dental erosion: possible approaches to prevention and control. *Journal of Dentistry*, 33(3):243–52, March 2005. ISSN 0300-5712. doi: S0300-5712(04)00164-2. URL `http://www.ncbi.nlm.nih.gov/pubmed/15725524`. PMID: 15725524.

A. Coppa, L. Bondioli, A. Cucina, D. W. Frayer, C. Jarrige, J. - F. Jarrige, G. Quivron, M. Rossi, M. Vidale, and R. Macchiarelli. Palaeontology: Early neolithic tradition of dentistry. http://www.nature.com/nature/journal/v440/n7085/pdf/440755a.pdf, April 2006. URL `http://www.nature.com/nature/journal/v440/n7085/pdf/440755a.pdf`.

J. D. B. Featherstone and D. Fried. Fundamental interactions of laserswith dental hard tissues. *Medical Laser Application*, 16(3):181–194, 2001.

S.R. Ghorayeb, C.A. Bertoncini, and M.K. Hinders. Ultrasonography in dentistry. *Ultrasonics, Ferroelectrics and Frequency Control, IEEE Transactions on*, 55 (6):1256–1266, 2008. ISSN 0885-3010. doi: 10.1109/TUFFC.2008.788.

A. Hall and J. M. Girkin. A review of potential new diagnostic modalities for caries lesions. volume 83, pages 89–94. IADR, 2004.

M. C. D. N. J. M. Huysmans and J. M. Thijssen. Ultrasonic measurement of enamel thickness: a tool for monitoring dental erosion? *Journal of*

Dentistry, 28(3):187–191, March 2000. doi: 10.1016/S0300-5712(99)00063-9. URL http://www.sciencedirect.com/science?_ob=ArticleURL&_udi=B6T86-3YF3VVT-4&_user=10&_rdoc=1&_fmt=&_orig=search&_sort=d&_docanchor=&view=c&_searchStrId=961701155&_rerunOrigin=scholar.google&_acct=C000050221&_version=1&_urlVersion=0&_userid=10&md5=7ac35eaf65033607698819f1a9324706.

V. K. Jarvinen, I. I. Rytomaa, and O. P. Heinonen. Risk factors in dental erosion. *J Dent Res*, 70(6):942–947, June 1991. URL http://jdr.iadrjournals.org/cgi/content/abstract/70/6/942.

IT Joliffe and Bjt Morgan. Principal component analysis and exploratory factor analysis. *Statistical Methods in Medical Research*, 1(1):69–95, March 1992. doi: 10.1177/096228029200100105. URL http://smm.sagepub.com/cgi/content/abstract/1/1/69.

S. Lees, F Barber, and R Lobene. Dental enamel: Detection of surface changes by ultrasound. *Science*, 169(3952):1314–1316, September 1970. doi: 10.1126/science.169.3952.1314. URL http://www.sciencemag.org/cgi/content/abstract/169/3952/1314.

S.D. Peck, J.M. Rowe, and G.A.D. Briggs. Studies on sound and carious enamel with the quantitative acoustic microscope. *Journal of Dental Research*, 68(2):107–112, February 1989. doi: 10.1177/00220345890680020201. URL http://jdr.sagepub.com/cgi/content/abstract/68/2/107.

I. A. Pretty. Caries detection and diagnosis: Novel technologies. *Journal of Dentistry*, 34(10):727–739, 2006.

C. Rousseau, S. Poland, J. M. Girkin, A. F. Hall, and C. J. Whitters. Development of Fibre-Optic confocal microscopy for detection and diagnosis of dental caries. *Caries Research*, 41(4):245, 2007.

R. H Selwitz, A. I Ismail, and N. B Pitts. Dental caries. *The Lancet*, 369(9555):51–59, 2007. doi: 10.1016/S0140-6736(07)60031-2. URL http://www.sciencedirect.com/science/article/B6T1B-4MRGVD0-13/2/73cdc9abd2a8177a4bdf4445b6d2dee9.

Chapter 2

Teeth and dental disease

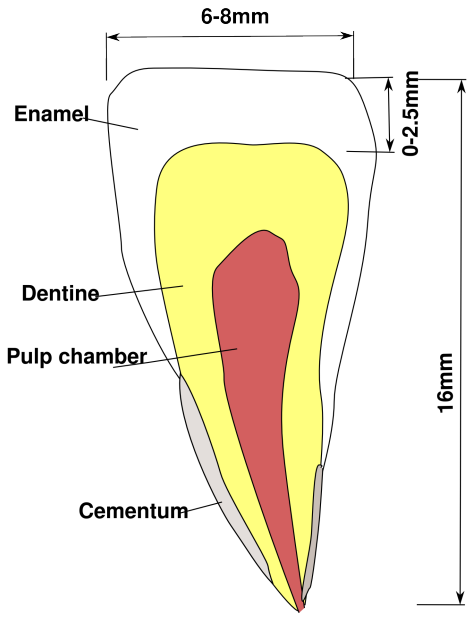

Figure 2.1: The tooth and its constituent materials

2.1 Introduction

In this chapter the biological properties and structure of the tooth will be discussed. The tooth is at the centre of this body of work and therefore it is important that a full understanding of its properties is appreciated. With this knowledge it is then easier to introduce the concepts of disease in the dental tissues and also the current methods of diagnosis and monitoring.

This chapter will start with an introduction to teeth and the materials that they comprise, and then discuss the two diseases that this thesis investigates, dental caries and acid erosion. A more detailed discussion of the optical and ultrasonic properties will be given in the chapters reporting those investigations.

2.2 Teeth

According to Dorland's Medical dictionary for Healthcare Professionals, a human has 20 primary (or deciduous teeth) which are replaced in later life by 32 permanent teeth. The primary function of teeth is for the preparation of food for

the journey through the digestive system, although they are also used in communication (both oral and visual) and aesthetics. Thus, with health and social implications, it is very important for teeth to be taken care of. Teeth are arranged in a semi-circular arrangement in the upper and lower jaws with teeth of similar function grouped together (incisors for cutting, molars for crushing) in areas optimal for their task. As shown in Figure 2.1, the tooth comprises three calcified materials (enamel, dentine and cementum) and a central chamber of connective tissue (the pulp). The enamel and the dentine shall be discussed in detail, with a brief note on the other structures to follow.

2.2.1 Enamel

Enamel is a crystal structure and is the hardest material in the human body. As a material it is transparent in nature with the greyish-white or yellowish appearance coming from the underlying dentine. While enamel is noted for its hardness, it is also susceptible to breakdown from acidic environments. The latter will be discussed in more detail when considering acid erosion as a disease.

The structure comprises elongated hexagonal hydroxyapatite crystals, around 25nm across and 100nm long, in a collagen based matrix (Habelitz et al., 2001; Meckel et al., 1965). The crystals group together to form "prisms" which spread out from their base at the dentine surface (Habelitz et al., 2001). The prisms are separated by organic fluids and materials. It is these separations that facilitate the transfer of nutrients from the external environment into the tooth in order to keep the tooth healthy and functional.

In total, the enamel of the tooth is 92-96% inorganic matter (the hydroxyapatite crystals), 1-2% organic matter (the collagen matrix), and 3-4% water (Habelitz et al., 2001). The density of enamel is around 2.8-3.0g/cm^3. The structure and make up of the enamel allows it to be the hardest material in the human body (Habelitz et al., 2001). However, it should be noted that enamel is also

very brittle (Meckel et al., 1965) owing to its high elastic modulus and low tensile strength (Habelitz et al., 2001).

2.2.2 Dentine

The dentine material is a softer material, with a density of around 2.1g/cm^3, and has a yellowish appearance. Dentine is not an amorphous material but is comprised of dentine tubules which spread out from the pulp chamber, up to a few mm in length. The tubule structure of dentine is important as it allows nutrients to be transported from the pulp to the dentine and enamel. The surroundings of these tubules also comprise hydroxyapatite crystals in a collagen matrix. Dentine, in total, is 70% inorganic material, 18% organic material, and 12% water (Habelitz et al., 2001). It is the lower inorganic component which makes dentine a softer and less brittle material than enamel.

2.2.3 Other components of the tooth

While it is the enamel and dentine which are of prime interest in this work, it is helpful to mention briefly the remaining tissues. The dentine material encases the softer pulp cavity where the blood vessels and nervous tissue are located. As one travels down the tooth from the crown towards the root, the enamel becomes progressively thinner until it reaches the dentine layer. Instead of exposed dentine, the root includes a hard outer layer known as cementum. It is to the cementum that the ligaments which hold the tooth in the gum and jaw are attached. If the enamel and dentine layers are breached, then damage to the internal components can occur. This is when pain and lasting damage can occur, therefore it is important to help the enamel and dentine to remain sound. What now follows is a discussion on the two main diseases to affect the enamel and dentine: cycle and erosion.

2.3 Introduction to dental disease

From a first glance, the tooth may seem like a lifeless hard object, however, this is not the case. The tooth is always undergoing chemical interactions which should keep it healthy and functional. However, as with all biological materials, external issues can disrupt these interactions and cause disease leading to loss of function and where nerves are present, pain. The tooth is no different and in this section two such events will be discussed, dental caries and acid erosion.

2.3.1 Dental caries

The enamel and dentine are continuously going through a demineralisation and remineralisation cycle which keeps the tooth healthy and strong. It is when this cycle goes out of balance that dental caries, or more commonly tooth decay, occurs. Dental caries is the localised destruction of the enamel and dentine tissue by the waste products of bacterium (Selwitz et al., 2007). What follows is a description of the pathology of the disease and current methods of detection and diagnosis.

Dental Caries pathology

The tooth is a functional object utilised in part for digestion. After consumption, remnants of foods are still present in the mouth, collecting on the tooth surface. Plaque, which is an organic biofilm composed of a mixture of bacterium, forms over the surface of the tooth. Certain bacteria in the plaque feed on the sugary components of the food remnants, producing acidic waste. This waste lowers the local environmental pH of the tooth surface, and if this drops to around 4.6, the enamel starts to dissolve. This occurs on the surface of the enamel to start with, and the dissolved enamel then re-mineralises producing a semi permeable cap on the lesion. If left untreated, the lesion grows with more and more material being

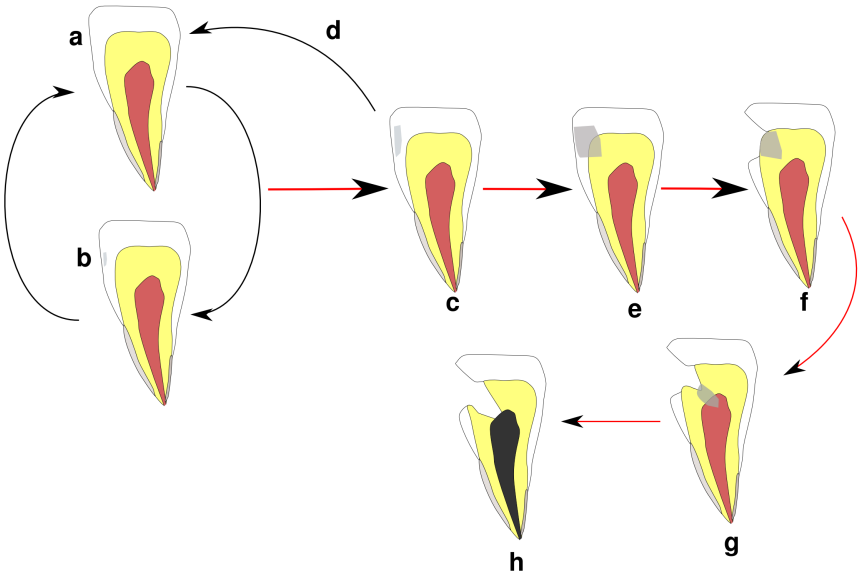

Figure 2.2: The dental caries cycle

lost at a subsurface level and also at a higher rate than can be re-mineralised. This is when a lesion is said to be 'active'.

After a while a cavity can occur when the cap over the lesion is breached. The lesion also can propagate in a similar fashion through the dentine, resulting in a hole straight through to the pulp and nerve. This is when pain arises.

An alternative scenario takes place if the biofilm is removed during the early stages of the caries lesion. By removing the biofilm, more nutrients (such as fluoride) can diffuse through the enamel surface. This improves the chances of the lesion re-mineralising and thus the material rebuilding, albeit with an altered structure. If the lesion is observed to be being re-mineralised or reducing in size, it is said to be 'arrested'. This cycle is shown diagrammatically in Figure 2.2.

Epidemiology and Aetiology of Dental Caries

While it is agreed that dental caries is a common complaint, there is a debate to whether dental caries is pandemic or epidemic in nature (Edelstein, 2006). The word epidemic comes from the Greek roots for "upon" and "the people", whereas pandemic refers to a disease that is upon all the people. The prevalence

of caries has been investigated many times, and while most works agree that it is a major problem, the characterisation between epidemic and pandemic remains to be solidified.

When comparing the epidemiology of dental caries between different countries the problem of subjectivity in the diagnosis arises. Different researchers use varying scales for characterising dental caries (Selwitz et al., 2007; Marthaler, 2004). One method of quantifying their prevalence is to use the Decayed Missing and Filled Teeth (DMFT) index of severity (Al-Sadhan, 2006; Edelstein, 2006; Marthaler, 2004). Using random sampling techniques, the DMFT value can be inferred to produce a percentage prevalence for the population.

A World Health Organisation bulletin found that while 60-90% of school children present dental caries, it is 'virtually universal' amongst adults (Petersen et al., 2005). More localised studies from countries around the world present similar figures, for example in the USA dental caries is the most common chronic disease of childhood (with a prevalence that is five times that of asthma) (Selwitz et al., 2007).

European figures are similarly high but, according to one review, showing a declining trend (Marthaler, 2004) for childhood rates. This decline is thought to be due to an increased awareness of dental health and hygiene, and higher rates of dental clinic action (Marthaler, 2004). It should be noted that there is an increased incidence of caries amongst the elderly, which can be seen as being related to better dental health and hygiene causing people to keep their teeth till later life (Selwitz et al., 2007).

Much has also been made of the effect on a developing country of the prevalence of dental caries. One study presented data spread over 14 years for Riyadh, Saudi Arabia (Al-Sadhan, 2006). In 1987, dental caries had a prevalence of 59.2% amongst schoolchildren. This had risen to 93.7% in 2000, with males showing a higher DMFT value than females. The Saudi Arabian(Al-Sadhan, 2006) study

also showed that in terms of the DMFT value, the decayed component (D) has the highest influence in both groups (male or female) studied. The D value was found to be lower in the rural areas than in urban areas; however the missing and filled (M,F) components were found to also be higher in the urban areas. While this could be associated with difference in lifestyles and eating habits or diets in the urban and rural areas, it also points towards a lesser number of treatment options in the rural communities.

It is clear to see from the research that dental caries is a worldwide problem that does not seem to be going away, despite a decline of incidence in some demographics. It is therefore important to look at what is being done to diagnose, monitor and ultimately treat dental caries.

Visual and tactile diagnosis of dental caries

The most common method of caries detection in the dental clinic is that of vision. The dentist first and foremost uses a "highly evolved, continually re-adjusting sensor" (Hall and Girkin, 2004), i.e. their sight (Selwitz et al., 2007), to observe any irregularities on the tooth surface which may denote disease. In the early stages of caries, the subsurface dissolution of the enamel causes changes in the optical properties of the enamel producing 'white spot lesions' on the surface. These are detected by drying the surface of the enamel, using air, and then observing, sometimes with the aid of a mirror for posterior of buccal tooth surfaces. The change in optical properties will be discussed in depth in a subsequent chapter, but briefly, the act of air drying serves to increase the relative refractive indices of the caries lesion and the surrounding sound enamel.

In order to aid this technique, a metal rod known as an explorer is used (Selwitz et al., 2007; McComb and Tam, 2001; Hamilton and Stookey, 2005; Pretty and Maupome, 2004). This is a sharp tool which gives the dentist a degree of tactile sensory information when observing a tooth. By prodding and

dragging across the surface of the tooth, the clinician is able to use Radike's method (Radike, 1972) of using the 'tackiness' and 'force of withdrawal' of suspect areas to make a diagnosis (Hamilton and Stookey, 2005). However, as can be gathered by the description, this is a very subjective method (Pretty, 2006) and has a sensitivity of only around 39-59% in occlusal surfaces (Selwitz et al., 2007) and other work has accused the method of having sensitivities of lower than 30% (McComb and Tam, 2001). However, the same work also points out that with expertise and specific training in the method, sensitivities over 60% are possible.

It has also been noted in the research that care should be taken when applying pressure using the sharp metal tool so as to not damage the surface of the tooth or implant foreign organisms (McComb and Tam, 2001). This view is also related in a paper by Kuhnisch et al, 2007 (KÃ$\frac{1}{4}$hnisch et al., 2007) in which it was stated that "using a sharp dental probe for occlusal caries detection causes enamel defects" and that it should be considered an inappropriate procedure.

However, it should be asked why a potentially dangerous tool is commonplace in the dental clinic. As the standard tool of dentistry, it is taught in the dental schools from the start of the course and the technique is continually refined through the clinician's career (Hamilton and Stookey, 2005). A dental explorer can be used without special sterilisation procedures or protective sleeves (Hamilton and Stookey, 2005). In order to counterpoint the argument regarding the transfer of disease by the tool, Hamilton points out that if this was the case one would expect the problem to become obvious due to the number of teeth probed every day.

In response to the claims by Ekstrand that the probe can cause microscopic damage to the enamel surface, Hamilton argues that this damage is detected at a magnification of x25 and is therefore of little consequence to the health of the tooth. Furthermore, he points out that the work that has been published on such damage is carried out on ex-vivo samples with no follow-up providing proof of

a lack of remineralisation by the natural environment (Hamilton and Stookey, 2005).

It is easy to see though that the dental explorer only allows investigation of the outer surface of the tooth in, at best, a minimally invasive way. In order to gain more information about sub-surface lesions, the dentist can use X-ray bite-wing radio-graphs.

An X-ray bite-wing radio-graph, as can be understood from its name is a method of imaging the tooth using X-rays via a plate of photographic film, or more recently a CCD array, inside a bite-wing (Wenzel, 2004). The photographic film is held between the upper and lower jaw by the teeth and the patient is exposed to X-rays. A two dimensional representation of the teeth in the jaws is produced. Carious lesions are indicated by shadowing in the images. The relative change in brightness between sound and carious enamel arises through the reduced density of carious enamel. The reduced density givers rise to less absorption at the lesion, allowing more x-rays to propagate through the tooth to the photographic film (or digital camera), which darkens under exposure.

While the dental explorer technique works on a tooth by tooth basis, a bite-wing radio-graph shows the full jaw with one measurement. The clinician can then spend time interpreting the image without the patient being involved. This has an advantage for patient comfort, whereby longer diagnosis times with the dental explorer means longer time probing the patients mouth.

The technique has a low sensitivity in relation to detecting surface lesions, around 50%, with a specificity of around 80% (Selwitz et al., 2007). However, for later stage lesions which have progressed to the dentine the sensitivity can be up to 70%, specificity around 70% (Wenzel, 2004). However, some reports have put the sensitivity in dentine at around 40%(Selwitz et al., 2007), but agree on a high specificity.

It has also been stated that caution should be used when looking to use ra-

diographs, and that they should not be used before clinical examination (Wenzel, 1995). Wenzel also makes mention of the fact that radiographs are not accurate with later stage lesions, stating that "lesions shown in the dentine by radiographs should be treated surgically". Another drawback to radiographs is in their lack of ability to distinguish between active and arrested lesions (Selwitz et al., 2007; Wenzel, 2004).

Electrical impedance measurements

The measurement of the electrical impedance of a tooth is emerging as a new technique for the detection of dental caries. It relies on the relative changes of electrical impedance between sound and carious enamel due to changes in porosity and structure. Increased porosity creates pockets of ionic fluid, which increases the electrical conductivity of the lesioned area (and conversely reduces the resistance) (Longbottom and Huysmans, 2004). However, far from being an imaging technique, the electrical impedance measures the bulk conductance of the tooth as a whole and presents a reading to the clinician (Longbottom and Huysmans, 2004).

The technique has been found to have a lower sensitivity to visual and tactile diagnosis, but with a higher specificity(Longbottom and Huysmans, 2004). This is probably due in part to the technique only measuring a bulk value for each tooth rather than being lesion-site specific. Due to the measurement coming from the status of fluid inside pores caused by lesions, hydration is an issue, especially after long periods of diagnosis (Longbottom and Huysmans, 2004).

2.3.2 Acid erosion

Whereas dental caries cause the loss of material from the tooth via bacterial interactions and is initially reversible, dental erosion is the irreversible loss of dental material without involving bacteria (Nunn, 1996). Dental erosion is an

increasing problem with the change in dietary habits around the world. A key example usually used of the problem is the perceived acceleration of erosion figures and the rise in the sales of fizzy drinks (Jensdottir et al., 2005; Zero and Lussi, 2005; West et al., 2001).

Pathology

In the discussion about the enamel of the tooth, it was stated that the enamel is susceptible to breakdown in acid environments. The enamel of the tooth is able to survive in environments down to around 4.6pH but when the surrounding environment becomes more acidic the enamel starts to dissolve. A good description of the surface dissolution comes from (Zero and Lussi, 2005):

> "Once in contact with the enamel, the acid with its hydrogen ion (or with its chelating capacity) will start to dissolve the crystal. The unionised form of the acid will then diffuse into the inter-prismatic areas of the enamel and dissolve the mineral in the subsurface region. This will lead to an outflow of tooth mineral ions (calcium and phosphate) and subsequently to a local pH rise in the tooth structure in close proximity to the enamel surface"

As stated, the erosion starts on the enamel surface, and if left untreated can progress until the dentine is exposed. The dentine, being of a similar composition to enamel also dissolves in acidic environments (Zero and Lussi, 2005). If the dentine is left untreated then penetration through to the pulp chamber can occur, leading to exposed nerves and pain.

Factors which contribute to dental erosion have been studied extensively and can be classified into two groups, namely extrinsic and intrinsic. The extrinsic factors which are mentioned frequently in the literature include acidic foods (Zero and Lussi, 2005; West et al., 2001), carbonated beverages (Jensdottir et al., 2005; Zero and Lussi, 2005; Nunn et al., 2003; Jarvinen et al., 1991; Tahmassebi et al.,

2006), sports drinks (Zero and Lussi, 2005; West et al., 2001), wines (Zero and Lussi, 2005), drugs (Lussi, 1996) and citrus fruits (Zero and Lussi, 2005; West et al., 2001; Nunn et al., 2003). Exposure to acidic work environments is also mentioned(Zero and Lussi, 2005). Regurgitation through medical complaints is commonly cited as an intrinsic factor (Zero and Lussi, 2005).

With so many factors influencing erosion in the worldwide population's mouths, it is now a good idea to investigate how prevalent dental erosion is today.

Epidemiology of dental erosion

It is clear from the literature that dental erosion is an increasing problem (Nunn et al., 2003; Nunn, 1996; Al-Dlaigan et al., 2001; von Fraunhofer and Rogers, 2004). Despite this, prevalence studies are still relatively rare in the literature (Nunn, 1996) and those that do exist tend to look at erosion in adolescents (11-16 years old), and in some cases convenience samples (Deery et al., 2000) where they are exclusively from dental patients (and therefore more likely to have disease) rather than the general public. The tendency to use samples from adolescents is for a number of reasons, but mainly that the teeth, while permanent, have only been erupted for a few years. It is thus easier to infer relationships from the dietary and lifestyle information gathered when monitoring the erosion (Nunn, 1996).

The results of a number of published prevalence studies carried out in the UK are presented in Figure 2.3, where the increasing prevalence through time is obvious. Nunn, 1996 concludes in her study that approximately half of children in the UK suffer from dental erosion, with a higher prevalence in the North than in London and the South East areas.

From this it is possible to infer a relation between socio-economic background and prevalence of dental erosion. London and the South-East of the UK is a much more wealthy area of the UK than the North. This relationship is shown in a

number of other studies as well (Al-Dlaigan et al., 2001).Most of the literature is agreed that one of the main culprits for the rise in the prevalence is the increase in fizzy drink consumption (Nunn et al., 2003; Al-Dlaigan et al., 2001; von Fraunhofer and Rogers, 2004). Fraunhofer (2004) states that soft drink production has increased five-fold over the 50 years between 1947 and 1997, and Tahmassebi (2006) paints a similar picture with a 56% rise in the previous 10 years and a projected rise of 2-3% over the years to come. Both studies found that there was no difference between diet and regular versions of the same brand of cola drinks as both contain an acidic component (Tahmassebi et al., 2006; von Fraunhofer and Rogers, 2004).

Detection and monitoring of dental erosion

When discussing the detection and monitoring of erosion, it is useful to consider two environments in which this task may be undertaken, namely the laboratory and the clinic.

The detection and monitoring of erosion in the dental clinic is a very subjective process, based on visual and tactile investigations to produce outcomes from indices of wear (Al-Malik et al., 2001; Amaechi and Higham, 2005). Accurate and reliable measurements are hard to come by due to the lack of a stable reference point in the tooth (Azzopardi et al., 2001) and as such there is no diagnostic device available for the early detection and quantification of dental erosion (Amaechi and Higham, 2005).

Indices which are used come in many different forms, from the Smith and Knight technique which uses putty impressions or photographs for continual monitoring (Azzopardi et al., 2001; Grenby, 1996) to others which have finely graded steps in their diagnosis (Lussi, 1996). The use of photographs, however, is heavily dependent on the environmental properties (light, position) and photographer ability (Amaechi and Higham, 2005) and finer steps tend to prolong diagnostic

time and reduce inter-examiner agreement (Lussi, 1996). It has also been commented that some indices for dental erosion are too generic in that they do not take in to account aetiology and thus monitor tooth wear as a whole (Al-Malik et al., 2001; Grenby, 1996).

Detection and quantification of erosion in the laboratory is a much more invasive task. Ex-vivo studies can utilise scanning electron microscopy, surface micro-hardness techniques (Hannig and Balz, 1999; Kato et al., 2007), optical methods and ultrasound. The latter two will be discussed in full in later chapters of this thesis.

Thus, the detection of dental erosion in the clinical environment is an extremely subjective process reliant on indices of varying scales, skills of the clinician and environments, resulting in difficult monitoring. While in the laboratory, erosion can be monitored in a quantitative manner, however, techniques are far from non-invasive and sample destruction is common.

2.4 Conclusions

In this chapter, dental caries has been discussed and shown to be a highly prevalent disease affecting a large proportion of the western world's population. While there have been investigations into various techniques for detecting and monitoring dental caries, there are as yet no quantitative methods available to the dentist in the clinic.

Dental erosion is an increasing problem in the western world, especially with the change in people's lifestyles and dietary habit. Due to the lack of suitable reference points on the surface of the tooth, there are no quantitative detection or monitoring tools available to the dental clinician.

2.4.1 Requirements for a diagnostic device

There are a number of requirements for a diagnostic device for the dental clinic. What now follows is a brief discussion of a few parameters: resolution, penetration depth, size or form-factor, clinician and patient comfort.

Relative to the human body, the tooth is a small object and as such the changes brought on by disease are also small. Therefore, for detection, as high spatial resolution as possible is required. With dental caries, lesions first visually manifest as small white spots on the surface of the enamel, and therefore any device for diagnosing early (reversible) caries should be able to localise to these areas. This points towards spatial resolutions of less than around 50μm. These lesions begin under the surface of the enamel and therefore a high axial resolution ($<50\mu$m) coupled with enough penetration depth to image the full enamel layer (up to a few millimetres) would be ideal.

Access to the front teeth is easy through the front of the mouth, however, side and rear teeth have limited access. Therefore an ideal device should be small enough to be manoeuvrable inside the oral cavity. This points to an active device probe being of millimetres up to a centimetre in dimensions. A lesser dimension being better with reference to observing the occlusal (inter-teeth) surfaces.

The smaller the device, the more comfortable it would be for the patient. Patient stress levels are anecdotally high, and any device should be designed to not increase these any more. This also points towards a perfect diagnostic device being minimally invasive and simple for the clinician to use in order to reduce 'in clinic' duration for the patient. With a view of simplicity, perhaps the perfect device would only use intrinsic biological components for measurements to reduce the pre-treatment for the patient. Such intrinsic components could be the structures and chemical properties of the enamel and dentine (optical, ultrasonic or electrical).

Now that the two main dental disease have been discussed, the rest of this

thesis will investigate two different modalities for the diagnosis of these. The first modality to be investigated will be that of photonics, with concentration on confocal microscopy for the detection of dental caries. Afterwards, attention shall be turned to ultrasound as a method of detecting and monitoring dental erosion.

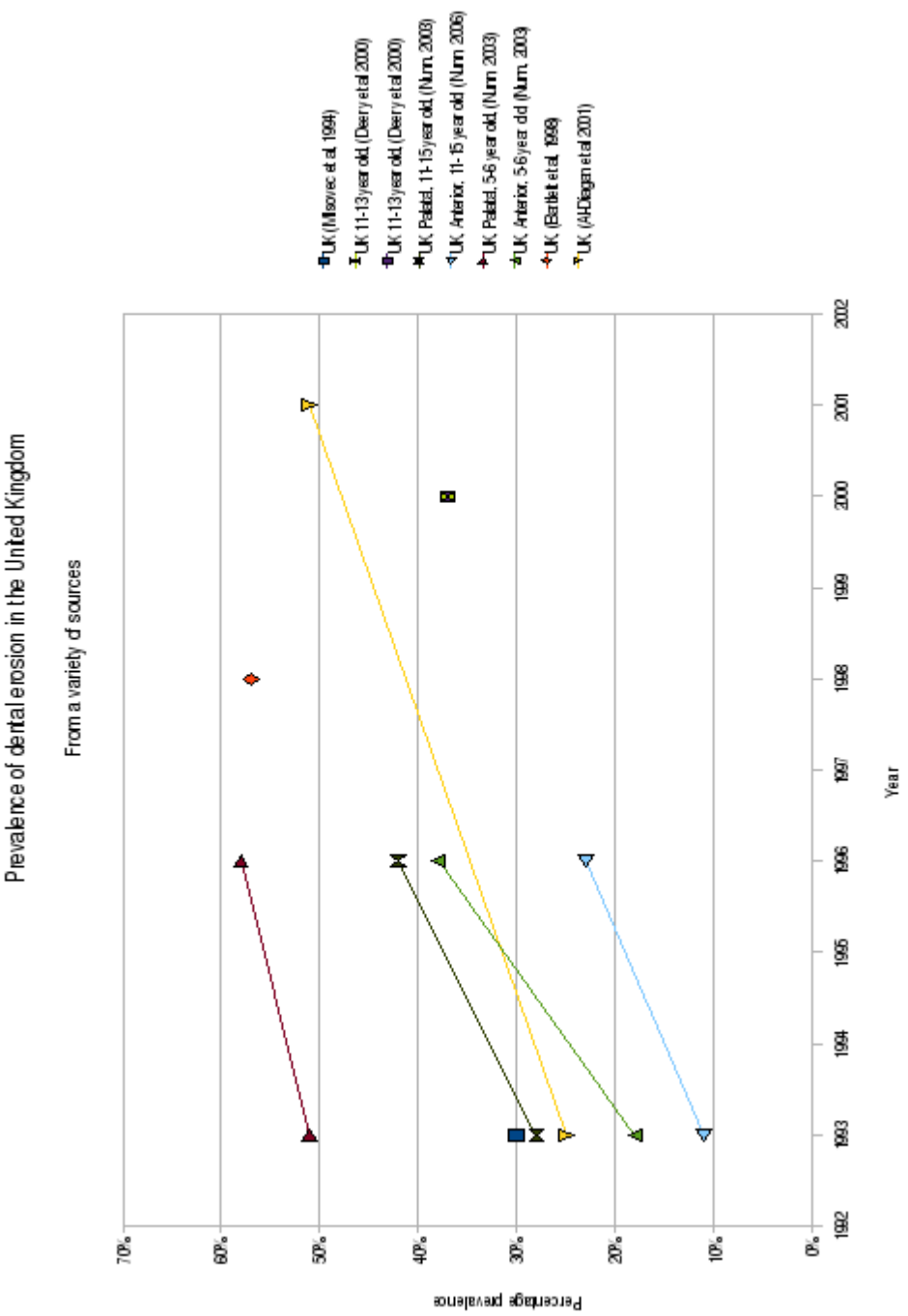

Figure 2.3: Prevalence of dental erosion in previous years

Bibliography

Y H Al-Dlaigan, L Shaw, and A Smith. Dental erosion in a group of british 14-year-old, school children. part i: Prevalence and influence of differing socioeconomic backgrounds. *British Dental Journal*, 190(3):145–9, February 2001. ISSN 0007-0610. doi: 11236918. URL `http://www.ncbi.nlm.nih.gov/pubmed/11236918`. PMID: 11236918.

M I Al-Malik, R D Holt, R Bedi, and P M Speight. Investigation of an index to measure tooth wear in primary teeth. *Journal of Dentistry*, 29(2):103–7, February 2001. ISSN 0300-5712. doi: 11239584. URL `http://www.ncbi.nlm.nih.gov/pubmed/11239584`. PMID: 11239584.

S. A. Al-Sadhan. Dental caries prevalence among 12-14 year-old schoolchildren in riyadh: A 14 year follow-up study of the oral health survey of saudi arabia phase i. *Saudi Dental Journal*, 18(1), 2006.

B T Amaechi and S M Higham. Dental erosion: possible approaches to prevention and control. *Journal of Dentistry*, 33(3):243–52, March 2005. ISSN 0300-5712. doi: S0300-5712(04)00164-2. URL `http://www.ncbi.nlm.nih.gov/pubmed/15725524`. PMID: 15725524.

A Azzopardi, D W Bartlett, T F Watson, and M Sherriff. The measurement and prevention of erosion and abrasion. *Journal of Dentistry*, 29(6):395–400, August 2001. ISSN 0300-5712. doi: 11520587. URL `http://www.ncbi.nlm.nih.gov/pubmed/11520587`. PMID: 11520587.

C Deery, M L Wagner, C Longbottom, R Simon, and Z J Nugent. The prevalence of dental erosion in a united states and a united kingdom sample of adolescents. *Pediatric Dentistry*, 22(6):505–10, 2000. ISSN 0164-1263. doi: 11132512. URL `http://www.ncbi.nlm.nih.gov/pubmed/11132512`. PMID: 11132512.

B. L. Edelstein. The dental caries pandemic and disparities problem. *BMC Oral Health*, 6(Suppl 1):S2, 2006.

T H Grenby. Methods of assessing erosion and erosive potential. *European Journal of Oral Sciences*, 104(2 (Pt 2)):207–14, April 1996. ISSN 0909-8836. doi: 8804888. URL `http://www.ncbi.nlm.nih.gov/pubmed/8804888`. PMID: 8804888.

S. Habelitz, S. J. Marshall, G. W. MarshallJr, and M. Balooch. Mechanical properties of human dental enamel on the nanometre scale. *Archives of Oral Biology*, 46(2):173–183, February 2001. doi: 10.1016/S0003-9969(00)00089-3. URL `http://www.sciencedirect.com/science?_ob=ArticleURL&_udi=B6T4J-4233N49-9&_user=10&_rdoc=1&_fmt=&_orig=search&_sort=d&view=c&_version=1&_urlVersion=0&_userid=10&md5=07418db393b9f42b491344accfeb1278`.

A. Hall and J. M. Girkin. A review of potential new diagnostic modalities for caries lesions. volume 83, pages 89–94. IADR, 2004.

J. C. Hamilton and G. Stookey. Should a dental explorer be used to probe suspected carious lesions? *The Journal of the American Dental Association*, 136(11):1526–1532, 2005.

M. Hannig and M. Balz. Influence of in vivo formed salivary pellicle on enamel erosion. *Caries Research*, 33(5):372–379, 1999. ISSN 0008-6568. URL `http://www.karger.com/DOI/10.1159/000016536`.

V. K. Jarvinen, I. I. Rytomaa, and O. P. Heinonen. Risk factors in dental erosion. *J Dent Res*, 70(6):942–947, June 1991. URL http://jdr.iadrjournals.org/cgi/content/abstract/70/6/942.

Thorbjörg Jensdottir, Allan Bardow, and Peter Holbrook. Properties and modification of soft drinks in relation to their erosive potential in vitro. *Journal of Dentistry*, 33(7):569–575, August 2005. doi: 10.1016/j.jdent.2004.12.002. URL http://www.sciencedirect.com/science?_ob=ArticleURL&_udi=B6T86-4FGXS74-2&_user=10&_rdoc=1&_fmt=&_orig=search&_sort=d&view=c&_acct=C000050221&_version=1&_urlVersion=0&_userid=10&md5=560f915c78960b13893bc87f09c9a972.

M T Kato, S H Sales-Peres, and M A R Buzalaf. Effect of iron on acid demineralisation of bovine enamel blocks by a soft drink. *Archives of Oral Biology*, 52(11):1109–1111, November 2007. doi: 10.1016/j.archoralbio.2007.04.012. URL http://www.sciencedirect.com/science?_ob=ArticleURL&_udi=B6T4J-4NX8RHH-4&_user=10&_rdoc=1&_fmt=&_orig=search&_sort=d&_docanchor=&view=c&_searchStrId=983894971&_rerunOrigin=scholar.google&_acct=C000050221&_version=1&_urlVersion=0&_userid=10&md5=b2f209b1708daa301df5281a11ec594f.

J. KÃ¼hnisch, W. Dietz, L. StÃ¶sser, R. Hickel, and R. Heinrich-Weltzien. Effects of dental probing on occlusal surfaces – a scanning electron microscopy evaluation. *Caries Research*, 41(1):43–48, 2007. ISSN 0008-6568. URL http://www.karger.com/DOI/10.1159/000096104.

C. Longbottom and M.-C.D.N.J.M. Huysmans. Electrical measurements for use in caries clinical trials. *Journal of Dental Research*, 83(suppl 1):C76–C79, 2004. doi: 10.1177/154405910408301S15. URL http://jdr.sagepub.com/content/83/suppl_1/C76.abstract.

A Lussi. Dental erosion clinical diagnosis and case history taking. *European Journal of Oral Sciences*, 104(2):191–198, 1996. doi: 10.1111/j.1600-0722.1996.tb00067.x. URL http://dx.doi.org/10.1111/j.1600-0722.1996.tb00067.x.

T. M. Marthaler. Changes in dental caries 1953-2003. *Caries Research*, 38(3): 173, 2004.

D McComb and L. E. Tam. Diagnosis of occlusal caries: Part i. conventional methods. *J Can Dent Assoc*, 67(8):454–7, 2001.

A H Meckel, W J Griebstein, and R J Neal. Structure of mature human dental enamel as observed by electron microscopy. *Archives of Oral Biology*, 10(5): 775–83, 1965. ISSN 0003-9969. doi: 5226910. URL http://www.ncbi.nlm.nih.gov/pubmed/5226910. PMID: 5226910.

J H Nunn. Prevalence of dental erosion and the implications for oral health. *European Journal of Oral Sciences*, 104(2):156–161, 1996. doi: 10.1111/j.1600-0722.1996.tb00064.x. URL http://dx.doi.org/10.1111/j.1600-0722.1996.tb00064.x.

J H Nunn, P H Gordon, A J Morris, C M Pine, and A Walker. Dental erosion – changing prevalence? a review of british national childrens' surveys. *International Journal of Paediatric Dentistry / the British Paedodontic Society [and] the International Association of Dentistry for Children*, 13(2):98–105, March 2003. ISSN 0960-7439. doi: 12605627. URL http://www.ncbi.nlm.nih.gov/pubmed/12605627. PMID: 12605627.

Poul Erik Petersen, Denis Bourgeois, Hiroshi Ogawa, Saskia Estupinan-Day, and Charlotte Ndiaye. The global burden of oral diseases and risks to oral health. *Bulletin of the World Health Organization*, 83:

661–669, 2005. URL http://www.scielosp.org/scielo.php?script=sci_arttext&pid=S0042-96862005000900011&nrm=iso.

I. A. Pretty. Caries detection and diagnosis: Novel technologies. *Journal of Dentistry*, 34(10):727–739, 2006.

I. A. Pretty and G. Maupome. A closer look at diagnosis in clinical dental practice: Part 5. emerging technologies for caries detection and diagnosis. *J Can Dent Assoc*, 70(8):540, 2004.

AW Radike. Criteria for diagnosis of dental caries. In *Proceedings of the conference on the clinical testing of cariostatic agents*, pages 87–88, Chicago, 1972. ADA Council on Dental Research.

R. H Selwitz, A. I Ismail, and N. B Pitts. Dental caries. *The Lancet*, 369(9555):51–59, 2007. doi: 10.1016/S0140-6736(07)60031-2. URL http://www.sciencedirect.com/science/article/B6T1B-4MRGVD0-13/2/73cdc9abd2a8177a4bdf4445b6d2dee9.

J.F. Tahmassebi, M.S. Duggal, G. Malik-Kotru, and M.E.J. Curzon. Soft drinks and dental health: A review of the current literature. *Journal of Dentistry*, 34(1):2–11, January 2006. doi: 10.1016/j.jdent.2004.11.006. URL http://www.sciencedirect.com/science?_ob=ArticleURL&_udi=B6T86-4H39752-1&_user=10&_rdoc=1&_fmt=&_orig=search&_sort=d&view=c&_acct=C000050221&_version=1&_urlVersion=0&_userid=10&md5=ea13bdacbe6675a78f68b00c735fcf4f.

J A von Fraunhofer and M M Rogers. Dissolution of dental enamel in soft drinks. *General Dentistry*, 52(4):308–12, 2004. ISSN 0363-6771. doi: 15366295. URL http://www.ncbi.nlm.nih.gov/pubmed/15366295. PMID: 15366295.

A Wenzel. Current trends in radiographic caries imaging. *Oral Surgery, Oral Medicine, Oral Pathology, Oral Radiology, and Endodontology*,

80(5):527–539, November 1995. doi: 10.1016/S1079-2104(05)80152-0. URL http://www.sciencedirect.com/science?_ob=ArticleURL&_udi=B6WP1-4JF8YB7-B&_user=10&_rdoc=1&_fmt=&_orig=search&_sort=d&view=c&_acct=C000050221&_version=1&_urlVersion=0&_userid=10&md5=d42de838ef8c12c0f8b0be08582e04fa.

A. Wenzel. Bitewing and digital bitewing radiography for detection of caries lesions. *J Dent Res*, 83(suppl_1):C72–75, July 2004. URL http://jdr.iadrjournals.org/cgi/content/abstract/83/suppl_1/C72.

N X West, J A Hughes, and M Addy. The effect of pH on the erosion of dentine and enamel by dietary acids in vitro. *Journal of Oral Rehabilitation*, 28(9): 860–4, September 2001. ISSN 0305-182X. doi: 11580825. URL http://www.ncbi.nlm.nih.gov/pubmed/11580825. PMID: 11580825.

D T Zero and A Lussi. Erosion–chemical and biological factors of importance to the dental practitioner. *International Dental Journal*, 55(4 Suppl 1):285–90, 2005. ISSN 0020-6539. doi: 16167607. URL http://www.ncbi.nlm.nih.gov/pubmed/16167607. PMID: 16167607.

Chapter 3

Optical techniques for dentistry

3.1 Introduction

Now that an introduction to teeth and the diseases associated with them has been given in the previous chapter, attention shall now turn to investigating methods of detecting these diseases. The next four chapters are devoted to an optical method based on confocal microscopy of detecting dental caries.

However, before describing how beams of light can be used to diagnose dental disease it is advisable to discuss how light interacts with dental tissues. After the basics have been laid down, the current 'new' optical technologies to aid detection of dental disease will be discussed. Afterwards, the technique of confocal microscopy will then be examined in depth and its implications for the detection of dental disease. Finally fibre optic confocal microscopy will be introduced in order to move towards a hand held quantitative device for the detection of dental caries.

The electromagnetic spectrum is vast, going from radioactive gamma rays all the way to long wave radio, however, the section of this spectrum that is of interest to this thesis is the optical region of the spectrum which lies between 300nm (ultraviolet) and 1.5μm (near infrared). The nature of light is a large topic, and outside the scope of this thesis, therefore this chapter will begin with only a brief introduction to the field of optics.

3.2 The nature of light

The study of light, commonly known as optics, has a long and varied history, centring on a disagreement between two models that were finally joined at the start of the 20th Century with the emergence of quantum mechanics. In the 17th Century both Isaac Newton and Robert Hooke studied the behaviour of light in separation. Newton explained his ideas using a particle based model whereby light was composed of quantities of light known as 'corpuscles'. Using this he

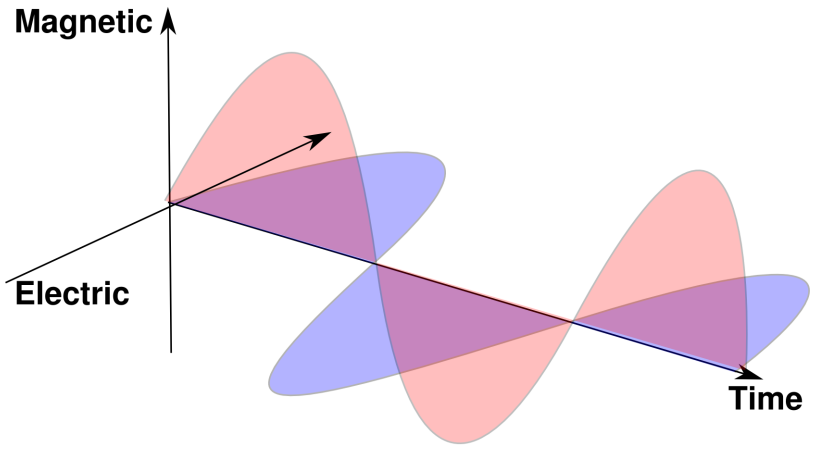

Figure 3.1: Electromagnetic field propagating through time with perpendicular electric and magnetic fields

was able to explain observations such as the spectrum of sunlight and refraction. However, his model could not explain diffraction as seen in Young's two split experiment where the patterns are seen when a beam of light is reflected around an object, giving rise to regions of light in areas where the particle model dictates there should be a shadow.

Hooke's work concentrated on a wave model of light, and as such could explain diffraction using the idea of wave-fronts (as stated in Huygens Law). This wave model could also explain refraction, reflection and the spectrum (through superposition of waves). Another key result which the wave model could explain was the slowing down of light as it passed into a denser medium (the corpuscle model predicted the opposite). The all encompassing nature of the wave model meant that it was accepted by the scientific community and Newton's corpuscle model was abandoned.

However, the wave model had the implication that light waves would need a medium to propagate through and so the aether was proposed. Experiments in the late 19th century by Michelson and Morely proved (through a failed hypothesis) that the aether did not exist. This was a blow to the wave model but was not enough to detract from the universal acceptance of the model.

Around the same time, James Clerk Maxwell was able to explain the propagation of light and its velocity of c through a unification of the electrostatic and magnetic forces. In this model, light is an electromagnetic wave, composed of an oscillating perpendicular electric and magnetic field (as shown in Figure 3.1). Through his four Maxwell equations he postulated that the speed of light would be dependent on the permittivity and permeability of free space. Through experiment this was verified and found that the value of c to be 299,792,458ms^{-1}. There is no difference between the region known as the visible spectrum to the rest of the electromagnetic spectrum other than the human eye is tuned to detect the waves of that wavelength band.

In 1905, Albert Einstein studied the photoelectric effect and noted that light shone on a piece of metal could produce a current for which he would win a Nobel prize in 1926. This current was proportional to the wavelength of the light and not to the intensity of the light. This could not be explained by the wave model and so the particle model re-emerged when Einstein postulated that light was composed of 'quanta' of light which he called Photons, each with an energy of E=hf, where h is known as Plank's constant (h=6.62606896E-34), and f is the frequency of the wave. Through this theory a wave-particle duality of light was proposed, and further established and accepted through verification of Compton Scattering.

And so, light is both a wave and a particle at the same time, travelling at the constant speed of around 3x108 ms^{-1}. What now follows is a discussion of how these peculiar beams interact with matter, specifically the materials which comprise the tooth.

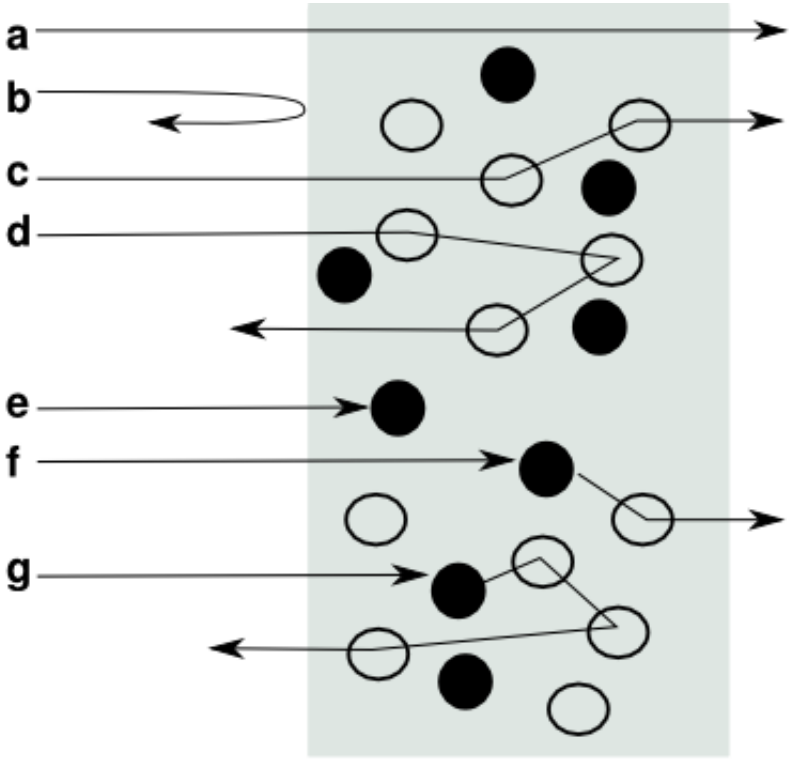

Figure 3.2: Optical interactions with matter. a) Transmission, b) Reflection, c) Scattering with transmission, d) Scattering with backscattering, e) Absorption, f) Fluorescence with transmission and g) Fluoresence with backscattering

3.3 Optical properties of dental tissues

The fact that a tooth is visible to the human eye is proof that light interacts with the materials. By considering the enamel and dentine as inhomogeneous materials (considering the make up of biomaterials such as collagen and hydroxyapatite as discussed in Chapter 2), it is possible to break the categories of optical interactions down to three main groups either reflection, scattering or absorption. With the latter possibly leading to fluorescence. Each of these interactions shall now be discussed with reference to the numerical properties of dental enamel and dentine.

Throughout the discussion, Figure 3.2 shall be referenced as a visual aid. In this diagram, the black circles represent particles which absorb an incoming wave, and the transparent circles represent scattering particles.

3.3.1 Reflection

Reflection (Figure 3.2b) is a macroscopic event that occurs when a light wave is incident on a surface of an object, or more generally when a wave is incident on a particle of much greater dimension than the incident wavelength. The result is a change in direction of the wave without any alteration in the energy of wave.

The amount of the wave which is reflected (and, conversely, transmitted) by an object can be calculated by the refractive indices of the materials. The refractive indices of enamel and dentine are 1.62 and 1.45 respectively. By using the Fresnel equation for the reflection coefficient

$$R = \frac{n_1 cos\theta_1 - n_2 cos\theta_2}{n_1 cos\theta_1 + n_2 cos\theta_2}^2$$

it is possible to calculate the amount of light that would be reflected at certain boundaries. This makes it possible to find out how much light is actually able to get inside the tooth for observation purposes. For simplicity the assumption of normal ($\theta_1 = 0$) incidence will be assumed. This allows the Fresnel equation to be reduced to $R = \frac{n_1 - n_2}{n_1 + n_2}$. For the air-enamel boundary the percentage of reflected light is calculated to be 6%, which means that 94% of the incident light is transmitted in to the tooth. If we ignore other effects such as scattering and absorption it can be calculated that when this light reaches the enamel dentine boundary (or junction), 0.06% of the light is reflected.

However, the effect of scattering cannot be totally ignored when discussing optical interactions with dental materials. It is actually the effect of scattering that gives rise to the tooth's colouration.

3.3.2 Scattering

In reflection the incident wave is reflected in one direction (through Snell's law), however, there is an interaction whereby the incident wave is scattered in all directions. Rayleigh scattering occurs when a wave of light's direction is changed

through interacting with a small particle (of dimensions smaller than the incident wavelength) or object inside an inhomogeneous material. Due to the relative size of the particle to the wavelength, this process is very wavelength dependent. However, if the dimensions are larger than the incident wavelength, then Mie Scattering takes over and this wavelength dependence drops. One can see these effects when considering the sky being blue (where only the blueish light, with a shorter wavelength, is scattered), and clouds appearing white where Mie scattering causes scattering across all wavelengths.

In classical theory scattering occurs when the oscillating electric field of the incident wave causes the electrons in the scattering particle to oscillate. Due to this oscillation, radiation is emitted at the same frequency and phase as the incident wave. Thus the scattering particles are seen to absorb the incident wave's energy and scatter it in all directions, with no change in frequency (Tipler and Llewellyn, 1999).

In single scattering, the direction of the wave is changed once. However, multiple scattering is more common which can lead to transmission (Figure 3.2c) where the wave continues to propagate in much the same direction as before the scattering events, or backscattering (Figure 3.2d) where the net effect of the individual scattering events lead to the wave propagating in the opposite direction to that at initial scattering.

Studies have shown that enamel and dentine are weakly scattering materials, with scattering coefficients (the fraction of incident light scattered per unit distance) shown to peak around 270nm and a sharp drop off above this. In the visible region the reduced coefficients have been measured to be $2.4cm^{-1}$ for enamel and $19.6cm^{-1}$ for dentine (Fried et al., 1995). It is thought that the scattering component in the dental materials is the organic collagen matrix. This explains why dentine, which has a lower percentage of mineral than enamel, has the higher scattering coefficient.

Tissue	$\{mu'_s\ (cm^1)$
Enamel	2.4
Dentine	19.6
Aorta	40
Whole Blood	6.11
Skin	35.5

Table 3.1: Reduced scattering co-efficents of biological tissues

A comparison of dental reduced scattering tissues against other biological tissues (taken from (Cheong et al., 1990)) are presented in Table 3.1. One can see that enamel has a lesser reduced coefficient to tissues such as Aorta and Skin, however, Dentine while still lower is more comparable. This is due to dentine having a higher organic component.

Enamel and dentine has an ordered structure made up of tubules and has been shown to exhibit light guiding properties (Kienle and Hibst, 2006). This light guiding nature of the materials leads to important and useful properties for disease detection and is shown in Figure 3.3.

In healthy dentine, light is guided through the tubule structure as shown in Figure 3.3a. However, when disease occurs in the tooth, the tubule structure is interrupted and damaged (as shown in Figure 3.3b) which leads to an increase in scattering (due to an increased randomness in the biological contents of that volume of material). This change in optical property can be observed as a relative change in a collected signal to that of the surrounding sound enamel.

3.3.3 Absorption and fluorescence

Absorption occurs when an object stops a wave of light and converts the energy into a different form (Figure 3.2e). The energy is commonly released in the form of heat but energy in the form of sound and light can also be produced. In the latter, this is known as Fluorescence (Figure 3.2f and g). The energy of the photon is absorbed by an object and then a lower energy photon is released.

Enamel and dentine are both weakly absorbing materials for much of the light

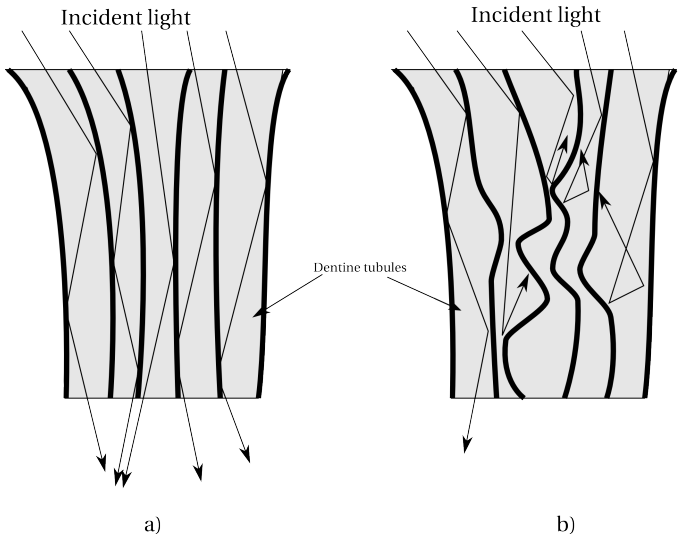

Figure 3.3: Incident light being scattered through a section of healthy dentine (a) and diseased dentine (b)

spectrum. There is a noted absorption peak at 270nm (in the ultraviolet region) for enamel (Spitzer and Bosch, 1975) which is useful for ablation techniques using excimer lasers. However, the low absorption in the Visible and NIR regions of the spectrum mean that these wavelengths can be used for diagnostic purposes with a minimal risk of heating (and therefore damage). Spitzer (1975) concluded that it was the biological component (the amino acids) of the enamel and dentine that were responsible for the absorption, which accounts for dentine having a higher absorption coefficient than enamel (ua=0.26mm^{-1} and ua=0.04mm^{-1} respectively) (Spitzer and Bosch, 1975).

Enamel is known to fluoresce when illuminated by 375nm light, emitting at 460 and 560nm, which is seen to be due to both the inorganic and organic components (Stookey, 2004). Dentine is known to fluoresce in the red when excited by a green light. This has been used in a technique for dental diagnosis which will be discussed in the next section where modern technologies in the dental clinic using optics are introduced.

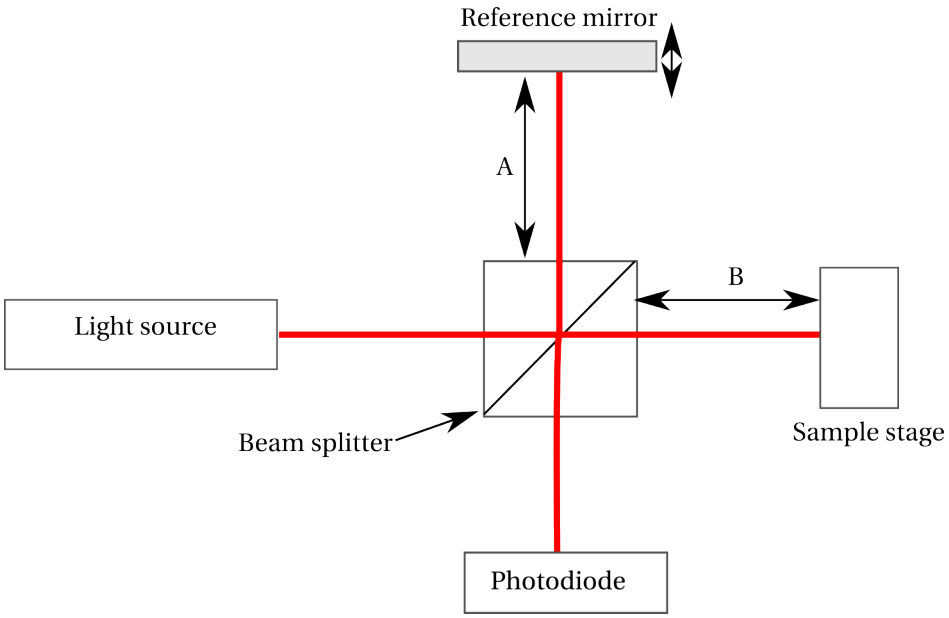

Figure 3.4: Schematic of an OCT system

3.4 Current optical techniques

There have been a number of new technologies investigated for use as dental diagnostic technologies. What follows is a brief description of some of the optical techniques and then a discussion on the advantages and disadvantages of these techniques before introducing the reasoning behind the technique of microscopy upon which the optics work in this thesis is based.

3.4.1 Optical coherence tomography

Optical coherence tomography (OCT) is a technique which utilises coherence effects of light waves to produce high resolution images (Huang et al., 1991). An OCT system is based upon the Michelson interferometer, as shown in Figure 3.4. A wide bandwidth light source is passed through a beam splitter so that half of the light goes to the sample to be imaged and the other goes to a reference mirror.

Upon reflection, these two light beams are combined and the resulting interference pattern is recorded on a photodiode. When the path difference (A-B in

Figure 3.4) is equal to nλ, where n is an integer and λ is the wavelength of the source, a maxima is recorded.

Therefore, as the reference mirror is scanned backwards and forwards, a series of maxima are recorded which match up to locations of reflecting objects inside the sample.

A wide bandwidth light source is required so that the coherence length of the illumination light is very short. If the coherence length was very long, the reference mirror would have to move a very long distance in order to produce a series of distinct maxima and minima. This would mean that the resolution of the system would not be suitable for resolving objects and layers within thin objects.

OCT has been demonstrated as a tool for dental imaging with depths of up to 1cm attained (Colston et al., 1998). A further modification to OCT which records information about the polarisation of the returned light, in order to take the birefringence properties of sound and caries enamel into account, has also been shown to be a useful aid for distinguishing between sound and caries enamel.

OCT has the advantage of producing high spatial and axial resolutions with large depth of field. This is in comparison to confocal microscope techniques (to be introduced in a later section) where high resolution is at the cost of depth of field, and to ultrasound which has a high depth penetration but poorer axial resolutions. The main disadvantage to OCT is cost, with suitable light sources that provide wide bandwidth costing tens of thousands of pounds.

3.4.2 Fluorescence based technologies

There are two types of applications of fluorescence when considering dental applications, Quantitative Light Fluorescence which operates in the ultraviolet and the commercial DiagnoDent device which operates using red wavelengths. A short description of both techniques follows.

QLF is a technique in which the tooth is illuminated with visible blue light and the resulting fluorescence is collected to form an image of the tooth on a computer screen (Bjelkhagen et al., 1982; Amaechi and Higham, 2002; Angmar-Maansson and Ten Bosch, 1987). A Green filter is used to collect intrinsic autofluorescent photons (arising from the aminoacids tryptophan and tyrosine in the collagen (KONIG et al., 1998)), and a red filter is used to collect fluorescence that is bacterially mediated(de Josselin de Jong et al., 2009).

Material loss, such as with a caries lesion, is associated with a drop in the return fluorescence signal due to the lesion scattering the fluorescent signal (which is thought to originate from the EDJ) away from the detector (as in Figure 3.3). A caries lesion can thus be detected by imaging the whole tooth surface and looking for areas of low return signal.

Using QLF with a green filter also has the advantage over other techniques that use the fluorescence seen in the red wavelengths (from bacteria by-products with the fluophore porphoryn (de Josselin de Jong et al., 2009)) in that it may hold information into the activity of the lesion (whether or not it is active or arrested). However, the output from a QLF set-up still relies on the user to interpret in much the same way as they would for an X-ray system which leads to issues of subjectivity.

DiagnoDent (KaVo, Germany) is more like a FOCOM system in that it produces a numerical result from the resulting fluorescence after excitation from a red laser light (655nm) source (Lussi et al., 2004). Caries lesions are detected by an increased measurement of the returned fluorescent signal (in contrast to QLF where a reduced signal signifies a lesion). This increased fluorescence during caries is thought to be from the bacterial by-products (through the fluophore porphoryn (de Josselin de Jong et al., 2009)); with the increased bacterial activity that comes with dental caries, producing more of a fluorescent signal (Ross, 1999). However, the actual source of the signal is still up for debate (Pretty and

Maupome, 2004).

However, the main disadvantage to this technique is the sample preparation needed. The accuracy is known to decrease due to the presence of stains, calculus (tartar), and even plaque and thus require a clean and dry surface (Pretty, 2006). This does not pose too much of a problem in a laboratory environment where such sample preparation can be considered routine. However, it should be noted that the DiagnoDent has not been proven useful to detect artificially created caries lesions through acid buffers, as these lack the bacteria that is thought to give rise to the fluorescent signal(Pretty and Maupome, 2004).

3.4.3 Fibre optic trans-illumination (FoTI)

FoTI uses the principle of scattering in order to improve the contrast between sound enamel and caries lesions in white light images (Davies et al., 2001). The tooth is illuminated by a thin beam of white light and areas of caries produce shadows through increased scattering, due to the break down of the tubule micro-structure of the enamel. The technique has been shown to improve detection rates when used alongside radiographs, however it has still to be taken up as a popular diagnostic technique (Pretty, 2006), and is subjective.

3.4.4 Absorption spectrophotometry

It is well established that absorption of light is dependent on wavelength, and that different materials have different absorption spectra. This is used by a number of techniques to measure concentration of substances in materials. Blood oxygen levels are routinely measured in hospitals by illuminating the thumb with light in order to measure the relative absorptions of de-oxygenated and oxygenated blood. This works because de-oxygenated blood is more absorbent below 830nm and oxygenated blood is more absorbent above 830nm. By measuring the drop in intensity of light as it passes through the blood, one can use the Beer law to

calculate oxygen levels of the blood.

This method has also been applied in the mouth in order to diagnose pulp vitality with recent modifications to allow for a clinical device. This works on the premise that a non-vital tooth will have lower flow of blood than one which is vital, and therefore by measuring the amount of oxygenated blood in the pulp chamber, one can see if the tooth is still being fed with new blood (Kahan et al., 1996).

The absorption properties of enamel in the near infrared region have also been shown to be useful for producing quantitative measurements of mineral loss by using a set-up similar to the QLF system described previously. Images are recorded using a CCD while the tooth is illuminated by a 1310nm superluminescent diode (SLED) (Jones et al., 2003).

Images from both trans-illumination and occlusal illumination can be recorded allowing better localisation of the mineral loss. The study was investigating the detection of dental defects, such as fluorsis, however, the ability to monitor mineral loss (or by connection gain) with such a simple system is far reaching.

3.5 The need for a new technology

While all the methods mentioned previously use optics to detect dental caries, none of the technologies (apart from perhaps QLF) produces a truly objective and quantitative measurement of a caries lesions (Pretty, 2006). FOTI produces photographic images of teeth with shadows due to lesions, however, the orientation of the tooth is crucial and most practitioners who have tried the FOTI technique use it as a second opinion with radiographs. There is thus a need for a new device to remove the dependence on the use of ionising radiation as a detection technique.

The DiagnoDent device is available commercially, however, unlike the QLF

technique there is little scientific work published on the effectiveness of the device (McComb and Tam, 2001). The main problem lies in the fact that there is little work into the correlation between the fluorescence response at 655nm and enamel loss. The QLF technique has many papers published on the fluorescence responses at 520-540nm but it is not possible to compare or infer the results to the DiagnoDent. This is probably due to the fact that it is thought that DiagnoDent relies on the bacterial by-products of dental caries for the fluorescence, and laboratory created caries lack these and instead rely on repeated acid buffering to produce lesions. Neither QLF or DiagnoDent have been shown to be useful for the detection of dentinal decay.

QLF produces numerical data as well as images of the teeth and lesions, however, the data out is a surface plot of relative detected fluorescence. The onus is still on the dentist to decide whether or not a lesion is to be operated on. While QLF produces a correlation between fluorescence and enamel material in order to produce a figure for the depth of lesion, this information could be confused between a larger lesion deeper into the enamel surface and a smaller one that is closer to the surface. This would lead to a dentist needing to remove enamel material until they are satisfied that they have removed all of the diseased tissue. Since the fluorescence is related to the relative amount of enamel material around a site, this makes QLF redundant for monitoring the removal of a lesion when enamel is being lost as well.

In order to address the need for a quantitative measurement tool of caries lesions that is able to measure the depth of a lesion as well as its thickness for monitoring purposes, the rest of this and subsequent chapters will investigate the use of confocal microscopy for dental disease detection. Confocal microscopy allows optical sections to be produced by rejecting out of focus light (Minsky, 1957). The technique has been shown to be compatible with dental tissues, and an adaptation using fibre optics has been demonstrated (Rousseau et al., 2007).

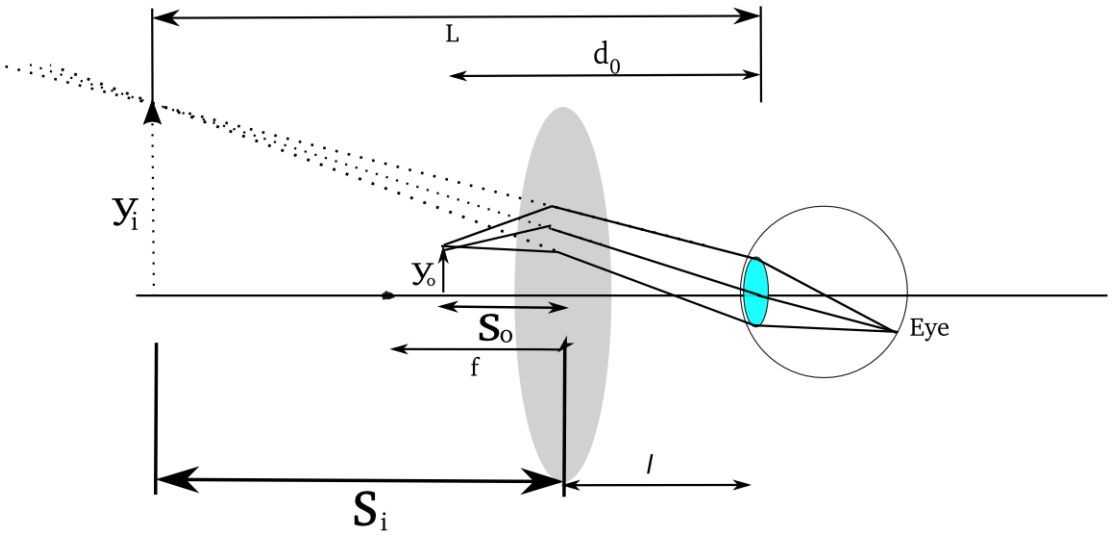

Figure 3.5: Image enlargement with a magnifying glass

In order to understand fully how this technique works, it is useful to introduce confocal microscopy by considering the concepts of basic microscopy.

3.6 Microscopy

Microscopy is the observation of microscopic objects, and as such instruments have been developed and used that produce an image of an object such that it appears larger than the original object actually is. The simplest of these tools is the magnifying glass (Figure 3.5). While this is simply a lens that produces positive magnification, it is useful to analyse the rays to understand how a microscope works

Magnification is defined as the ratio of the angle that the image makes with the optic axis (α_0), to that of the object with the optic axis (α_1) as shown in Figure 3.5:

$$M = \frac{\alpha_0}{\alpha_1} \tag{3.1}$$

For this, the paraxial region is the only one of concern, and therefore therefore

$$M = \frac{tan\alpha_0}{tan\alpha_1} \tag{3.2}$$

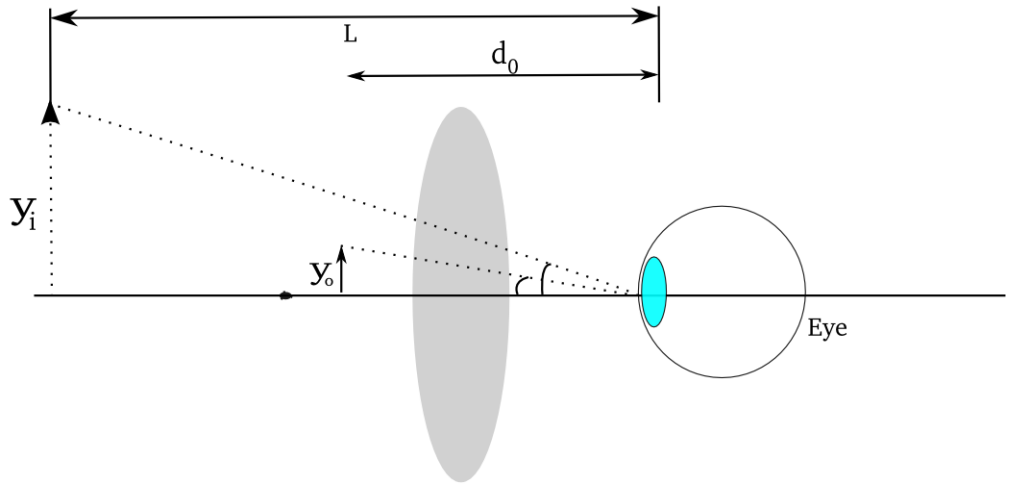

Figure 3.6: Reduced diagram of magnifying glass showing angles of interest.

Or, as can be seen from Figure 3.6,

$$M = \frac{y_i d_0}{L y_0} \tag{3.3}$$

The Gaussian lens formula is presented as

$$\frac{1}{s_0} = \frac{1}{s_i} + \frac{1}{f} \tag{3.4}$$

and the magnification can also be written as

$$M = -\frac{s_i}{s_0} \tag{3.5}$$

giving

$$M = (1 - \frac{s_i}{f})\frac{d_0}{d} \tag{3.6}$$

If D is taken to be the power of the lens, defined as $\frac{1}{f}$, then the magnification can be written as

$$M = (1 + D(L-1))\frac{d_0}{L} \tag{3.7}$$

This shows a dependence of the magnification on the distance of the eye to

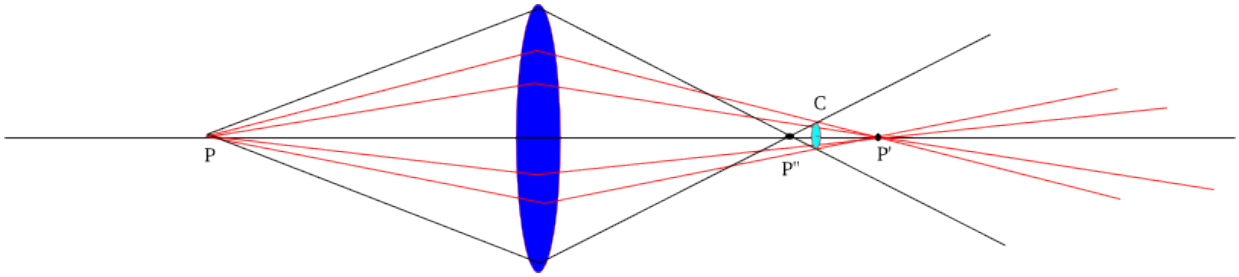

Figure 3.7: Spherical aberations, with centre of confusion labeled C

the object, d_0. This can be awkward to deal with in a practical environment. Therefore it is useful to remove this aspect from the magnifying glass to allow a more uniform magnification, along with comfort for the observer.

Also, it can be inferred that the magnification could be increased by decreasing the focal length of the lens ($M\alpha\frac{1}{f}$). However, it is assumed that the rays are paraxial and as such the angles made with the optic axis are very small (as seen in the above derivation). A decreased focal length can be achieved by increasing the curvature of the lens. This, however, also leads to larger angles with the optic axis for rays further away from the optic axis. The result of this is that the focal point is not a single point any more and is spread over a distance around the main focal point, this is known as a spherical aberration.

As is shown in Figure 3.7, the rays which are further from the optic axis in the lens have a greater angle of refraction, and as such meet the optic axis earlier (P") than those near the centre of the lens (P') . The area circled C is known as the centre of confusion.

Spherical aberrations are not caused by the manufacture of the lens, but are a result of the laws of refraction at curved surfaces. They limit the practical and acceptable magnification of the magnifying lens to around x2 or x3.

Both of these problems (spherical aberrations and dependence of eye distance on magnification) are reduced by the compound microscope (Figure 3.8), which in simple terms uses a magnifying lens to produce a virtual image which an eye piece then projects into the eye, producing greater magnification.

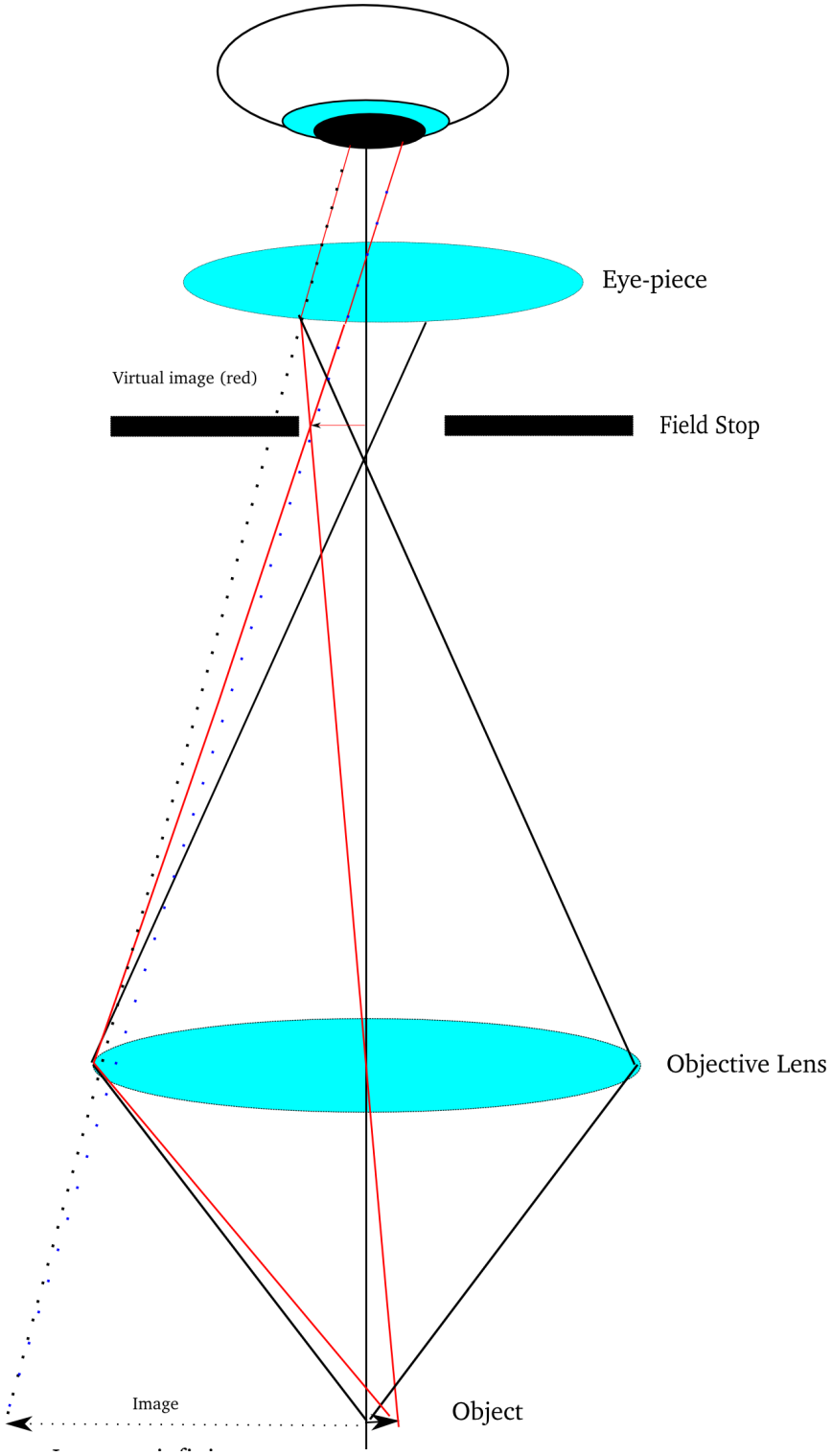

Figure 3.8: Ray diagram of compound microscope

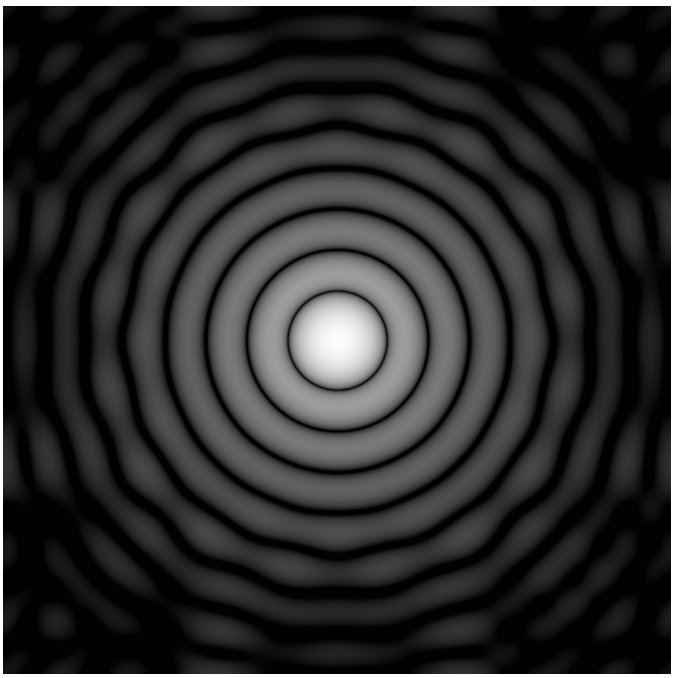

Figure 3.9: An airy disc, produced in ImageJ by performing an FFT on a circular aperture

This setup, while more complex, leads to greater magnifications than are possible in the simple magnifying glass system. However, it is not sufficient to have infinitely great magnification as there comes a point in which one does not gain any more detail, such a limit is called the resolving power of the lens, or optical system.

3.6.1 Resolving Power

An illuminated circular aperture, such as those in a microscope, will produce a diffraction pattern known as an Airy disk, as shown in Figure 3.9. This involves a bright centre spot with every increasing large circles of light around it. The dimensions of the bright spot and the concentric rings is determined by the diameter of the aperture and the illumination light, such that:

$$\sin\theta_2 = 1.22\frac{\lambda}{D} \tag{3.8}$$

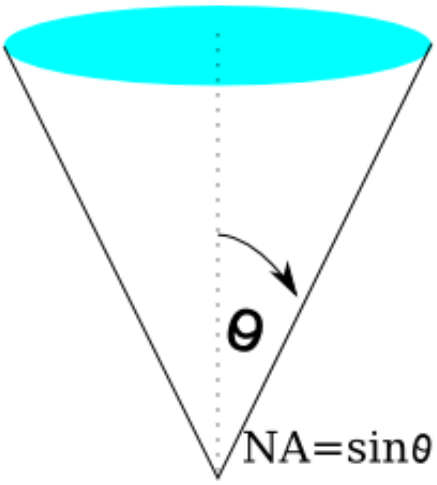

Figure 3.10: Numerical aperture of an objective lens

Where θ_2 is the annular radius of the second dark ring, λ is the illumination wavelength and D is the diameter of the aperture. Thus, for larger wavelengths, the radius of concentric rings increases, and vice versa for the diameter of the aperture.

The Rayleigh criterion relates this to the resolving power of a microscope stating that

> "Objects are just barely resolved if the centre of one diffraction pattern coincides with the first minimum of the other"

This distance from the centre to the first minimum is equal to and therefore the resolution of a microscope objective can be expressed as

$$\text{resolution} = 1.22\frac{\lambda}{NA} \tag{3.9}$$

Where NA is the numerical aperture (Figure 3.10) of the objective lens, and a higher value will result in a tightening of the Airy disks meaning closer lying objects can be resolved. In physical terms, the numerical aperture is the sine of the half angle of the cone of acceptance of the objective.

As an example, a typical x20 magnification microscope objective will have an NA of 0.4[1] which provides a resolution of 0.69 μm. The micro-structures of dental enamel, as discussed in chapter 2, are of around 1μm in dimensions and therefore it is possible to produce high resolution images of dental surfaces using such an objective.

However, the main problem with this type of microscope is that sub-surface imaging is tricky. There is no rejection of light in a compound microscope and therefore if the focal point is positioned below the surface of an object, the out-of focus light from the surface is still recorded leading to a blurry image. This is explained diagrammaticality in Figure 3.11 where the microscope has been replaced by a single lens representing the optics. Light is emitted from a source and propagates through a beam-splitter to the lens. There are then two reflection pathways shown in green (representing the surface reflection) and red (representing the sub-surface object of interest at the focal point),

Both the green and red rays arrive at the photo-detector (PD) and are thus recorded as part of the image. As can be inferred, it would be very difficult to distinguish between the two reflection pathways since, in the real application, the ray paths would not have the green and red colouring!

Confocal microscopy is an adaptation to microscopy which provides for the out-of-focus problem. The rest of this chapter will deal with confocal microscopy in view to produce a fibre optic based system for the diagnosis of dental disease.

3.6.2 The confocal microscope

Confocal microscopy was invented in 1957 by Marvin Minksy while working as a Junior Fellow at Harvard (Minsky, 1957). A ray diagram of the concept is shown in Figure 3.12, whereby a point source (Minksy used an emission lamp, however, modern day set-ups use laser sources, for reasons to be discussed in a following

[1] http://www.microscopyu.com/articles/formulas/formulasresolution.html

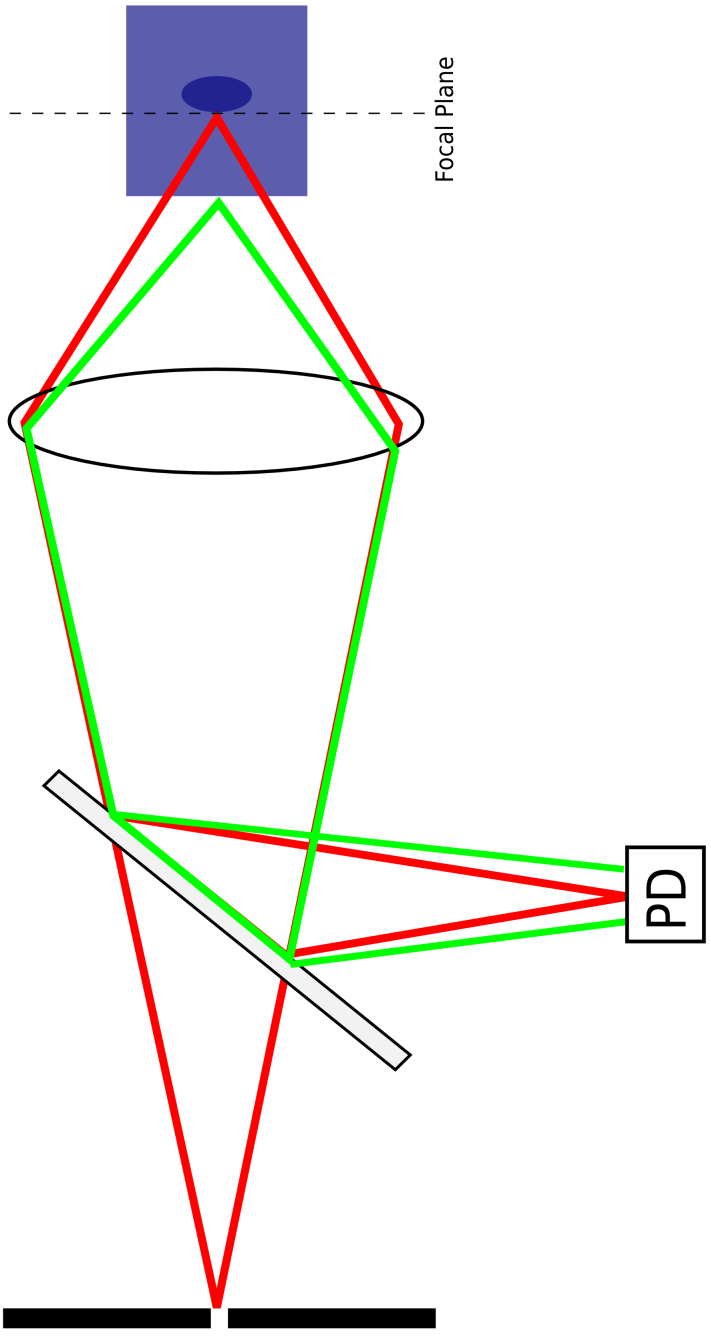

Figure 3.11: Signal collection in conventional micorscope.

section) is emitted through a beam splitter. As with the microscope, there are two main ray reflection pathways, namely out of focus light and in focus light.

The key difference with a confocal microscope to a conventional microscope is the small aperture which is placed over the photodetector. This is to reduce the active surface area of the photodetector so that only light which is tightly focused on the surface is recorded. As shown in Figure 3.12, light reflected from the sub-surface object of interest (illustrated in red) is focussed tightly through the aperture and is thus recorded on the photodetector. The light reflected from the surface of the object (illustrated in green) is not adequately focussed when it reaches the aperture and is thus blocked from registering all but a partial signal on the photodetector.

Thus in a practical application with a semi-transparent object (at the source wavelength), for example a cell, optical sections can be produced by moving the focal point of the microscope through the cell and recording the reflected, or fluorescence, intensity from the focal point. Areas of different optical properties (due to scattering and absorption effects) at the focal point will produce different reflection intensities, and thus subsurface images can be built up.

Image formation in scanning microscopes

Two dimensional optical sections are created by 'steering' the focal point in the X-Y plane. The reflection intensity is then recorded in a point by point manner. A high NA objective lens will allow a sub-micron spot-size which will result in a high resolution optical section being produced (Shotton, 1989). Three dimensional images can also be produced by recording multiple X-Y sections at different Z locations (by moving the focal point through the cell for each section).

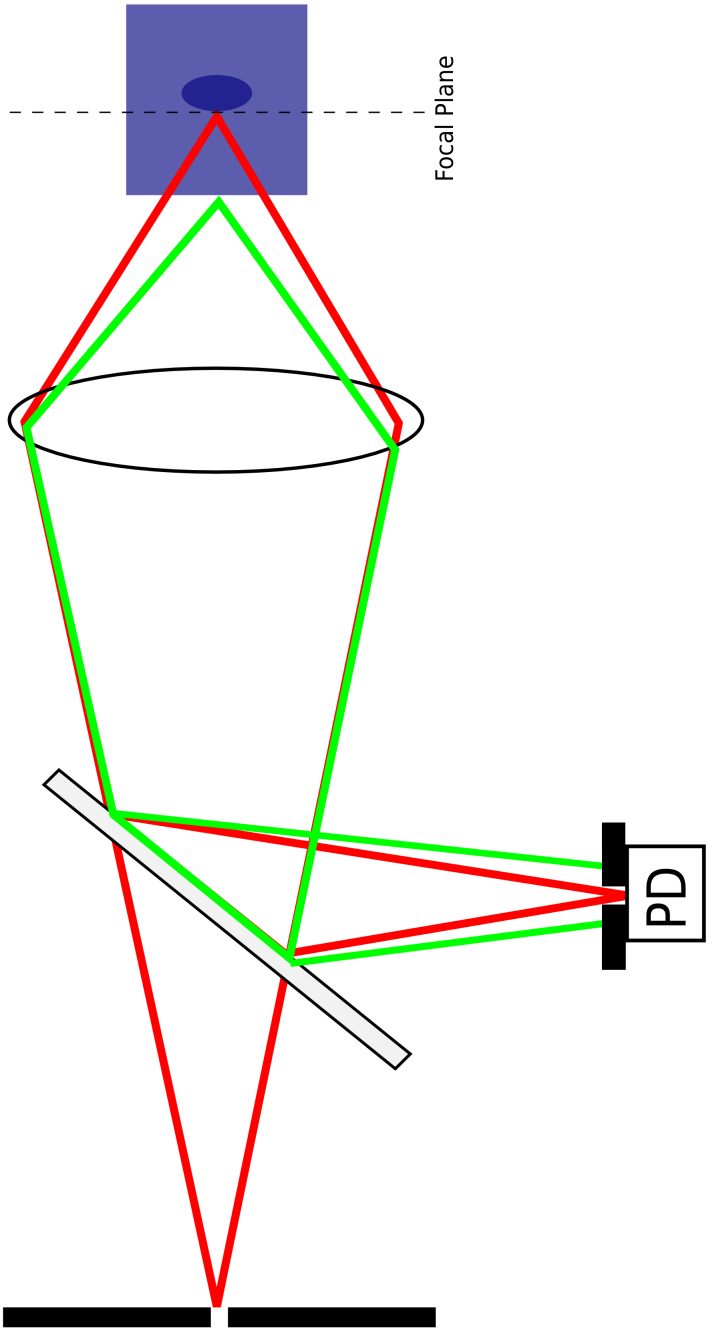

Figure 3.12: Signal detection in confocal microscope showing rejection of out of focus light.

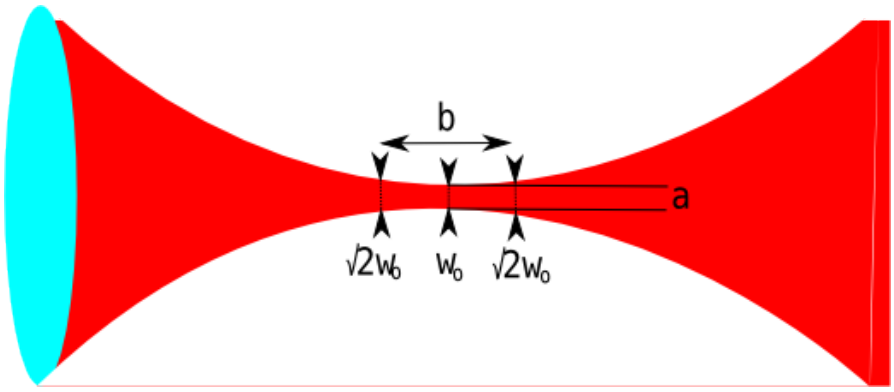

Figure 3.13: Exaggerated diagram showing lateral (a) and axial resolution (b) for a Gaussian beam profile

Resolution

There are two types of resolution to be considered in a confocal microscope system which is to produce three-dimensional images (lateral and axial). These are both shown in an exaggerated fashion in Figure 3.13. The lateral resolution (Figure 3.13a) determines the detail in each plane and is basically governed by Rayleigh's criterion as discussed previously. The axial resolution (Figure 3.13b) depends on the confocality of the system and determines how 'thin' an optical slice can be recorded.

The confocality of the system is determined by both the objective lens and the pinhole of the system. The objective lens focusses the light down to a point, however, with any light beam, the focus will not be an infinitely small point; instead it will be an area of minimum beam-waist. The confocality is measured as the distance between the two points in the beam where the width, for a Gaussian beam (such as that from a laser source) is equal to $\sqrt{2}w_0$. It is also mathematically expressed as

$$b = \frac{2\pi {w^2}_0}{\lambda} \tag{3.10}$$

Where w_0 is the minimum beam waist and is related to the lateral resolution calculated from the Rayleigh Criterion. From this expression it is easy to infer that a lens which tightly focuses the beam with a short focal length will thus

have a short confocal parameter and thus be able to produce very thin optical sections.

The second part of the system which controls the thickness of an optical section is the pinhole at the photo detector. Most systems allow this aperture to be varied in diameter from fully open (when the system would be acting in a non-confocal way) to fully closed. The optimum size of the pinhole lets sufficient light through that there is good contrast and also sufficient detected light in the image recorded while keeping a good degree of confocality.

Making the pinhole less than w_0 the system would in theory be highly confocal, however, the small amount of light recorded on the photo diode may lead to very poor images. In the other case, a pinhole much larger than the size of the beam waist would lead to very bright images but at the expense of confocality. Thus the choice of pinhole size is not trivial and differs between applications.

Applications of confocal microscopy

The ability of confocal microscopy to produce high resolution optical slices has revolutionised the biological sciences and a full review would be outside the scope of this chapter. It has been shown to be useful in ophthalmic applications for rapid diagnosis (Masters and So, 2001) of complaints. There has also been work published to show its usefulness as a skin imaging modality (Calzavara-Pinton et al., 2008). The field of cell biology and imaging has seen a great deal of work carried out with a good review being (Shotton, 1989). The detection of lung cancer has also been investigated as a use for the technique (Lane et al., 2009). Outside of the biological field, confocal microscopy has also been investigated as a method of providing three dimensional optical storage for computers.

Multi-photon confocal microscopy

For completeness, a word should be said about multi-photon confocal microscopy and its application in dentistry. Multi-photon microscopy is a technique allowing higher optical resolutions than conventional confocal microscopy. It acheives this by utilising a non-linear effect known as energy doubling, whereby a fluophore will only be excited where two photons of double the required wavelength are incident at exactly the same time(Lin et al., 2011). The probability of this happening is very low, and therefore it only occurs at the focal region of a high NA objective. A pulsed laser is also used to increae the number of photons incident in the focal region, and because collected emmited photon's can only result from this area, an image can be built up with high spatial resolution.

This technique has been demonstrated for imaging carious tissues with thin optical slices (0.35μm) up to 200μm below the surface of the tooth. A further advance in this technique known as second harmonic generation has also been shown to work in distinguishing healthy dentine from carious dentine (Lin et al., 2011). This arises due to SHG's reliance on microstructure producing the non-linear effect, with caries breaking down the dentine's collange fibre matrix (the main source of the auto-fluorescence (Lin et al., 2011) at 375nm) and reducing the collected fluorescence.

Due to the point-scanning method of building up the images, and the low photon counts, multiphoton microscopy is still a lab-based method. Further research in to video rate imaging techniques is required before it could be envisaged in the dental clinic.

3.6.3 Summary

Confocal microscopy revolutionised biological sciences with the ability to create high resolution three dimensional images. However, for in-vivo dental imaging, the bulky optics for imaging lead to quite a disadvantage due to the limited

space inside the oral cavity. The rest of this chapter shall concentrate on an adaptation to confocal microscopy that allows depth profiles to be recorded using micro-optics.

3.7 Fibre optic confocal microscopy

The standard confocal microscope set-up has a few features which make it unsuitable for in vivo biological work. Namely the bulky optics required for beam scanning and focussing. A fibre optic confocal microscope (FOCOM) is an adaptation whereby the scan head is removed from the rest of the system by incorporating a single mode optical fibre instead of a pinhole (Kimura and Wilson, 1991). This allows for the separation and miniaturisation of the scan head into a hand held probe.

3.7.1 Single mode fibre as a pinhole

In a conventional confocal system a pinhole aperture is used to distinguish between in and out of focussed light, with FOCOM a single mode optical fibre (SMF) is used instead. The light is coupled into the fibre by focussing a collimated beam of light into the fibre. Any light that is not collimated (and of the wavelength for the fibre to operate as a single mode fibre) does not get sufficiently focussed and is thus rejected.

The act of rejecting uncollimated light can be used on the 'exit' end of the fibre to produce a miniature confocal microscope hand-piece as shown in Figure 3.14. Light exits the fibre and is collimated by the first lens. This collimated beam of light is then focused by the second lens which acts as an objective lens. Light reflected from the focal point of the objective lens is collimated and thus returned down the fibre, any other light is rejected, giving a confocal action.

A schematic of a typical FOCOM set up is shown in Figure 3.15. The laser

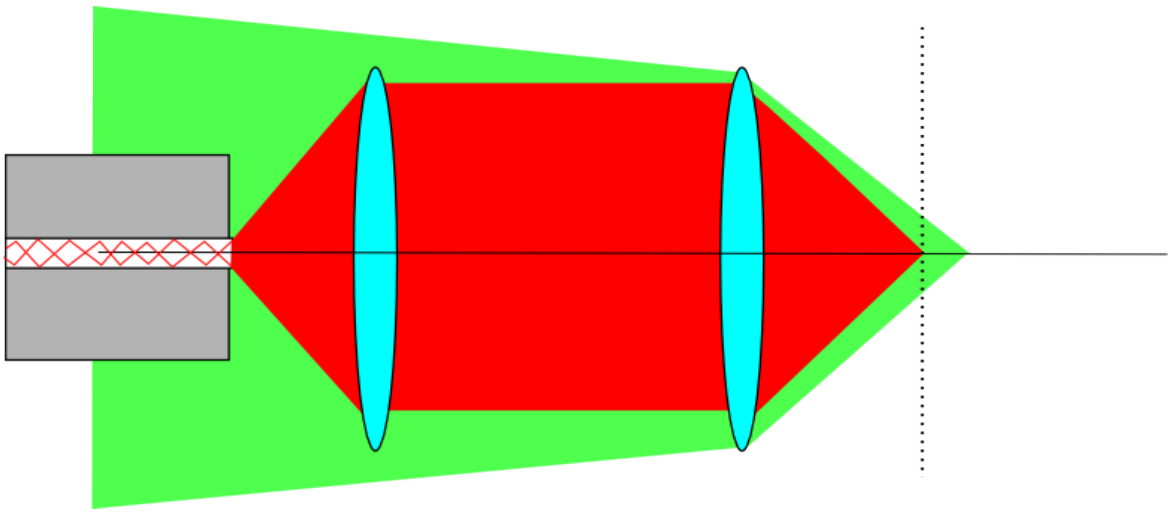

Figure 3.14: A single mode optical fibre acting as pinhole in FOCOM.

is contained inside a box which also holds the initial fibre coupling optics and photodetector. A fibre optic cable connects the hand piece to the rest of the system. This has its advantages in that the fine alignment needed for coupling laser light into a SMF is contained inside a packaging and out of reach of a non-technical user.

The performance of a FOCOM now depends on the SMF, collimating lens and the objective lens. Figure 3.16 demonstrates the effects of the numerical aperture differences between the SMF and the collimating lens. Figure 3.16a shows the case where the numerical aperture of the fibre, NA_{fibre} is greater than that of the collimation lens, NA_{collim}. The light exiting the fibre is highly divergent and due to the lower NA_{collim} value, not all this light is collected by the lens (illustrated by the darker region of light leaving the SMF). Therefore the return signal will be lower than if this light was collected and transmitted to the objective lens. Such a set up is said to be lens dominated because the lens controls how much light is 'used' (or collected) from the fibre (Dabbs and Glass, 1992).

The second case is if $NA_{collim} > NA_{fibre}$, where a fibre dominated system arises (Dabbs and Glass, 1992), as shown in Figure 3.16b. This time, all the light is collected by the lens and collimated. However, the resolution of the system

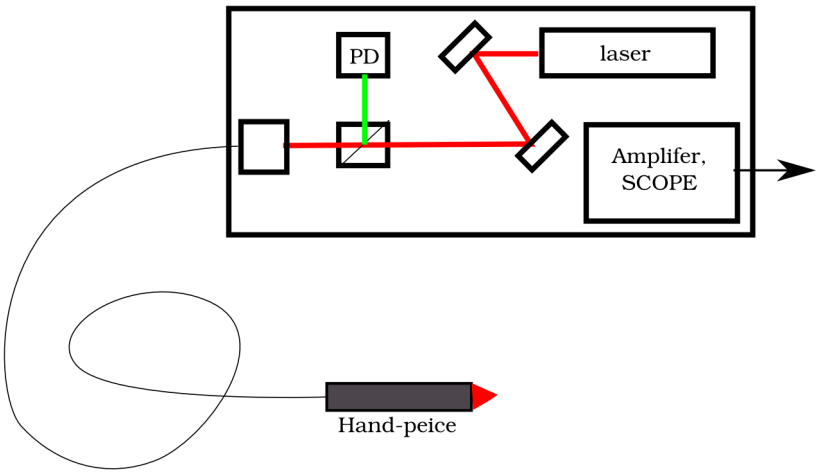

Figure 3.15: Schematic of a FOCOM system showing the separation of the laser optics and the confocal hand piece

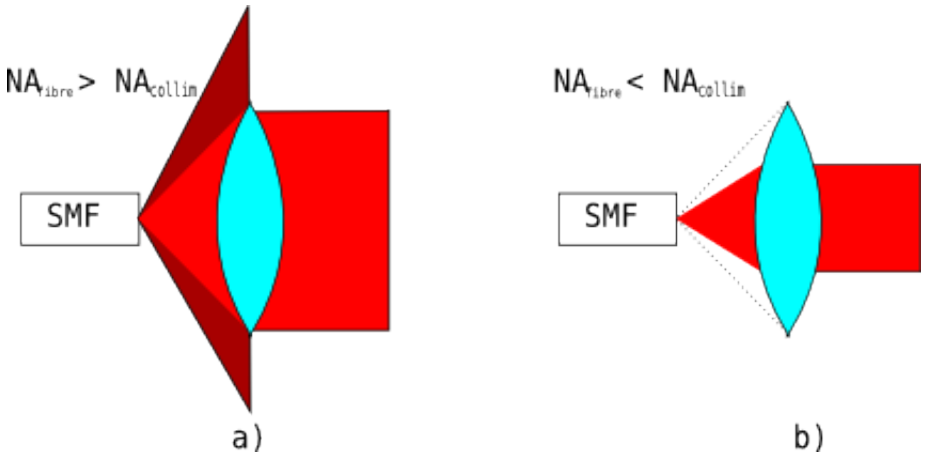

Figure 3.16: A single mode fibre acting as a pinhole can give either a) a lens or b) fibre dominated system

suffers in that the width of the collimated beam is less than if the lens had been backfilled. This reduces the effective NA of the objective length and leads to a longer confocal factor.

Thus the choice of lens for collimating the light output from the single mode fibre should be a trade off between an increased return signal intensity (for example with a high power lasers) or a reduced optical slice thickness (if a low powered laser is available). In the case where $NA_{fibre} = NA_{collim}$ there is a maximum intensity transfer between the fibre and the lens but the system is not truly confocal (Dabbs and Glass, 1992).

3.7.2 Application to dental disease

The ability of FOCOM to detach the scanning optics from the rest of the confocal system is of great use for the oral environment. This is of interest for the detection of dental caries where subsurface lesions are an early manifestation of the disease. The subsurface lesions have a different optical property to sound enamel, and as such produce a different reflection and backscattered intensity. By scanning the focal point of a FOCOM system through a suspected area of caries and recording the reflection intensity at each point, a depth profile can be produced which shows the front and back surfaces of the lesion underneath the enamel surface (Rousseau et al., 2007).

What now follows is a description of a desktop FOCOM set up which has been used to detect early dental caries. From this a discussion of its advantages and disadvantages will arise and shall serve as a good basis for the following two chapters where the miniaturisation of the scanning optics is discussed before a miniature scan head is used to measure sub-surface caries lesions.

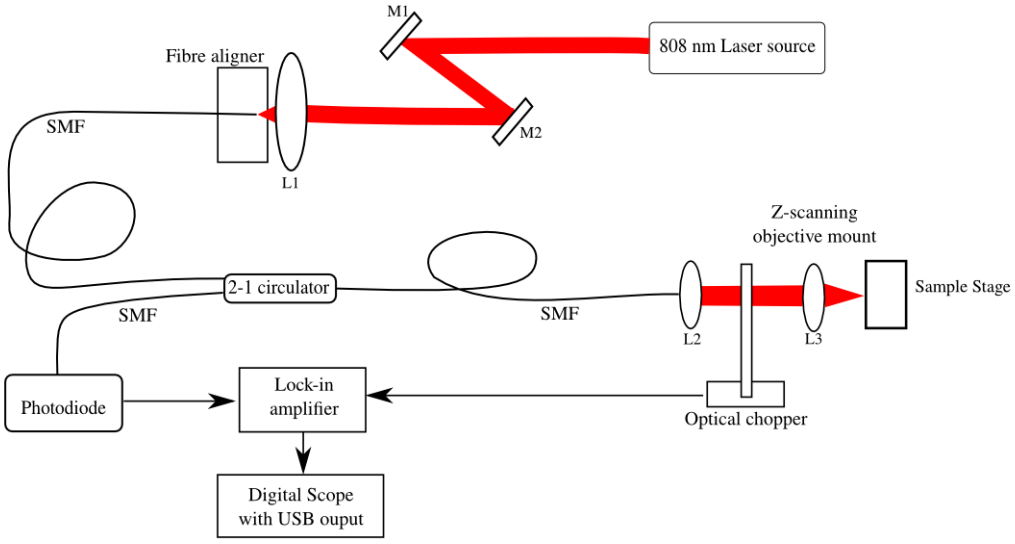

Figure 3.17: Basic desktop FOCOM setup as demonstrated in Rouseau et all (2007)

3.7.3 A fibre optic system for the detection of dental disease

Figure 3.17 shows the basic set-up for a desk-top confocal system which was used by Rouseau et al (2007) to detect early caries lesions. The 808nm laser light source (chosen due to the transparency of enamel at this wavelength (Fried et al., 1995)) is coupled into a single mode optical fibre using a x20 objective (L1 in Figure 3.17). The fibre is connected to a 2-1 circulator which acts as the beam splitter, and also allows total confinement of the laser light until the handpiece. The light exiting the single mode fibre was collimated using a 0.276NA (L2 in Figure 3.17) objective and focused to a tight focal point using a x40 0.55NA objective lens (L3 in Figure 3.17). This objective lens was mounted on to a translation stage which allowed it to be moved backwards and forwards at a constant speed. The light that was reflected is sent back into the fibre and directed via the circulator to a photodiode for recording the reflection intensity. An optical chopper is incorporated in order to increase the signal to noise ratio, and also to allow discrimination between reflection from the sample and those from the bare ends of the fibres.

The work of Rousseau et al (2007) demonstrated that a fibre optic confocal microscopy could be used to detect early caries lesions. However, the set-up used still incorporated bulk optics for the scan head, and as such was not suitable for in-vivo investigation. Therefore there were two aspects to consider for the miniaturisation of this set-up: 1) the lenses incorporated as the collimation and objective optics and 2) the method in which the objective optic would be scanned backwards and forwards. The following chapter is devoted to the miniaturisation of the hand piece and will discuss the choice of optical components and the miniature scan stage. This will lead on to a subsequent chapter where the hand piece is used for detecting dental disease.

Bibliography

Bennett T. Amaechi and Susan M. Higham. Quantitative light-induced fluorescence: A potential tool for general dental assessment. *Journal of Biomedical Optics*, 7(1):7–13, 2002. doi: 10.1117/1.1427044. URL `http://link.aip.org/link/?JBO/7/7/1`.

B. Angmar-Maansson and J.J. Ten Bosch. Optical methods for the detection and quantification of caries. *Advances in Dental Research*, 1(1):14–20, 1987. doi: 10.1177/08959374870010010601. URL `http://adr.sagepub.com/content/1/1/14.abstract`.

H Bjelkhagen, F Sundstrom, B Angmar-Mansson, and H Ryden. Early detection of enamel caries by the luminescence excited by visible laser light. *Swed Dent J*, 6(1):1–7–, 1982. URL `http://ukpmc.ac.uk/abstract/MED/6951310`.

Piergiacomo Calzavara-Pinton, Caterina Longo, Marina Venturini, Raffaella Sala, and Giovanni Pellacani. Reflectance confocal microscopy for in vivo skin imaging. *Photochemistry and Photobiology*, 84(6):1421–30, 2008. ISSN 0031-8655. doi: 10.1111/j.1751-1097.2008.00443.x. URL `http://www.ncbi.nlm.nih.gov/pubmed/19067964`. PMID: 19067964.

W F Cheong, S A Prahl, and A J Welch. A review of the optical properties of biological tissues. *IEEE Journal of Quantum Electronics*, 26(12):2166–2185, 1990. URL `http://ieeexplore.ieee.org/xpls/abs_all.jsp?arnumber=64354`.

B. Colston, U. Sathyam, L. DaSilva, M. Everett, P. Stroeve, and L. Otis. Dental OCT. *Optics Express*, 3(6):230–238, 1998.

T. Dabbs and M. Glass. Fiber-optic confocal microscope: FOCON. *Appl. Opt*, 31(16):3030–3035, 1992.

G M Davies, H V Worthington, J E Clarkson, P Thomas, and R M Davies. The use of fibre-optic transillumination in general dental practice. *Br Dent J*, 191(3):145–147, 2001. ISSN 0007-0610. doi: 10.1038/sj.bdj.4801123. URL `http://dx.doi.org/10.1038/sj.bdj.4801123`.

Elbert de Josselin de Jong, Susan M. Higham, Philip W. Smith, Catherina J. van Daelen, and Monique H. van der Veen. Quantified light-induced fluorescence, review of a diagnostic tool in prevention of oral disease. *Journal of Applied Physics*, 105(10):102031, 2009. doi: 10.1063/1.3116138. URL `http://link.aip.org/link/?JAP/105/102031/1`.

D. Fried, R. E. Glena, J. D. B. Featherstone, and W. Seka. Nature of light scattering in dental enamel and dentin at visible and near-infrared wavelengths. *Appl. Opt*, 34(7):1278Â1285, 1995.

D Huang, EA Swanson, CP Lin, JS Schuman, WG Stinson, W Chang, MR Hee, T Flotte, K Gregory, CA Puliafito, and al. et. Optical coherence tomography. *Science*, 254(5035):1178–1181, November 1991. doi: 10.1126/science.1957169. URL `http://www.sciencemag.org/cgi/content/abstract/254/5035/1178`.

R. Jones, G. Huynh, G. Jones, and D. Fried. Near-infrared transillumination at 1310-nm for the imaging of early dental decay. *Optics Express*, 11(18):2259–2265, 2003.

R S Kahan, K Gulabivala, M Snook, and D J Setchell. Evaluation of a pulse oximeter and customized probe for pulp vitality testing*. *Journal of En-*

dodontics, 22(3):105–109, March 1996. doi: 10.1016/S0099-2399(96)80283-4. URL http://www.sciencedirect.com/science?_ob=ArticleURL&_udi=B82X7-4NW57SB-1&_user=10&_rdoc=1&_fmt=&_orig=search&_sort=d&_docanchor=&view=c&_searchStrId=959286994&_rerunOrigin=scholar.google&_acct=C000050221&_version=1&_urlVersion=0&_userid=10&md5=e23bfc2a44f1be27be08e76801d2310c.

A. Kienle and R. Hibst. Light guiding in biological tissue due to scattering. *Physical Review Letters*, 97(1):18104, 2006.

S Kimura and T Wilson. Confocal scanning optical microscope using single-mode fiber for single detection. *Applied Optics*, 30:2143–2150, June 1991. URL http://adsabs.harvard.edu/abs/1991ApOpt..30.2143K.

K. KONIG, G. FLEMMING, and R. HIBST. Laser-induced autofluorescence spectroscopy of dental caries, 1998. Anglais.

P. M. Lane, S Lam, A McWilliams, J. C. leRiche, M. W. Anderson, and C. E. MacAulay. Confocal fluorescence microendoscopy of bronchial epithelium. *Journal of Biomedical Optics*, 14(2):024008–10, March 2009. URL http://link.aip.org/link/?JBO/14/024008/1.

Po-Yen Lin, Hong-Chou Lyu, Chin-Ying Stephen Hsu, Chia-Seng Chang, and Fu-Jen Kao. Imaging carious dental tissues with multiphoton fluorescence lifetime imaging microscopy. *Biomed. Opt. Express*, 2(1):149–158, Jan 2011. doi: 10.1364/BOE.2.000149. URL http://www.opticsinfobase.org/boe/abstract.cfm?URI=boe-2-1-149.

A. Lussi, R. Hibst, and R. Paulus. DIAGNOdent: an optical method for caries detection. volume 83, pages 80–83. IADR, 2004.

B. R. Masters and Peter So. Confocal microscopy and multi-photon excitation

microscopy of human skin in vivo. *Optics Express*, 8:2, January 2001. URL http://adsabs.harvard.edu/abs/2001OExpr...8....2M.

D McComb and L. E. Tam. Diagnosis of occlusal caries: Part i. conventional methods. *J Can Dent Assoc*, 67(8):454–7, 2001.

M Minsky. Microscopy apparatus, 1957. URL http://www.freepatentsonline.com/3013467.html.

I. A. Pretty. Caries detection and diagnosis: Novel technologies. *Journal of Dentistry*, 34(10):727–739, 2006.

I. A. Pretty and G. Maupome. A closer look at diagnosis in clinical dental practice: Part 5. emerging technologies for caries detection and diagnosis. *J Can Dent Assoc*, 70(8):540, 2004.

G Ross. Caries diagnosis with the DIAGNOdent laser: a user's product evaluation. *Ontario Dentist*, 76(2):21–24, March 1999. ISSN 0300-5275. URL http://www.ncbi.nlm.nih.gov/pubmed/10518890. PMID: 10518890.

C. Rousseau, S. Poland, J. M. Girkin, A. F. Hall, and C. J. Whitters. Development of Fibre-Optic confocal microscopy for detection and diagnosis of dental caries. *Caries Research*, 41(4):245, 2007.

D.M Shotton. Confocal scanning optical microscopy and its applications for biological specimens. *J Cell Sci*, 94(2):175–206, October 1989. URL http://jcs.biologists.org/cgi/content/abstract/94/2/175.

D. Spitzer and J. Ten Bosch. The absorption and scattering of light in bovine and human dental enamel. *Calcified Tissue International*, 17(2):129–137, April 1975. doi: 10.1007/BF02547285. URL http://dx.doi.org/10.1007/BF02547285.

G. K. Stookey. Optical Methods-Quantitative light fluorescence. volume 83, pages 84–88. IADR, 2004.

P Tipler and R Llewellyn. *Modern Physics*. Worth Publishers Inc.,U.S., 3rd revised edition edition, April 1999. ISBN 1572591641.

Chapter 4

Micro-optics for the oral cavity

4.1 Introduction

Before any tool is suitable for the detection of dental disease in-vivo, the size of the system must be optimal for entering the oral cavity. Previous work into using fibre optic confocal microscopy has utilised standard desk-top optics, and with most of the lenses being 2“ in diameter (Rousseau et al., 2007), these are unsuitable for use in the mouth.

This chapter therefore reports on the choice of the miniature lenses for use in the oral cavity, where two choices of lenses are characterised and their advantages and disadvantages are compared. The final choice is then utilised in the next chapter to diagnose and detect dental disease in a miniature system.

The two types of lenses that shall be compared are Gradient Refractive Index Lenses (GRIN) and aspheric lenses. In order to characterise the GRIN lenses, a computer simulation is used before verifying the results with a desktop based system. With aspheric lenses, the Rayleigh criterion and Dabbs and Glass method (Dabbs and Glass, 1992) were used to calculate hypothetical resolutions and a similar desktop based system to that of the GRIN verification is used to verify these.

4.2 Traditional Lenses

Traditional lenses rely on two properties to alter the incoming light wave. The first property is the difference in refractive index of the lens medium and its surroundings, which from Snell's law alters the change of the wave's direction by

$$n_1 \sin\theta_1 = n_2 \sin\theta_2 \tag{4.1}$$

However, as can be seen by this equation, the direction is not altered for waves incident to the normal of the boundary (if $\theta_1 = 0$, then $\sin\theta_1 = 0$), therefore a

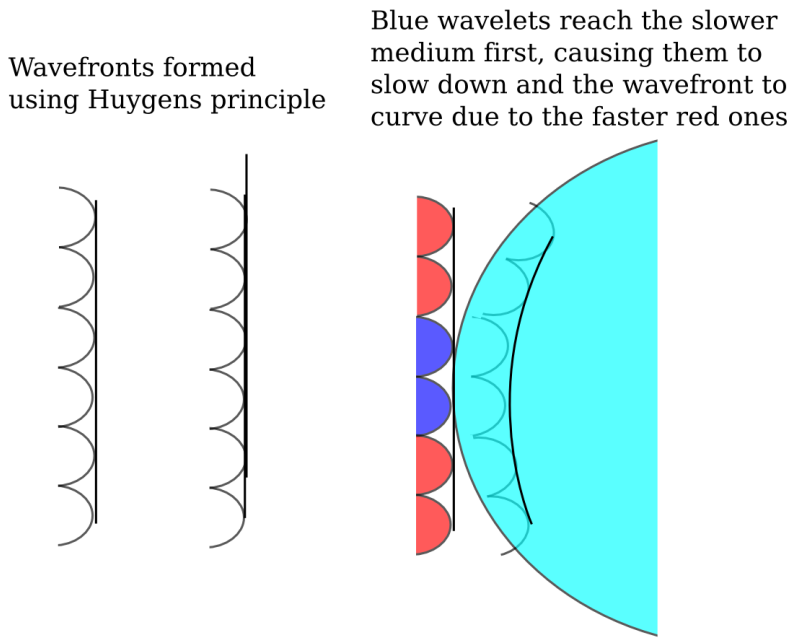

Figure 4.1: Focusing with a traditional lens

second property of curvature is used. This means that for the wave incident on the lens, most of the wave front is incident at an angle to the normal, causing focussing. This can also be explained using Huygen's principle to say that the curvature creates an optical path length difference between different wavelets incident on the lens as shown in figure 4.1).

4.3 Aspheric Lenses

Aspheric lenses are a very common optical component, with applications ranging from military viewfinders to bifocal spectacles. They were first mentioned in the 9th century by the Muslim scientist Ibn Sahl who, through developing what would later be known as Snell's Law, developed the shape of lenses in order to reduce aberrations. Further work was carried out by Descartes and Huygens, although this seems to be more from a trial and error method into polishing lenses to the desired shape, rather than with any optics theory.

Aspheric lenses have a uniform refractive index and use a curved face in order

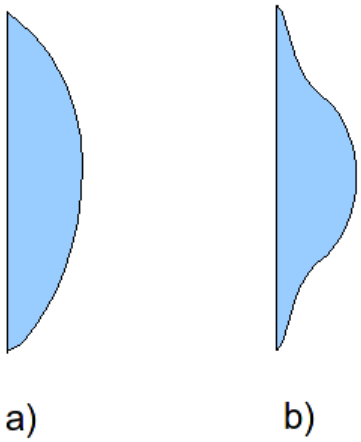

Figure 4.2: The curvature of a traditional (a) lens compared to that of an aspheric (b) lens

to focus light. Typical standard lenses have a curved face that is spherical and therefore are subject to spherical aberrations as discussed in Chapter 3. An aspheric lens fixes this issue by having a non-spherical curved face (as shown in Figure 4.2), and therefore rays from the outer edges are reflected in a different manner to those near the centre. These reductions in aberrations mean that, under ideal conditions (full back-aperture filling) the resolution provided by the aspheric lens can be said to be diffraction limited.

There has been much work carried out in to aspheric lenses for confocal purposes and as such the bulk of the theoretical aspect of this chapter focuses on introducing GRIN lenses for confocal systems. Where the theoretical characteristics of the aspheric lenses are needed, data sheets from manufacturers provide ample information for estimating axial resolutions.

What now follows is an introduction to the various properties and characteristics of GRIN lenses. A computer simulation of a GRIN lens material for the one dimensional confocal application will be used to calculate the available resolution of a specified GRIN lens. After this has been discussed, an FOCOM system as described in the previous chapter will be used to compare and contrast the GRIN

lens experimentally against an aspheric lens.

4.4 GRIN lenses

GRIN (Gradiated indice) lenses are an attractive option for this body of work due to their size and form factor. Traditional lenses have a strong connection between their size and their ability to collect and focus light, ranging from a few centimetres on an optics bench to the meter diameters found in astronomical telescopes. This body of work predominantly concerns dental imaging and therefore the common environment for imaging is the oral cavity. This puts a limit on the dimensions of the optics which can be used comfortably (and practically) for the purpose.

GRIN lenses only use the refractive index property to focus light (Marchand, 1982). GRIN lenses come in two forms, namely Radial and Axial GRIN lenses. The former exhibits a change in refractive index as a function of radial distance from the optic axis, and the latter as a function of distance along the optic axis. This creates an optical velocity gradient through the material, and due to restrictions on the optical path length of different wavelets, exhibits a focussing of the wave. For this work, however, only radial GRIN lenses shall be considered.

GRIN lenses can be manufactured to be low diameter (1.8mm) glass rods, much like a fibre optic cable. As will be shown, GRIN lenses can be produced to facilitate use with fibre optics and remove the complex optical set-ups associated with bulk optics.

4.4.1 GRIN Profile

As stated before, the property of the GRIN lens that allows for focussing is its varying refractive index. In order to understand how this allows for focussing, consider a rowing boat in a lake. If one is to row one paddle faster than the

other, then the boat starts to change direction. With GRIN lenses, the change in refractive index means that for light propagating through the medium, one edge of the ray has a slightly increased speed and thus changes the direction of propagation through rotation of the ray.tab:scattering

This refractive index gradient can be present axially or radially and it is the latter that will be considered in this chapter. Through geometric ray optics, the refractive index profile for a standard GRIN lens is found to be of the form

$$n(r) = n_0(1 - \frac{r^2 g}{2}) \tag{4.2}$$

Where n_0 the refractive index at the centre of the GRIN lens. The parameter of this expression, r, is the distance away from the centre of the lens, and g is a constant value which controls the gradient of refractive index.

As the ray propagates through the length of GRIN media, the pathway oscillates around the optic axis due to the symmetry of the profile. This gives rise to the intrinsic property of *pitch*.

4.4.2 Pitch

Due to the method in which they focus light, the length of the lens plays a part in the action of the lens, as shown in Figure 4.3. As mentioned above, the path of a ray through GRIN material oscillates around the optic axis. The 'natural' length of a GRIN lens is the length in which the GRIN profile allows for one full oscillation, this length has the lensing effect that takes a point on one face of the material and images it to the other face. A GRIN lens cut to its natural length is said to have a pitch of 1.

Other focusing effects can be produced by grinding the lens to different lengths to produce fractional pitches, for example, if the lens has a pitch of 0.5 (which means it is half its natural length) then an object will be imaged inversely on the

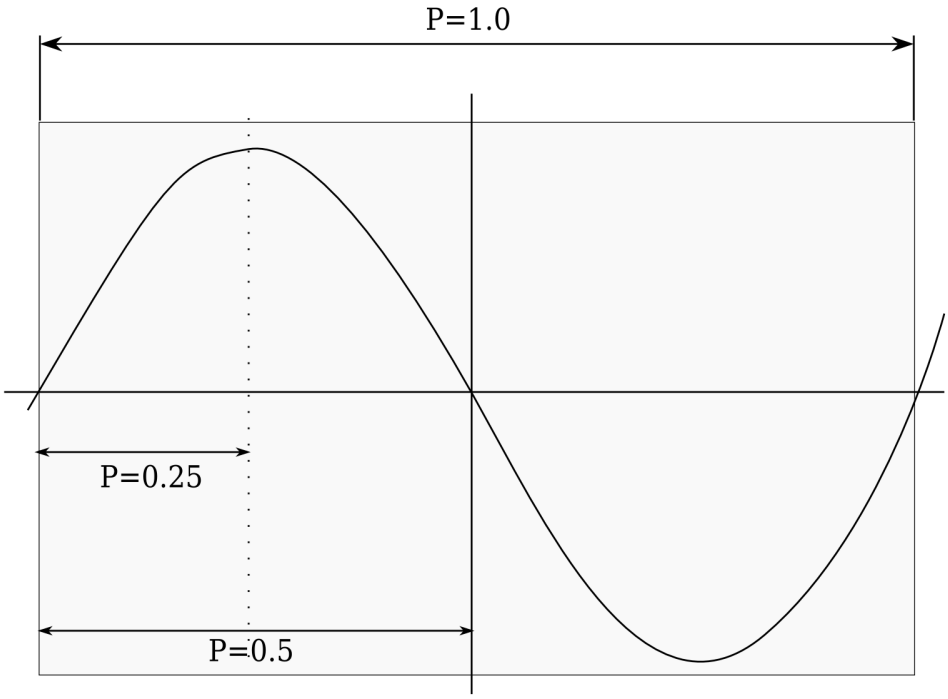

Figure 4.3: Diagram explaining the property of pitch for GRIN lenses

other face, as shown in Figure 4.3.

One useful pitch for work with optical fibres is that of 0.25, whereby a point source on one face will produce a collimated output beam. For this work, a slightly longer pitch of 0.29 is considered. This pitch allows a point that is slightly away from one face to be focussed to a point that is external to the opposite GRIN face, as shown in Figure 4.4.

4.4.3 Ray Tracing

In conventional ray tracing programs, the media in which light propagates through are assumed to have homogeneous refractive indices. This allows easy application of Snell's law and basic geometry for calculating the ray pathway. However, as stated, GRIN lenses have an inhomogeneous refractive index, and as such a different method has to be incorporated.

One method is to use an iterative numerical integration scheme such as the Runge-Kutta version 4 on a modified Eikonal equation (Sharma et al., 1982).

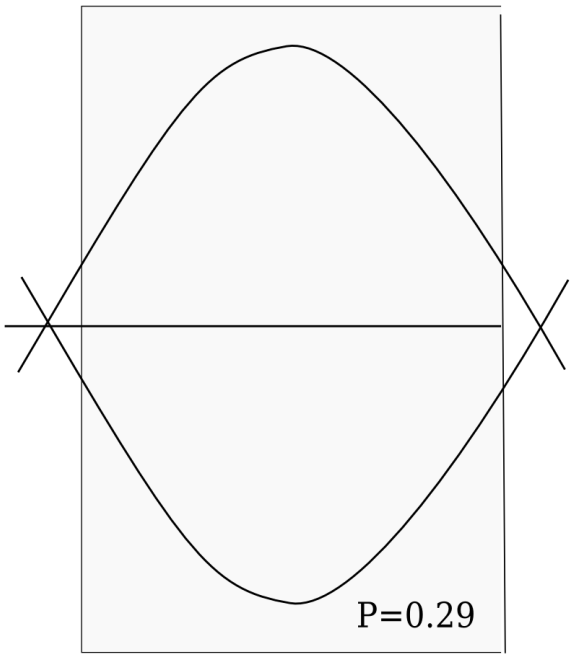

Figure 4.4: GRIN lens material with a pitch of 0.29

The Eikonal equation relates the optical path of a ray passing through a medium to the refractive index of the medium, given by :

$$(\nabla L(\mathbf{r}))^2 = n^2 \tag{4.3}$$

Where $L(\mathbf{r})$ is the optical path of the ray as it propagates through the medium. n^2 is the square of the refractive index of the medium. This equation is derived using Maxwell's equations and a full derivation can be found in (Landis and Seliskar, 1995). It is of note that in the derivation of the Eikonal equation, the assumption that the refractive index in the medium is constant is never made, and therefore this equation holds for a material with a varying refractive index.

The Eikonal equation can thus be adapted to be of use with a GRIN lens. This is achieved by rearranging the equation into a differential equation which can be solved using a numerical algorithm such as Runge Kutta. To start, a unit

vector which points along the path of the ray, s, is defined such that

$$s = \frac{\nabla L(\mathbf{r})}{n} \tag{4.4}$$

This can also be defined as

$$s = \frac{d\mathbf{r}}{ds} \tag{4.5}$$

where $\mathbf{r}$ is the displacement vector of the ray from the optical axis, and s is taken to be along the path of the ray. And now this can be combined with the expression of s to give

$$\frac{d\mathbf{r}}{ds} = \frac{\nabla L(\mathbf{r})}{n} \tag{4.6}$$

In order to produce a differential equation that is solvable by a computer, it is useful to define an independent variable. For this,

$$d\tau \equiv \frac{ds}{n} \tag{4.7}$$

is defined, where n is the refractive index along ds. Which can be applied to the expression above to produce

$$\frac{d\mathbf{r}}{d\tau} = \nabla L(\mathbf{r}) \tag{4.8}$$

By differentiating (4.8) with respect to τ and substituting for $(\nabla L(\mathbf{r}))^2$ using the Eikonal equation (4.4) , it is arrived at

$$\frac{d^2\mathbf{r}}{d\tau^2} = \frac{1}{2}\nabla n^2 \tag{4.9}$$

Where r is a three dimensional vector and as such, the above expression can be written out as a set of three independent equations

$$\frac{d^2x}{d\tau^2} = \frac{1}{2}\frac{\delta}{\delta x}n(x)^2 \frac{d^2y}{d\tau^2} = \frac{1}{2}\frac{\delta}{\delta y}n(y)^2 \frac{d^2z}{d\tau^2} = \frac{1}{2}\frac{\delta}{\delta z}n(z)^2 \tag{4.10}$$

However, for radial GRIN lenses such as those used in this investigation, the refractive index does not change with position along the optic axis, therefore,

$$\frac{d^2z}{d\tau^2} = 0 \tag{4.11}$$

Integrating with respect to τ to give

$$\frac{dz}{d\tau} = C \tag{4.12}$$

Or, more usefully,

$$d\tau = \frac{dz}{C} \tag{4.13}$$

As well as the constant refractive index along the optic axis, the GRIN lenses are radially symmetric, giving

$$\frac{d^2x}{d\tau^2} = \frac{d^2y}{d\tau^2} \tag{4.14}$$

Substituting for $d\tau$ to give

$$\frac{d^2x}{dz^2} = \frac{1}{2C^2}\frac{\delta}{\delta x}n(x)^2 \tag{4.15}$$

The Eikonal equation relates the refractive index of the medium to a path along the ray's propagation which might not be parallel to the optic axis. However for our simulation we are concerned with tracing a path along the optic axis, and calculating the distance of the ray from the optic axis. This is exactly what equation 4.15 describes. However, before it can be used the constant C must be interpreted. By substituting equation 4.7 in to equation 4.13, we arrive at

$$C = n(x)\frac{dz}{ds} \tag{4.16}$$

Where the refractive index n, has now been replaced by $n(x)$, which is the refractive index at radial displacement x.

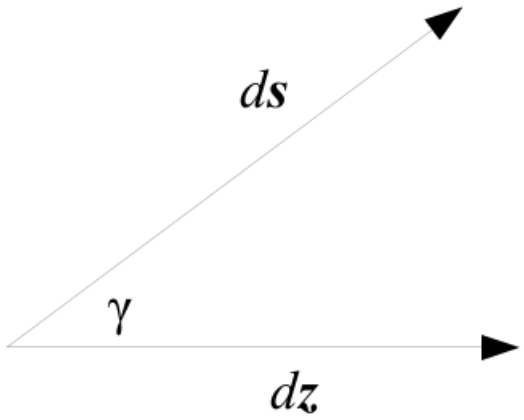

Figure 4.5: Diagram showing the relationship between ds, dz and and angle gamma

As shown diagrammatically in Figure 4.5, and by (4.16), C is the projection of the ray along the optic axis, and therefore:

$$C = n(x)\frac{dz}{ds} = n(c)cos\gamma \tag{4.17}$$

Where γ is the angle that the ray (at radial displacement x) makes with the optic axis. This gives the complete expression to be

$$\frac{d^2x}{dz^2} = \frac{1}{2n(x)^2cos^2\gamma}\frac{\delta}{\delta x}n(x)^2 \tag{4.18}$$

Or, to put it in a form that can be solved using the numerical Runge-Kutta method,

$$\frac{d^2}{dz^2} = D(x) \tag{4.19}$$

4.4.4 Computer simulation

In order to reproduce the ray's motion through the GRIN lens via an independent variable, a numerical technique is used. The equation for the position of the ray is modified such that its result depends on the previous location (this being a

tuple of the position and angle the ray makes with the optical axis). A program can then be written to step along the optic axis, iteratively calculating values for this two-dimensional parameter, and therefore problem has thus been diluted down to solving an ordinary differential equation.

As stated before, a common technique to be used in problems of this type is that of Runge Kutta integration, in which the next value is calculated from the previous and a mid point between the two. This has been refined to produce Runge Kutta version 4 (RK4), in which the computer uses the original point, and three in between points to calculate the next value.

The GRIN lens that shall be simulated will have a pitch of 0.29, a gradient constant of g=0.332, and a length of 5.45mm. This is identical to the Nippon Sheet Glass company (Melles Griot) lenses which were available to experimentally verify the findings of the computer simulation.

Setting up of expression

By defining a ray vector, T, as before,

$$\mathbf{T} \equiv \frac{d\mathbf{r}}{d\tau} \tag{4.20}$$

Since $\mathbf{T}$ is the same as before, its components are again the three optical cosines (Sharma et al., 1982):

$$\mathbf{T} \equiv \frac{d\mathbf{r}}{d\tau} = n\frac{d\mathbf{r}}{ds} = in\frac{dx}{ds} + jn\frac{dy}{ds} + kn\frac{dz}{ds} = in\cos\alpha + jn\cos\beta + kn\cos\gamma \tag{4.21}$$

Which in the one dimensional case reduces to

$$\mathbf{T} = kn\cos\gamma = \frac{d\mathbf{r}}{dz} \tag{4.22}$$

Or by substituting for dr with a numerical approximation

$$\Delta \mathbf{r} = R_{n+1} - R_n \tag{4.23}$$

Where R_n is the radial distance at step 'n', and by substituting for Δr with dr, through (4.22) in the limit $R_{n+1} - R_n \to 0$, the next radial distance can be calculated as

$$R_{n+1} = R_n + T_n dz \tag{4.24}$$

Thus, the ray can be propagated along by successively estimating T_{n+1}. The Runge Kutta numerical technique gives a method for doing this (Sharma et al., 1982):

$$R_{n+1} = R_n + \Delta z(T_n + \frac{1}{6}(A + 2B + C))T_{n+1} = T_n + \frac{1}{6}(A + 4B) \tag{4.25}$$

with,

$$A = \Delta D(R_n)B = \Delta z D(R_n + \frac{\delta z}{2}T_n + \frac{1}{8}\Delta z A)C = \Delta z D(R_n + \Delta z T_n + \frac{\Delta z}{2}B) \tag{4.26}$$

This is now a simple numeric problem for a computer to solve, using the initial conditions that R_0 is the distance of the ray from the optic axis, and T_0 is the original angle. $D(r)$ is evaluated using the expression given above, as is $n(r)$ in order to find the refractive index at that point.

In order to simulate the action of a GRIN lens placed a distance away from a single mode fibre, a series of ray propagations are calculated, numbered 1, 2 and 3 in Figure 4.6. Firstly, the ray is propagated from the single mode fibre to the GRIN lens. This is a simple case of using Pythagoras to calculate (from the NA of the fibre) the height in which the ray's extremity is on the GRIN lens.

The angle at which it enters the GRIN lens is calculated using Snell's law for a boundary between air and the refractive index at that height in the GRIN

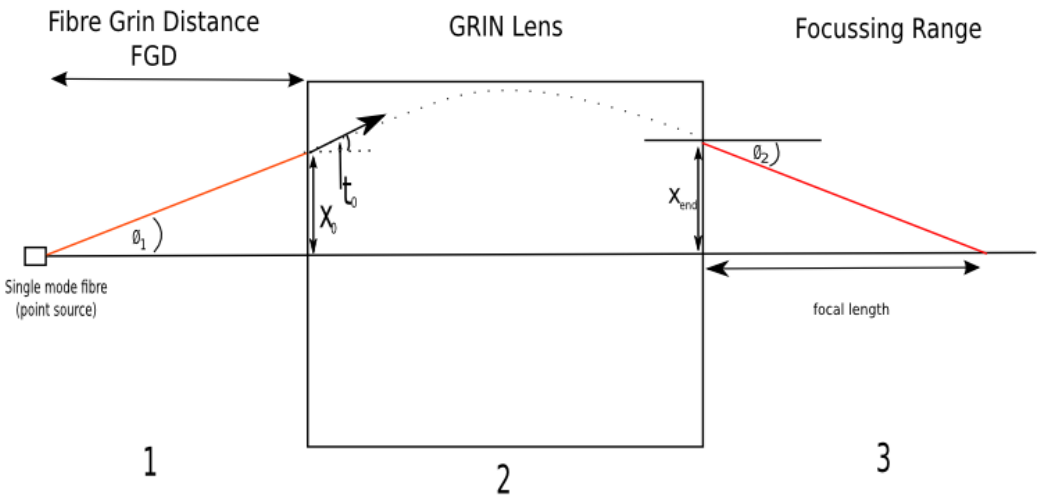

Figure 4.6: Simulation of single mode fibre through GRIN material

lens. The Runge Kutta method is then used to propagate the ray through the GRIN lens, incorporating values for the GRIN material's properties from the manufacturer's data-sheet.

At the end of the GRIN lens, Snell's law is then used to calculate the exit angle, before a final use of trigonometry to calculate the focal point position. The focus was chosen to be where the ray crosses the optic axis. In order to create a more complete image, several rays (5 in total) were propagated through the system.

This process was repeated over a range of values for the fibre-GRIN distance in order to characterise the effect of the fibre GRIN distance on the focal range, spatial resolution and confocality of the system. The effect of increasing the gradient constant, g, on resolution and focal length was also investigated.

4.5 Experimental characterisation of lenses

In order to verify the GRIN computer simulation, a tabletop FOCOM system was constructed as shown in Figure 4.7. Light from an 808nm laser source was coupled into a single mode optical fibre, making use of mirrors M1 and M2 for alignment and lens L1(x20 Nikon objective) for focusing the beam in to the fibre.

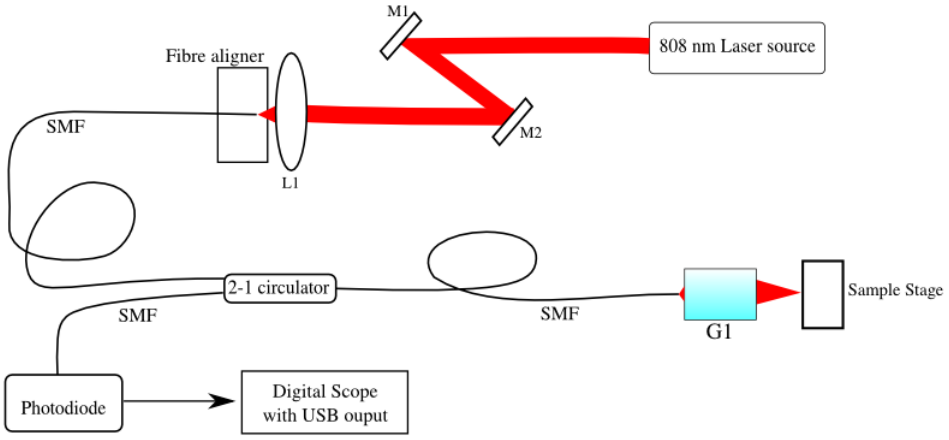

Figure 4.7: FOCOM system with GRIN lens objective

The objective lens of the FOCOM described in Chapter 3 was replaced with a 0.29 pitch GRIN lens (G1 in Figure 4.7). This lens was attached to the end of the single mode fibre by means of a custom made glass holder, as shown in Figure 4.8. The GRIN lens was glued (using a UV cure glue) to one end of the glass holder. The other end of the glass holder was designed in such a way that it could be fitted to the FC connector of the fibre with scope to adjust the fibre GRIN distance.

In order to investigate the effect of varying the fibre-GRIN distance, a mirror was axially scanned using a micrometer sample stage from the end face of the GRIN lens to a distance of 6 mm. The intensity from the reflected light through the FOCOM was recorded as a function of this distance for two separate fibre-GRIN distances.

A modified version of the tabletop system was created in order to characterise the aspheric lens, as shown in Figure 4.9, with a major change being the addition of a lock-in amplifier, the reasons for which will be discussed shortly. The light exiting from the single mode fibre is collimated by an aspheric lens (L2, NA=0.27) and passed through an optical chopper (637Hz) in order to increase the signal to noise ratio and to enable the discrimination of the required signal from back

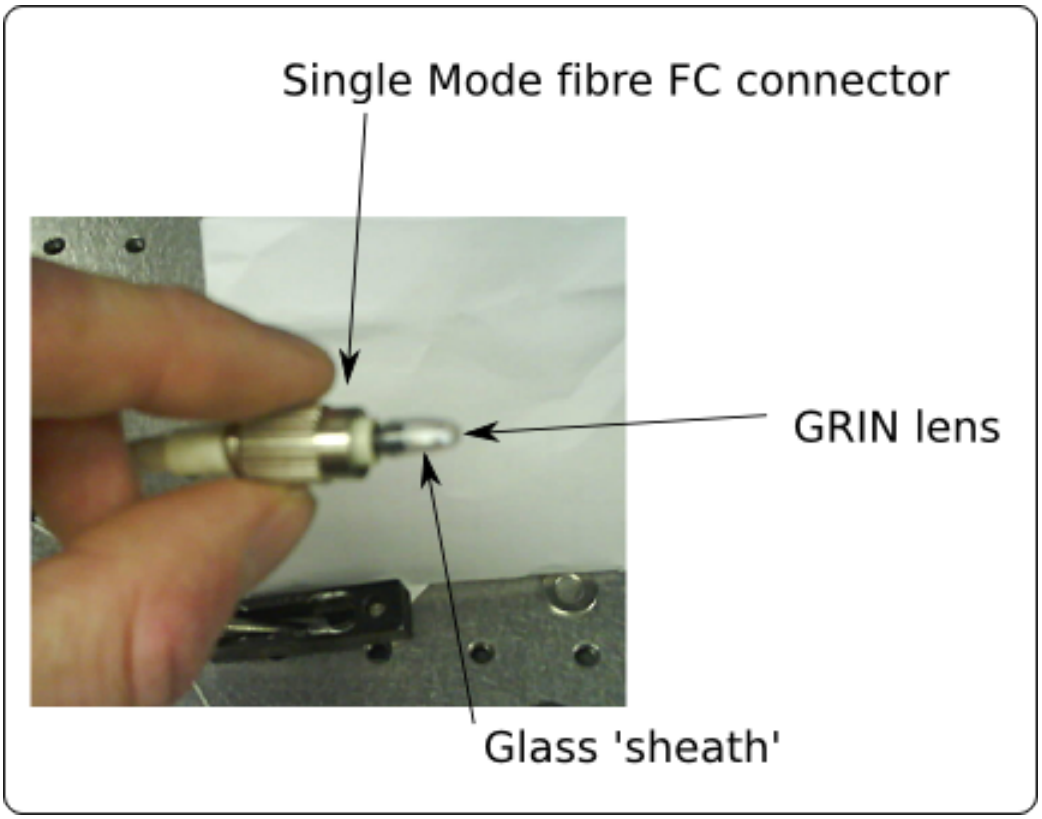

Figure 4.8: Glass holder for GRIN lens mounted on single mode fibre cladding.

reflections from the fibre.

The chopped light is then focused by an aspheric lens (L3, NA=0.55NA), acting as the objective, which is mounted on a motorised axial translation stage. A signal generator drives this stage using a sinusoidal voltage output, allowing the lens L3 to scan its focal point axially back and forth through a mirror typically at around 1.8 mms^{-1}. At this velocity, the lock-in amplifier is averaging the reflected signal over roughly 1.8μm (calculated from the integration constant of the lock-in amplifer) which equates to around 7 cycles of the chopper.

Light that returns from the focal point is then returned through the collimation optics L2 and delivered to a photodiode (Thorlabs, PDA 101). After signal processing through a lock-in amplifier (Femtolabs) the resulting signal is displayed on a digital oscilloscope (Tektronics) presenting the depth profile on its display, and permitting the storage of the data to a USB memory stick, in the

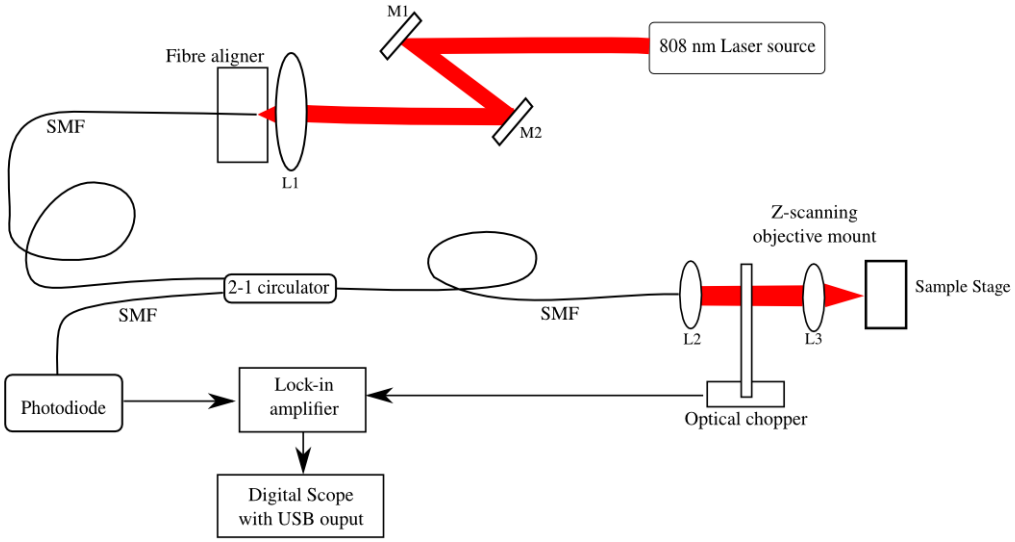

Figure 4.9: Desktop FOCOM system with aspheric lens.

comma separated value (CSV) text format, for transfer to a computer for analysis. Analysis was carried out using SCILAB on a Linux workstation running Ubuntu Intrepid Ibex. Graphical representation of the data was later produced using an OpenOffice.org Spreadsheet.

In order to demonstrate that the FOCOM system was also capable of measuring translucent objects, the mirror was replaced by a microscope cover glass slip (thickness 160 microns) and FOCOM scans were recorded as with the mirror.

4.5.1 Results

Figure 4.10 shows the computer simulated ray trace of a ray through a piece of commercial GRIN material (Nipon-Sheet Glass company, g=0.327,L=5.57mm). A total of 10 rays (five rays, including an on-axis ray, were simulated and the diagram uses symmetry to complete the image) are shown propagating through free space from a single mode fibre, through the GRIN media and then propagating through free space to a focus point, determined to be 1.5mm from the output face of the GRIN lens. The relationship between the focal length, axial resolution and spot size with the spacing between the fibre and the GRIN lens is shown in

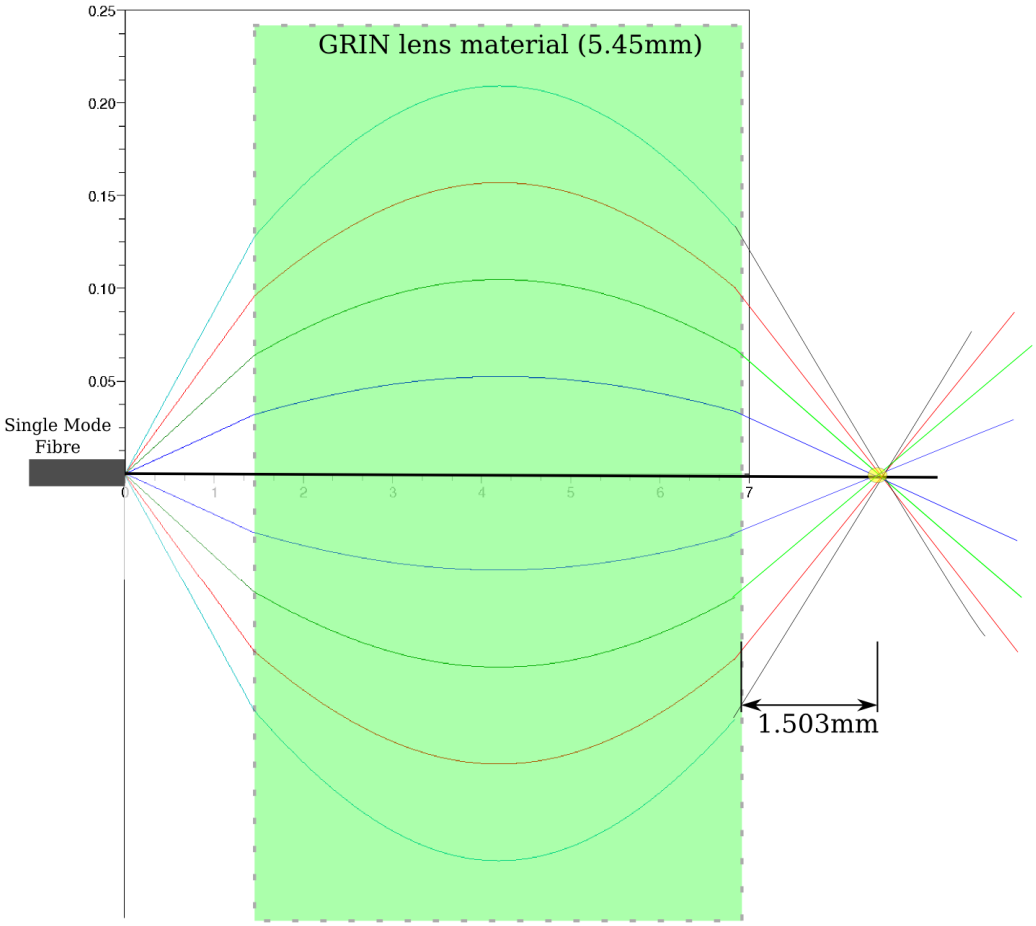

Figure 4.10: Simulated ray path of light through GRIN media

Figure 4.11.

Axial resolution is estimated from the computer systems by way of a 'focal spread parameter'. This is taken as the difference in the position that the outer most and inner most ray crosses the optical axis. From this point on, axial resolution will be refered to as focal spread where the computer simulation is concerned.

Figure 4.12 shows the results of increasing the gradient index constant, g, on focal length and focal spread. As a convenient method of measuring the usefulness of these values, a plot of the ratio of focal length to focal spread is also given. A good imaging system will have a low ratio of focal spread to focal length, meaning that many more unique data points can be recorded through the focal length.

Figure 4.13 shows the effect of increasing the gradient constant g on the 'pitch' of the lens. A higher value of g means that the ray has a shorter periodicity of motion as it propagates through the GRIN media, and therefore in order to exit at the correct height and angle for optimal focussing, the material must be shortened.

The experimental results of the relationship between the focal length and focal spread is shown in Figure 4.14 where each curve is a separate measurement from scanning a mirror through the focal point of the lens. The narrow continuous blue trace shows the reflection peak when the GRIN lens is positioned 750 $\hat{\text{I}}\frac{1}{4}$m from the fibre, and the dashed line shows that of a butt-coupled fibre (FGD=0 μm). The butt-coupled trace exhibits an asymmetric appearance due to the travel on the micro-stage not being sufficient to record the full spread of the response.

A scan of a mirror recorded using an aspheric lens as an objective is shown in Figure 4.15a, and that of a microscope cover slip is shown in Figure 4.15b. Figure 4.15a exhibits a single peak due to the front face of the mirror only,whereas figure 4.15 shows a dual peak due to the front and rear face of the cover slip. The small 'ripples' in the leading peaks are manifestations of the axial airy disc pattern

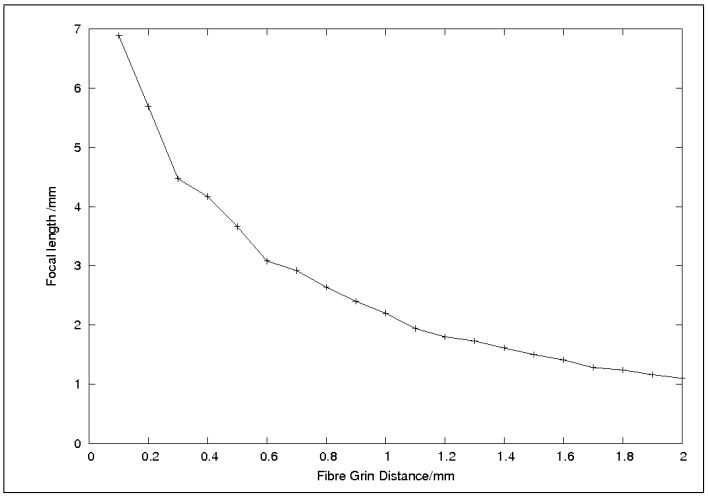

(a) Focal Length versus fibre grin distance

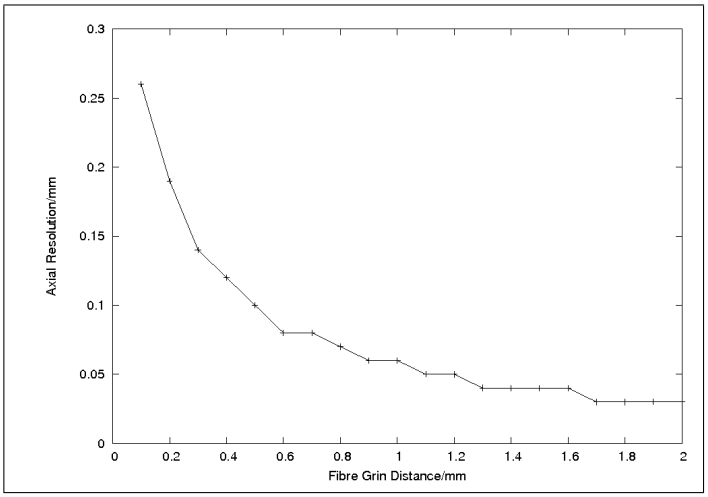

(b) Axial resolution versus fibre grin distance

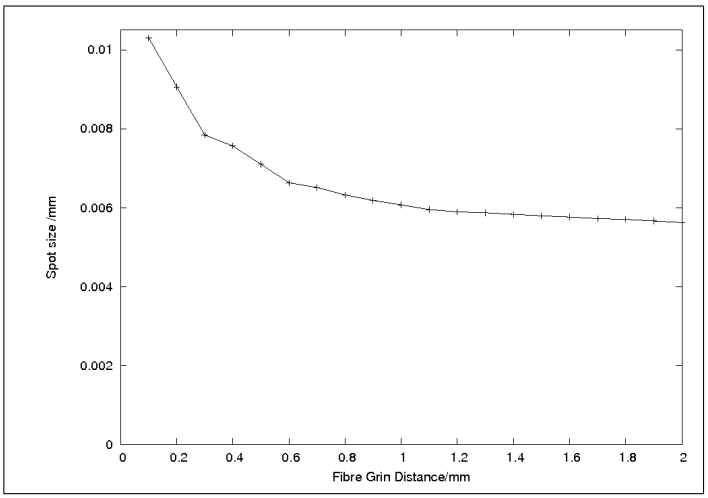

(c) Spot size (FWHM) versus fibre grin distance

Figure 4.11: Simulated parameters of GRIN lens with varying distance between fibre and GRIN lens.

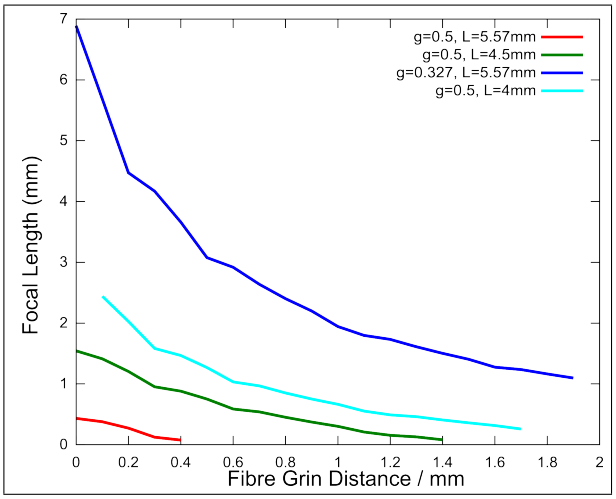

(a) Focal Length versus fibre grin distance

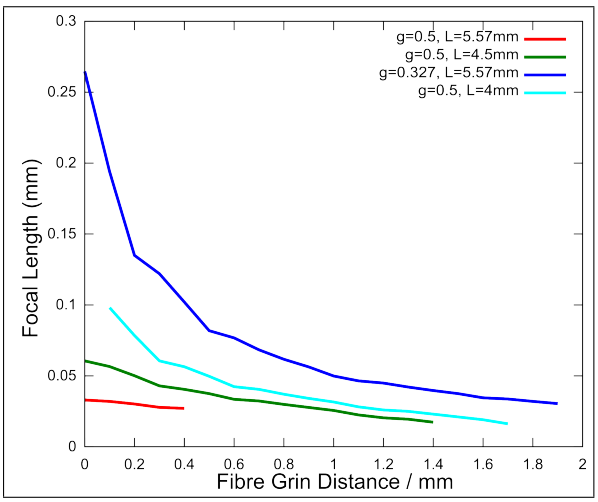

(b) focal spread versus fibre grin distance

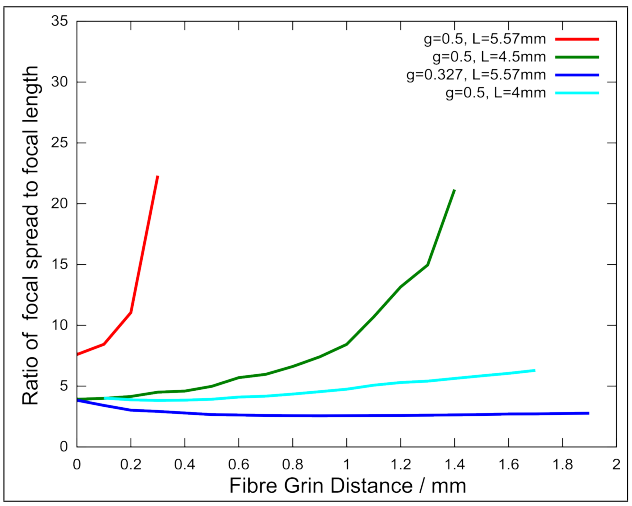

(c) Spot size (FWHM) versus fibre grin distance

Figure 4.12: Simulated effect on parameters of GRIN lens with varying radial profile.

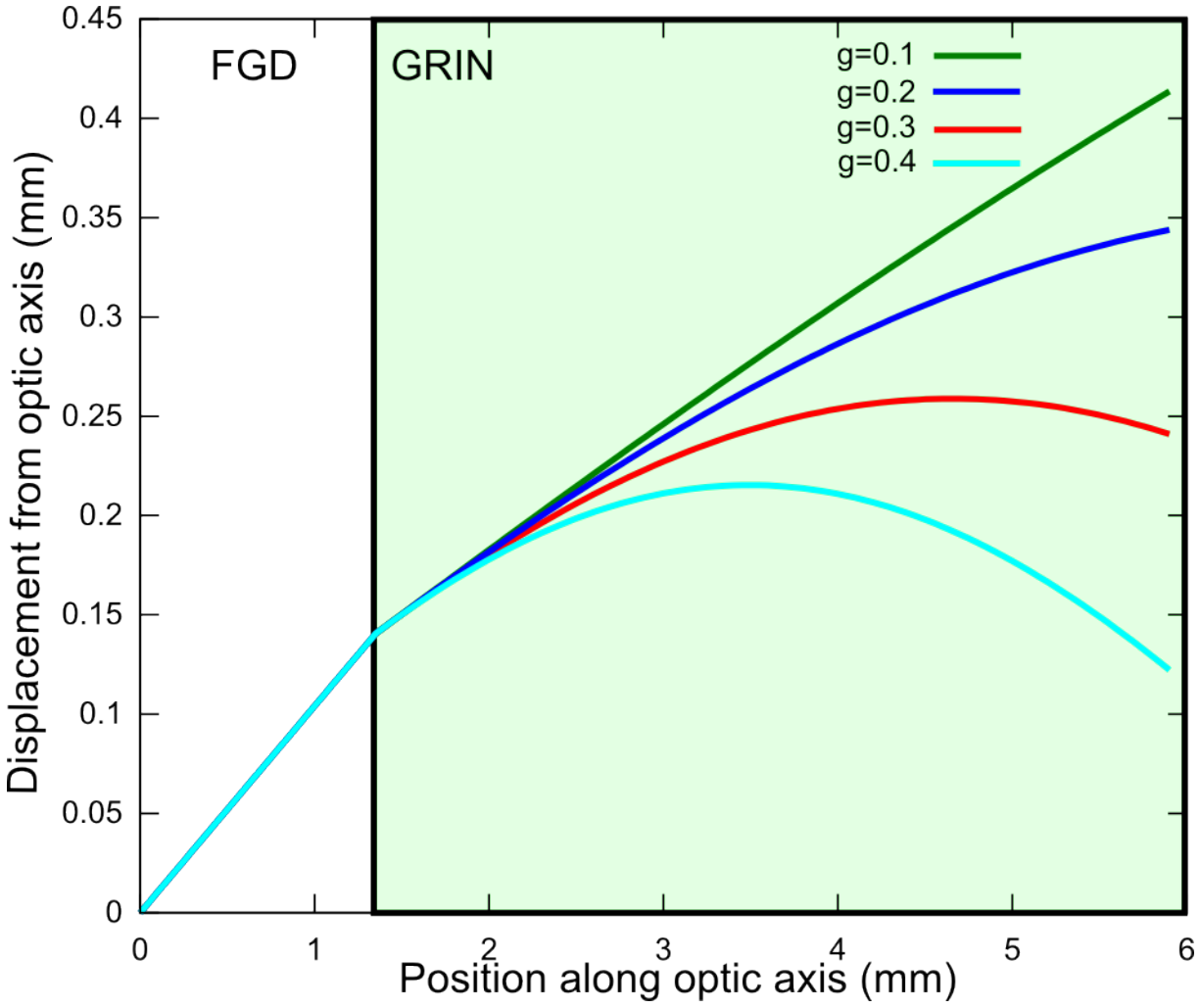

Figure 4.13: Effect of varying g on ray path through GRIN lens

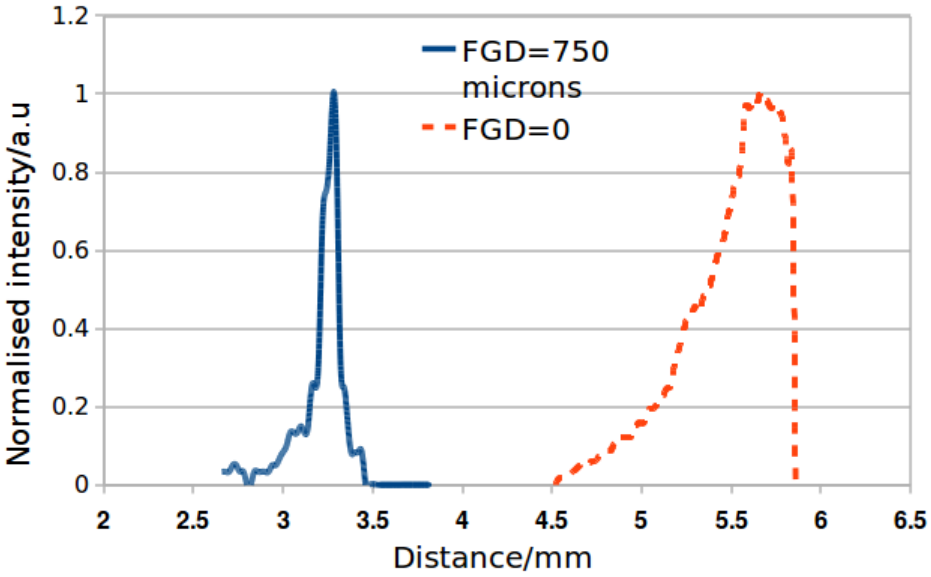

Figure 4.14: Experimental results of testing the GRIN lens.

formed in a diffraction limited system. Their appearance is due to spherical abberations and the alignment of the end face of the fibre with respect to the imaging objective (Sheppard C.J.R, 1997).

In order to make a proper comparison between the two types of lenses, the characteristics are shown in Table 4.1. The properties that are the most adequate for the dental application are in bold text for clarity.

Lens	**Est. Axial Res'ln**	**Axial Resolution**	**Focal Length**	**Diameter**
GRIN, FGD=0mm	>300 μm	>1mm	5.5mm	1.8mm
GRIN, FGD=0.75mm	75μm	100μm	3.2mm	1.8mm
Aspheric	60.8 μm	33.1μm	2.9mm	3.2mm

Table 4.1: Table of estimated and measured parameters for a GRIN lens and aspheric lens confocal microscope

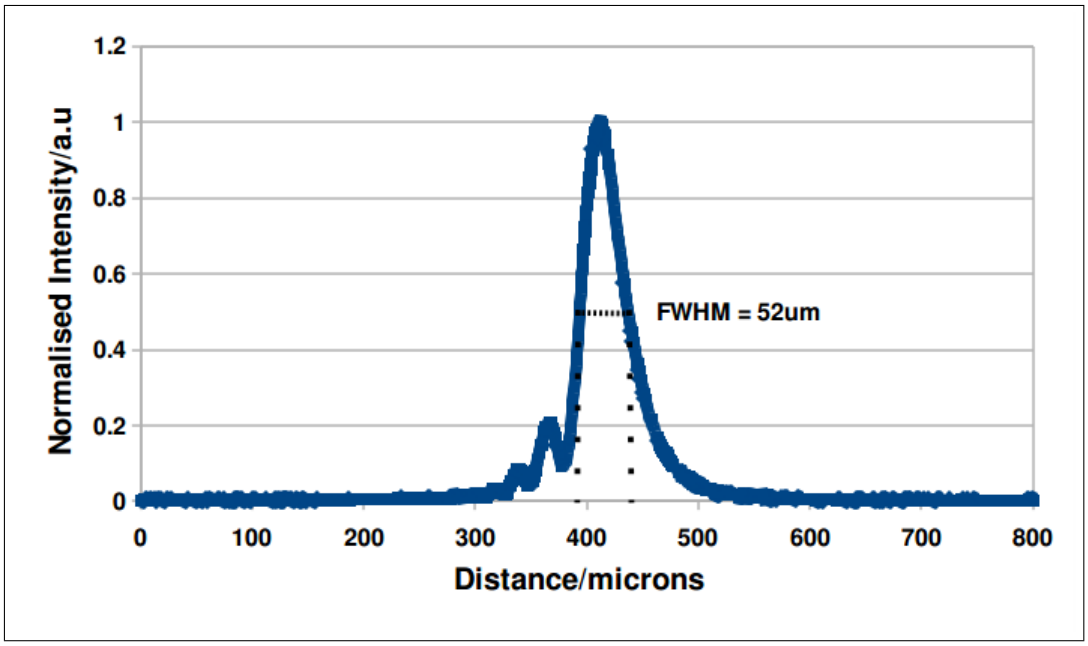

(a) Axial scan of a mirror

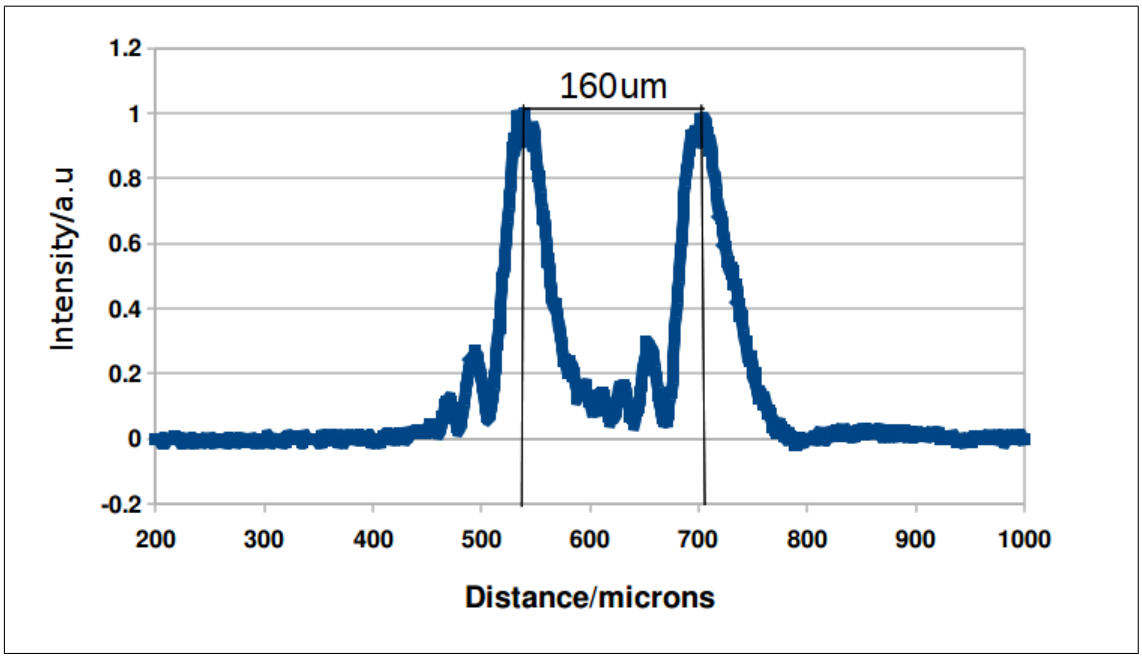

(b) Axial scan of 160um microscope coverslip

Figure 4.15: Experimental characterisation of aspheric lenses.

4.6 Discussion

As shown in Figure 4.10, the rays leave the single mode fibre and propagate a distance through free space to the GRIN lens. As expected, while propagating through the GRIN material, the rays follow a curved path. At the other end of the lens material, the rays are refracted again and propagate through free space producing a focal point, 1.503mm from the GRIN lens. It should be noted, the similarity between the output of this simulation and the theoretical ray paths displayed in Figure 4.4.

It should also be noted that in 4.10, the material shown is only a small fragment of the GRIN lens used. The diameter of the GRIN lenses used for the practical study is 1.8mm, and shown is a diameter of around 0.5mm. This extra material has been omitted for image scaling purposes. From the ray diagram it is possible to say that a smaller diameter GRIN lens could be utilised for this study if such a lens was possible since only a thin tube of the existing GRIN lens is actually used for lensing.

The use of only a thin area of the GRIN lens has implications in the effective NA of the system. If the fibre was more highly divergent, then more of the material would be used for focussing and this would result in a higher effective NA of the system, and therefore a higher resolution. However, the NA of the fibre is linked to the intrinsic properties of the single mode fibre, and replacing the fibre with another one would have implications in the confocality of the system and choice of wavelength.

The effect of increasing the fibre GRIN distance on the focal length (and the resulting spread of this point) is shown in Figure 4.11a. The data sheet that the GRIN lens manufacturer provides shows a similar graph for focal length, and this matches up with that presented in Figure 4.11a, verifying the computer model. Both of the graphs presented in Figure 11 show an almost exponentiation decrease with a slight bump around 0.4mm. It is thought that this is due to

the accuracy of the integration routines being greater than the bit depth of the computer running the simulation (Sharma et al., 1982).

It has been demonstrated that as the distance becomes longer (for example in order to give the light exiting the fibre more distance to diverge and backfill more of the lens), the focal length becomes shorter (Figure 4.11a) and more tightly focussed (Figure 4.11b). This has implications in the proposed use of a GRIN lens for investigating dental disease. A long focal point is useful as that increases the depth that can be scanned in a fibre optic confocal microscope setup, however, as seen in the graphs this means a less tightly focussed spot. This reduces the resolution of the scan that is possible with a useful focal lenght.

4.11c presents the effect of increasing the fibre grin distance on the spot size of the GRIN lens. This is included for completeness as the application that this thesis concerns itself with is of depthprofiles rather than imaging. From the graph in 4.11c one can see that the spot size reduces with increasing FGD to a steady state value of around 7μm. This gives high localisation to a measurement on the tooth surface and would be suitable for measuring a lesion that presented itself at around 20μm diameter.

The experimental verification of the GRIN lens simulation backs up these relationships, with a butt-coupled fibre producing a poor resolution with a long focal length, and a longer fibre-GRIN spacing producing a higher resolution but with a shorter focal length. This shorter focal length would not be a problem if the resolution was higher. However, with a resolution of 100 $\hat{\text{I}}\frac{1}{4}$m, one could only record 20 useful data points through a 2 mm focal length.

It is noticeable from the graphs in Figure 4.11 that the resolution of a GRIN lens system is less than 50 microns with a fibre GRIN distance of over 1 mm, and that the focal length also changes between a fibre GRIN distance of 1 and 2 mm. If the fibre was to be scanned axially to, and from, the GRIN lens face, this could provide a method of scanning the objective focal spot with a stationary objective.

However, the resolution provided would still be poor compared to the distance that is being scanned, and once biological samples are considered aberrations would make this technique difficult.

As can be seen from Figure 4.12 if one was to obtain a GRIN lens with a higher gradient index constant of 0.5 (and shorter length of 4mm), a resolution of less than 50μm can be obtained with a focal length of around a millimeter. However, the commercially available GRIN lens provides the best ratio of focal length to focal spread for a given range of focal lengths.

As an estimate from the simulation, a fibre GRIN distance of 1.1 mm will provide a focal point of around 2 mm with a resolution of around 50 μm. Using bulk optics, a resolution down to a couple of microns is achievable. A reduction in resolution by the GRIN lens is expected due to the lower NA values (0.54) for the lenses than in the bulk objectives.

The axial full width half maximum of the mirror scan with an aspheric lens, as shown in Figure 4.15a, was found to be 52($\pm$0.08)μm. This is calibrated from the cover-slip scan which provides a reference thickness measurement. The value is then corrected for the bending of the optical cone as it propagates through a boundary between refractive indices. Such a boundary causes a focal shift that increases or decreases depending on the relative refractive indices.

This is higher in resolution to the theoretical axial resolution of a lens. The theoretical axial resolution was calculated with an NA_{eff} of 0.13 (due to the fibre-dominated system) which gave a calculated value of 60.8μm. This value arises from the spread of the light as it exits the SMF and is collected by the collimating optics. An NA value of 0.13 was given for the SMF, from this it is calculated that the diameter of the collimated beam is only 0.38 mm, giving the reduced effective NA of the objective. Experimentally, it has been found that the system has a slightly higher resolution than calculated, and this could be down to the collimator producing a slightly wider beam diameter, resulting in a slightly

higher effective NA.

This system only incorporates singlet aspheric lenses, and it could be envisaged that a specially designed doublet could be used to widen the beam before the objective lens. This would increase the effective NA and allow for higher resolutions up to the diffraction limit, which keeping the form-factor of the lens system to a minimum.

One of the major advantages to using the aspheric lenses is the ability to incorporate an optical chopper into the system. This allows a lock-in amplifier to be used which can increase the signal to noise ratio when investigating biological samples. While an optical chopper could have been implemented with the GRIN lens system, the blades of which would have to be incredibly small to be placed between the lens and the sample. This would have been possible with a MEMS device, but unfortunately this was not available in the scope of this work.

4.7 Conclusions

While GRIN lenses provide a confocal axial scanning ability, and their dimensions are very suitable for use in the oral cavity, the resolutions provided are too low to be useful for the early detection of dental disease where an early lesion may be around 10μm in thickness.

Aspheric lenses theoretically allow a higher resolution with a similar focal length and also the incorporation of an optical chopper. However, it has been shown in this chapter that without a more complex arrangement of lenses, allowing for beam widening, resolutions that are obtainable at this wavelength are similar to the GRIN lens system.

In this chapter, it has been shown that it is possible to use miniature GRIN or aspheric optics to produce a fibre optic confocal microscope similar to that of (Rousseau et al., 2007). However, the resolution obtainable with this miniature

system has to be shown to be lower. This means that the data that is collected with the miniature system is intrinsically poorer than that of the previous work, and the interpretation of recorded scans much more difficult.

The next chapter introduces a method of analysing one dimensional data called principal component analysis. This technique will be applied in the subsequent chapter where the miniature aspheric FOCOM system is used to diagnose dental caries.

The aspheric route has been chosen due to the incorporation of the lock-in amplifier allowing for better signal to noise ratios, and also for the hypothetical diffraction limited improvements that could be developed. It is expected that the results from using an aspheric lens setup would be applicable for a similar GRIN based setup due to the similar resolution characteristics found in this chapter.

Bibliography

T. Dabbs and M. Glass. Fiber-optic confocal microscope: FOCON. *Appl. Opt*, 31(16):3030–3035, 1992.

D A Landis and C J Seliskar. Fiber-Optic/GRIN lens couples for use in chemical spectroscopy. *Applied Spectroscopy*, 49(5):547–555, May 1995. URL `http://as.osa.org/abstract.cfm?URI=as-49-5-547`.

Erich W. Marchand. Gradient-index imaging optics today. *Applied Optics*, 21 (6):983, March 1982. doi: 10.1364/AO.21.000983. URL `http://ao.osa.org/abstract.cfm?URI=ao-21-6-983`.

C. Rousseau, S. Poland, J. M. Girkin, A. F. Hall, and C. J. Whitters. Development of Fibre-Optic confocal microscopy for detection and diagnosis of dental caries. *Caries Research*, 41(4):245, 2007.

A. Sharma, D. V. Kumar, and A. K. Ghatak. Tracing rays through graded-index media: a new method. *Appl. Opt*, 21(6):984Â987, 1982.

Shotton D.M Sheppard C.J.R. *Confocal laser scanning microscopy*. Bios Scientific Publishers, 1997.

Chapter 5

Principal Component Analysis

5.1 Introduction

For a diagnostic tool to be successful, there must be a reduced emphasis on the user to interpret the recorded data and an increase on providing clinically useful quantified data. This is because in simple diagnostic tools there may be a binary set of relations in which a computer can test for a number of conditions and provide an answer using logic. However, in biological situations, the problem is much more complex where the data is not as clear cut, quantised and frequently not logical.

It is important to consider that the end user of a medical device is more than likely a non-expert in the technology, and therefore, will not have the familiarity with the raw output data that someone who developed the device would. There is therefore an interest in a method to allow a computer to interpret data at a deeper, more statistical, level and provide the user with clear information suitable to aid diagnosis.

This chapter introduces principal component analysis (PCA) as a way of aiding the analysis of one dimensional data sets (Joliffe and Morgan, 1992). This has relevance for this work because it allows a computer to be used to aid with the interpretation of the data. Another motivation for using PCA is the reduced resolution in the optical system when using miniature lenses as opposed to bulk optics, however, such an analysis system would also be used with systems that have the highest resolutions possible.

5.2 Principal components

In order to understand what PCA is it is useful to compare it to Fourier analysis where a data set is decomposed into a series of sine and cosine components. A complex wave form can thus be represented to some level of accuracy by a much smaller number of coefficients. The original wave form can then be recon-

Figure 5.1: Decomposition of two shapes (a and b) into multiples of stars, circles and squares.

structed through the addition of the original base components, multiplied by the coefficients.

PCA achieves a very similar result, except the principal components in this technique are not trigonometric functions. Rather they are derived from the similarities in the data and differ between data sets. The original data can then be interpreted by considering the coefficient (or weighting) of each component in order to attach meaning and relationships to the original data set. By using these components, the interpretation of the original data can be a much simpler task.

This is shown diagrammatically in Figure 5.1 where there are two outlines of complex shapes. If one was to try and describe the shapes, say over the telephone, it would be very difficult. However, if one notices that both shapes are a superposition of a star, a square and a circle the task is much simpler. These three shapes can be said to be the "Principal Components of the shapes" in Figure 5.1a and b.

Figure 5.1a is a shape that is composed of all three base components of the same size, whereas 5.1b is only composed of a circle and a star that has been enlarged by 50%. Therefore, if one knows the forms of the components (star,

circle, and square), one can represent each shape as a simple three component vector, i.e. this vector would be (1,1,1) for Figure 5.1a, and (1.5,1,0) for Figure 5.1b. In order to group objects that are similar, one can then plot these vectors in a three-dimensional scatter plot. Due to the nature of the vectors, similar objects will lie close together in such a representation. Of course, as shall be seen later, more complex objects will require more than three dimensions and a new way of interpreting the data will be required.

For most experimental datasets, the principal components are unknown and therefore a method for finding these is needed. This is exactly what PCA provides by way of a covariance matrix. The next section describes the mathematics of PCA and how the base components are found.

5.2.1 Mathematics

In linear algebra, for a matrix $\mathbf{X}$, there exists a non zero eigenvalue, λ, such that $X\mathbf{z} = \lambda z$, where $\mathbf{z}$ is a non-zero vector known as an eigenvector of $\mathbf{X}$. A simpler way of explaining this is that there is a vector $\mathbf{z}$, that when pre-multiplied by a matrix $\mathbf{X}$, the mathematical effect is to scale z by λ, the eigenvalue. The operation of scaling does not change the direction of the vector $\mathbf{z}$, only its magnitude.

For a square matrix of size N by N, there will be up to N discrete and non-trivial eigenvalues and eigenvectors. Therefore the definition of the eigenvalue should be written:

$$\mathbf{X}z_i = \lambda_i z_i \tag{5.1}$$

In this equation there are i orthogonal eigenvectors, z_i, each with a corresponding eigenvalue λ_i. In order to calculate the eigenvalues of $\mathbf{X}$, an equation known as the characteristic polynomial is solved. The determinant of a matrix is a scalar and is a characteristic property of a square matrix, denoted $det(X)$. The characteristic polynomial equation is stated to be $det(\lambda\mathbf{I} - \mathbf{X})$, which is of

the order of N. The eigenvalues, λ_i, are found at the roots of this equation:

$$det(\lambda \mathbf{I} - \mathbf{X}) = 0 \tag{5.2}$$

It was stated before that the only result out of multiplying the vector $\mathbf{z}_i$, by $\mathbf{X}$ is to multiply $\mathbf{z}_i$ by a scalar. Therefore the set containing the vectors, $\mathbf{z}_i$, is a vector space.

Furthermore, if the matrix is symmetric, then the eigenvectors are real and provide a basis for the column data contained in the original matrix. This is contained in the theory of eigen-decomposition, whereby a real, symmetric matrix, $\mathbf{X}$, can be represented as $\mathbf{X} = \mathbf{Q}\Lambda\mathbf{Q}^T$, with $\mathbf{Q}$ being a matrix where each column is an eigenvector of $\mathbf{X}$. The matrix Λ is diagonal, with each entry being an eigenvalue of $\mathbf{X}$, for example

$$\begin{bmatrix} \lambda_1 & 0 & 0 \\ 0 & \lambda_2 & 0 \\ 0 & 0 & \lambda_3 \end{bmatrix} \tag{5.3}$$

This means that if one has a set of data that can be contained in a symmetric matrix, the principal components of the data should be able to be calculated. Up to this point, the discussion has been particularly abstract and so attention will now be turned towards using a real data set.

5.2.2 Principal components of real data

In order to keep this chapter relevant to the rest of this thesis, this section will deal with calculating the principal components of data that comprises a set of one dimensional 'scans'. This is in keeping with the previous chapter's discussion into fibre optic confocal microscopy and the data recorded with such a system, and also with the work involving ultrasound latterly in this thesis.

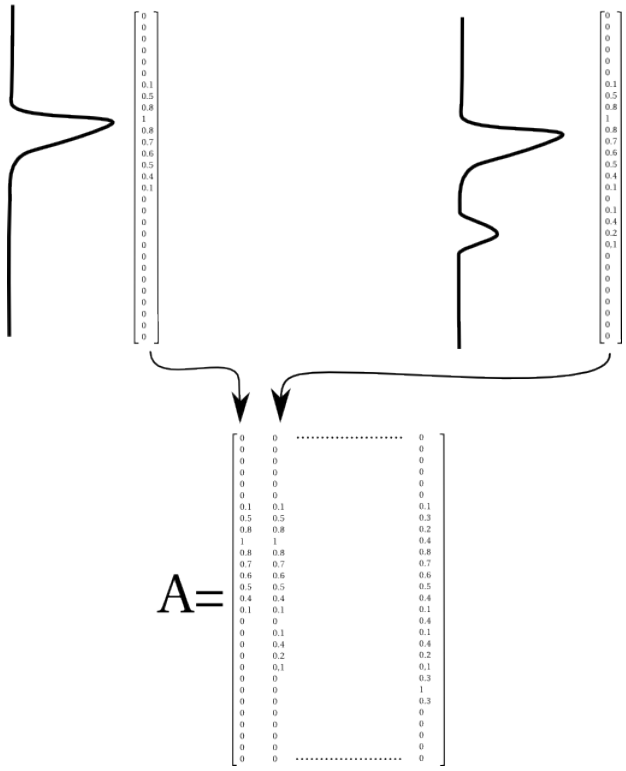

Figure 5.2: Formation of data matrix, A, from one dimensional FOCOM data

Figure 5.2 shows how a matrix can be built up from a number of one dimensional data-sets. Each column of **A**, is one set of, say N, voltage measurements over a period of time, with M being the total number of scans in the matrix **A**. Thus, the final matrix **A** is an M by N matrix, and typically N»M.

However, the matrix **A** is not square since typically N»M, and there is no guarantee that it will be symmetric. Therefore, in order to make use of eigenvalues and eigenvectors for principal component analysis of this data set, a further treatment of the data is required. The aim is to produce a real symmetric square matrix, containing information about the data in **A**. In order to achieve this, a covariance matrix, **C**, is calculated for the matrix **A**.

5.2.3 Covariance Matrix

In order to introduce the concept of the covariance matrix, it is useful to create a new notation for the matrix **A**, so that $\mathbf{A} = [\phi_1 \phi_2 \dots \phi_3]$, where ϕ_i is the i^{th} set

of N measurements, x:

$$\begin{bmatrix} x_1 \\ x_2 \\ \dots \\ x_N \end{bmatrix} \tag{5.4}$$

The covariance matrix, $\mathbf{C}$, is a matrix whose entries are calculated from the covariance between each of the columns in $\mathbf{A}$ with each other, such that the $(i,j)^{th}$ entry of $\mathbf{C}$ is:

$$C_{ij} = (\phi_i - \bar{\phi}) \times (\phi_j - \bar{\phi}) \tag{5.5}$$

In this expression, $\bar{\phi}$ is the average set of measurements in $\mathbf{A}$. In order to simplify this discussion, we can introduce the mean shifted matrix $\mathbf{B}$ such that

$$\mathbf{B} = [\phi_1 - \bar{\phi}\phi_2 - \bar{\phi} \dots \phi_3 - \bar{\phi}] \tag{5.6}$$

The covariance matrix, $\mathbf{C}$, can now be calculated as $\mathbf{C} = \mathbf{B}\mathbf{B}^T$, where $\mathbf{B}^T$ is the transpose of matrix $\mathbf{B}$. The covariance matrix has the two required properties of symmetry and being square by definition and therefore it is possible to calculate the eigenvectors of $\mathbf{C}$. These eigenvectors are, as stated before, a vector space relating to the data in $\mathbf{A}$. The data in $\mathbf{A}$ can thus be projected to this new space and represented as a linear combination of the new basis vectors.

The next section shall explain an efficiency problem with calculating the eigenvectors of $\mathbf{C}$, and subsequently show the final steps in calculating the principal components.

5.2.4 Computing eigenvectors and eigenvalues of C

Most mathematical software packages have the ability to compute the eigenvalues and eigenvectors of a given matrix, with the amount of processing power required dependent on the matrix in question. The calculation of eigenvectors

and eigenvalues is an iterative process across the matrix, with the characteristic polynomial (5.2) solved.

The covariance matrix of a matrix $\mathbf{B}$ can be also defined as

$$\mathbf{C} = \mathbf{B}\mathbf{B}^T \tag{5.7}$$

This matrix, $\mathbf{C}$, is of size N by N, and therefore there will be up to N discrete and non-trivial eigenvectors (i.e. N roots of equation 5.2). If we assume that the number of measurements recorded in each column of $\mathbf{B}$ (the mean shifted values of $\mathbf{A}$) is to be very large, the time to calculate the eigenvalues and eigenvectors will also be very large.

In order to reduce this time and make the process more efficient, consider the matrix $\mathbf{B}^T\mathbf{B}$ and it's eigenvalues, and eigenvectors $\mathbf{v_i}$, such that:

$$(\mathbf{B}^T\mathbf{B})\mathbf{v}_i = n_i\mathbf{v}_i \tag{5.8}$$

The matrix $\mathbf{B}^T\mathbf{B}$ is only M by M in size, which by assumption is much smaller than N by N, and therefore much quicker to compute. However, in order to relate this back to the eigenvalues of $\mathbf{C}$, consider the pre-multiplication of both sides by $\mathbf{B}$:

$$\mathbf{B}\mathbf{B}^T\mathbf{B}\mathbf{v}_i = n_i\mathbf{B}\mathbf{v}_i \tag{5.9}$$

Which by definition of $\mathbf{C}$ (5.7),

The result being that the eigenvalues, n, of $\mathbf{B}^T\mathbf{B}$ are equal to those of $\mathbf{C}$, λ, and the eigenvectors of $\mathbf{C}$, $\mathbf{u}_i$ can be found by $\mathbf{u}_i = \mathbf{B}\mathbf{v}_i$. This last calculation is a simple task for any matrix based mathematical computer program or function library.

5.2.5 Making sense of the new set of axes

The final calculation in the last section produces a set of eigenvectors of **C** by multiplying a set of vectors to the mean shifted data. It is these resulting vectors that are the Principal Components of the data in **B**. Each principal component is a column matrix of length N, and if plotted may look like a member of **B** (the mean shifted version of **A**). Therefore it is possible to represent a member of **A** as a set of weightings, **w** of each of the base vectors, **u**.

$$\mathbf{\Gamma} = [w_1, w_2, \ldots, w_M] \tag{5.10}$$

This is known as projecting a member of **A** on to the new set, with Γ_i the representation of ϕ_i in terms of these projection weights. This is easily done in mathematical software by pre-multiplying the members of **B** with the transposed set of principal components, $\mathbf{\Gamma}_i = (\phi_i - \bar{\phi})\mathbf{U}^T$, where **U** is a matrix made up of the principal components, with each column being a separate principal component.

Furthermore it is possible to reconstruct a member of **A** from the weightings with simple mathematical operations.

$$\phi_i = (\sum_{j=1}^{M} w_j u_j + \bar{\phi}) \tag{5.11}$$

It has been stated that for a square matrix of dimension M, there will be M different eigenvalues and eigenvectors, which means that for the new vector space that has been derived there may be up to M different dimensions in this space. It is therefore important to try and reduce the number of dimensions as much as possible in order to analyse the data easily.

5.2.6 Recap

After all the mathematics in the previous section it is a good idea to work out a simple method as to how one may apply PCA to a set of measurements for analysis. Before starting the PCA process, the data should be aligned to a common point. This is in order that each row of the matrix **A** corresponds to the same measurement across each of the scans in **A**. As an example, consider the depth profiles recorded using a FOCOM or ultrasound system. A set of scans could be aligned so that the 'front' face of the material being scanned occurs at the same point, say the tenth sample. In the matrix **A**, each member of the tenth row is now a separate measurement of the same location through the material. After this has been achieved, the mean set of measurements is subtracted from the data set. The effect of this is to ensure the data set has a zero empirical mean and allow for proper comparison with a minimised error due to approximating the data.

The eigenvectors and eigenvalues of the covariance are now calculated using the more efficient method described above. The eigenvectors are multiplied to the mean shifted data set to reveal the principal components, and finally each column of the mean shifted data set is multiplied to the principal component matrix to produce a vector of the weights of each component in that column.

For analysis, the weights are used to measure distances between scans and therefore their similarities. The coefficients contained in the weight vector can also be plotted as a scatter plot in order to visualise clustering along certain principal components. It is this latter technique that will be used in the following chapters regarding dental disease detection.

5.3 Applications of PCA

The applications of PCA are widespread and multidisciplinary, and as such, a review of the field would be well outside the scope of this chapter. For a complete description of PCA and its applications, the book by Jolliffe (1986) is a popular reference source.

Since PCA is just a multi-variate statistical technique, the source of the data is not of any interest in using the technique. The basic idea of PCA is to take a set of data with a large number of variables, and reduce these variables to a number that is easier to interpret.

The ability of principal component analysis to represent a data set in terms of a much smaller dimension vector of weights (along with the known components) allows the technique to be used for image compression (Costa and Fiori, 2001; Dony and Haykin, 1995). This is a lossy compression technique, but with the appropriate number of principal components chosen, the effect can be worthwhile.

The application of principal component that created interest in the technique for dental diagnosis was that of face recognition (Turk and Pentland, 1991). This work by Turk and Pentland (1991) is heavily cited, perhaps due to the clarity of the explanation of the PCA process which allows for the transfer of their ideas across to other fields and disciplines.

For face recognition, a set of known faces are used to create the principal components, known as a set of 'eigenfaces'. These eigenfaces occupy a vector space known as facespace (Turk and Pentland, 1991). A new face can be projected in to this space, and using a distance measurement the technique can accurately decide which person the new image belongs to.

If it is found that the new face is not close to any of the known faces, but still with in a useful distance to the facespace, it is said to be an unknown face that can be added to the model. If the new face lies completely outside the facespace, then it is said to not be an image of a face. This technique is also useful for

face recognition inside a larger image, perhaps for motion tracking or security surveillance(Turk and Pentland, 1991).

It is not a complicated matter to use PCA with two-dimensional data such as images (say, of size N by M) because the method requires that the image is transformed into a one-dimensional data set. This is achieved by concatenating each row of pixels to produce a long one dimensional data set of size 1 by NxM(Turk and Pentland, 1991). This means that almost any modality of collecting data can be used as a source for PCA so long as proper alignment of the data has taken place. In the case of matching a face to a specific known face, this is usually performed so that the eyes, nose and mouth are in roughly the same position in each image.

PCA is very useful when looking at disease from a genetic point of view where the data recorded can have hundreds of variables. Therefore PCA is used to reduce this set of data to a much more manageable size and allow diagnosis to take place. This technique has shown itself to be useful in genetic studies of lung cancer (Polat and Gunes, 2008) where the genetic characteristics of the cancer were investigated.

PCA has also been used for differentiation of cancerous and non-cancerous tissue (Molckovsky et al., 2003) using an optical technique known as Raman Spectroscopy where the data recorded is a set of peaks due to energy transfers. Such data can have many thousands of data points, but only a few peaks in each trace. Simple peak detection would not be the most efficient method of extracting information as the traces are made up of a superposition of energy transfers, and as such some molecules may share similarities with others. PCA can therefore be used to compare a new measurement against a bank of known traces from molecules, in much the same method as face recognition.

In order to demonstrate the technique, this chapter will finish with a short example using principal component analysis to detect air bubbles in an ultrasonic

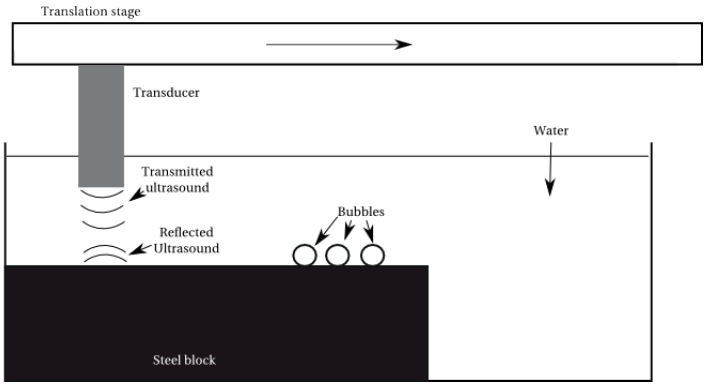

Figure 5.3: Ultrasound set-up to collect B-scan image of steel block underwater with bubbles on surface.

image of a steel block underwater. While the concepts of ultrasound will be explained in full later in the thesis, this example is simple enough to explain without an introduction to its mechanics.

5.4 Example: Using PCA to segment an Ultrasound Image

Figure 5.3 shows the set-up that was used in order to collect date for this simple example. The ultrasound source produced a pulse of high frequency sound towards the steel block, and then the reflected echoes were recorded. The recorded data is presented in Figure 5.4, where each vertical line of pixels in this B-scan is an individual pulse-echo trace, known as an A-scan. In this B-scan image there are 250 separate A-scans, with 2000 data points each.

Three A-scans are shown in Figure 5.5, each recorded after reflection from a different material in the image. Figure 5.5a shows the reflection from the steel block, presenting itself as a large solitary pulse of ultrasound. Figure 5.5b shows the reflection from the steel block from an area in which there lies a bubble. This presents itself as a large pulse preceded by a smaller pulse, which is due to the reflection of the ultrasound from the air trapped inside the bubble. The third ultrasound A-scan (Figure 5.5c) shows the recorded signal where there is

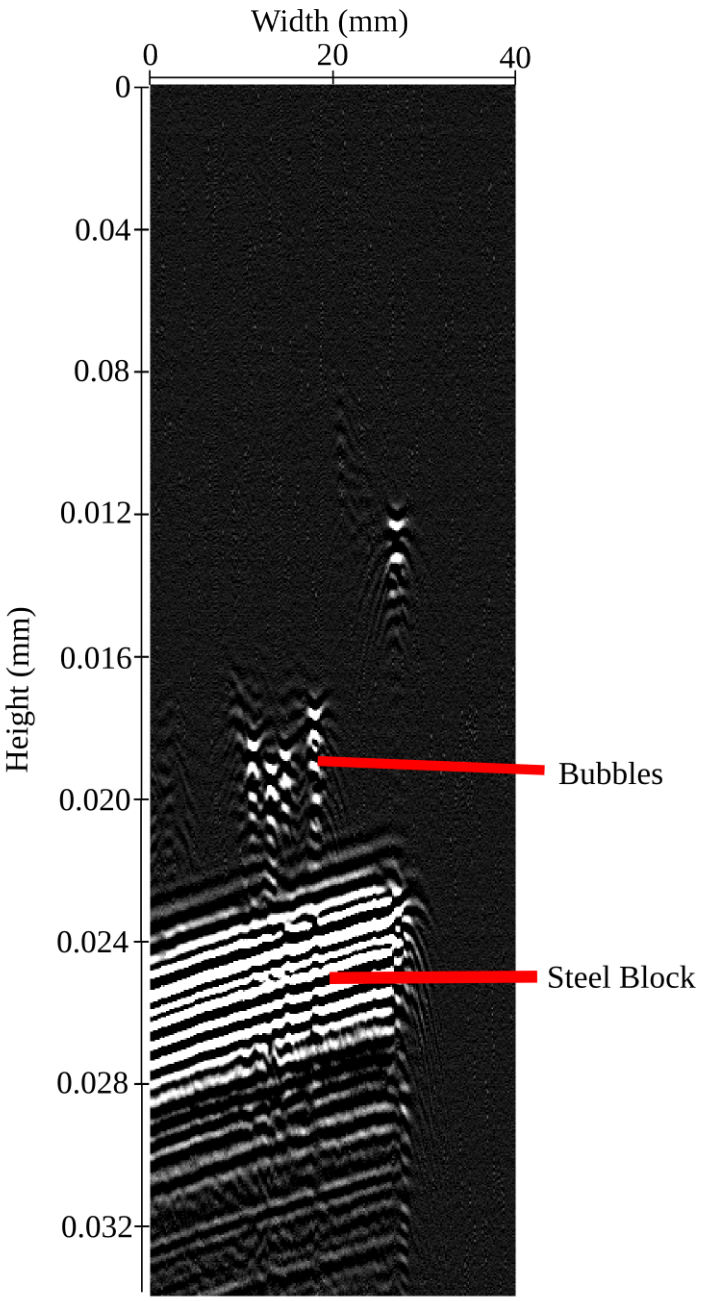

Figure 5.4: B-scan showing Steel block submerged in water with bubbles showing.

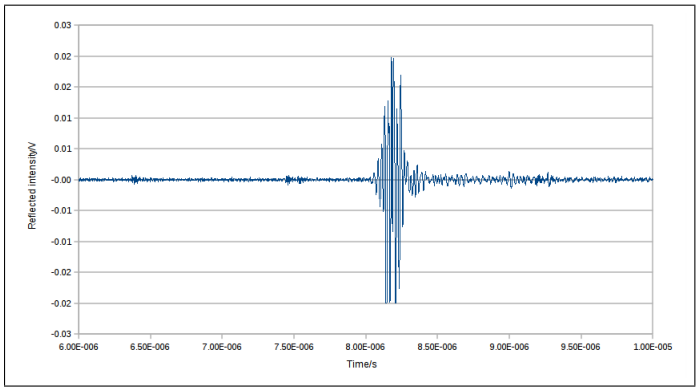

(a) A-scan of Steel block submerged underwater

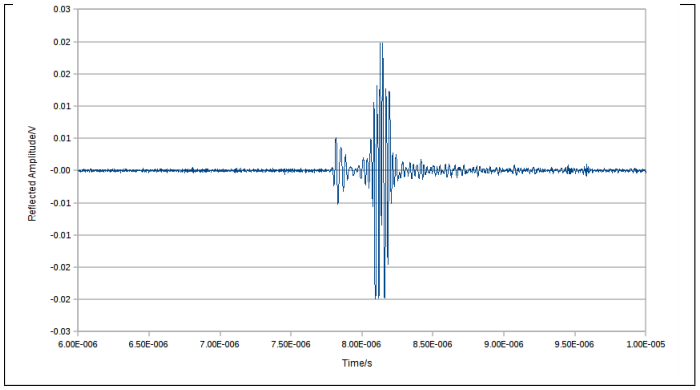

(b) A-scan of Steel block submerged underwater with bubbles

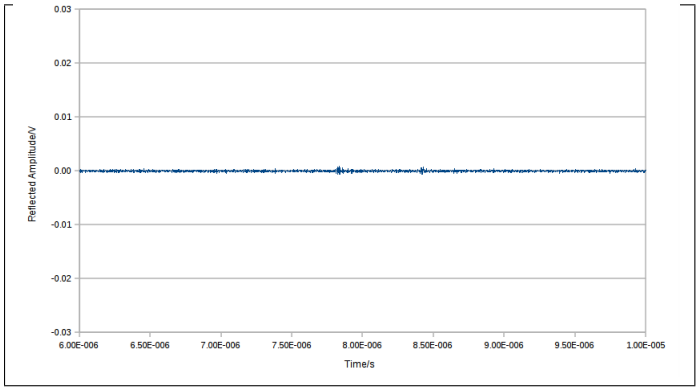

(c) A-scan of no target underwater

Figure 5.5: Choice ultrasonic A-scan's from steel block experiment

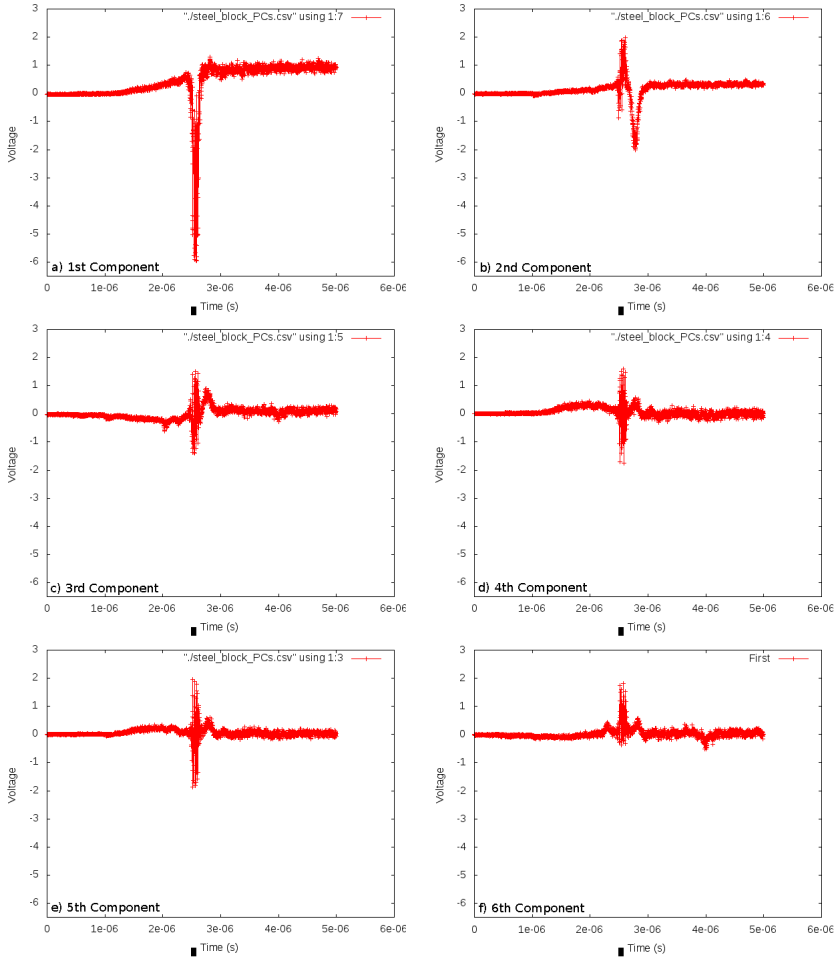

Figure 5.6: First six derived principle components from ultrasonic dataset.

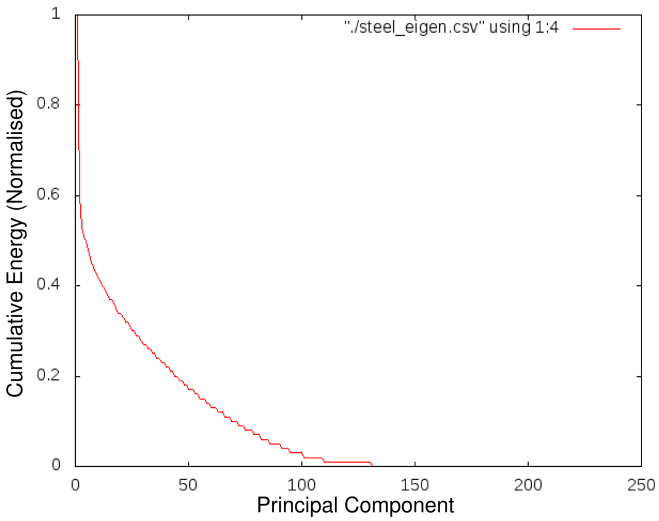

Figure 5.7: Cumulative energy of principal components from Steel block data set.

no object for the ultrasound to be reflected off, as expected the A-scan exhibits a very low reflected amplitude with no major features.

By looking at the A-scans in Figure 5.5, a trained ultrasound user would be able to say whether or not there was a bubble on the steel surface. The aim of this exercise is to see whether or not PCA, as described above, can allow a computer to detect A-scans with bubbles mathematically.

The first step in using PCA is to prepare the data. For this, each A-scan is normalised and shifted so that the first point at which the signal rises above 25% of the total height occurs in the same time sample in all the A-scans. After this has been carried out for the data, the covariance matrix is created. With this data set, the covariance matrix is 2000 by 2000 data points, which is very large and would take even the fastest available PC sometime to calculate the eigenvectors. As derived above, the eigenvectors are calculated, in mathematical package Scilab, using the alternate method (with a matrix of 250 by 250 instead) and then converted to the principal components using simple matrix multiplication. The first six of these are presented in Figure 5.6.

The reason for only presenting the first six principal components is illustrated in Figure 5.7 where the cumulative energy of each principal component is shown.

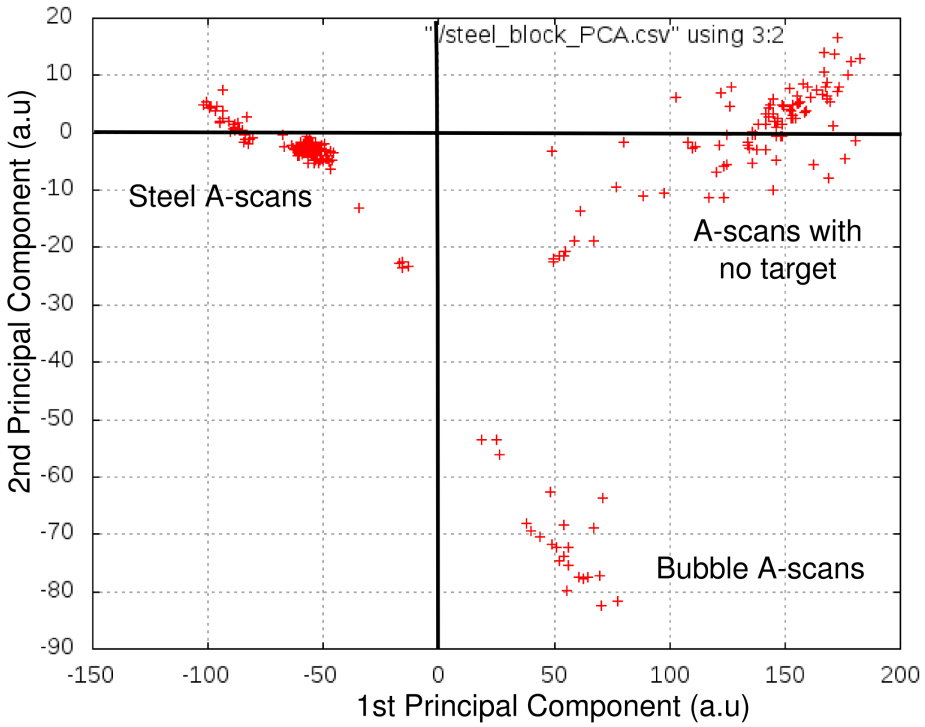

Figure 5.8: First and second principal component weightings for steel block experiment, showing segmentation of A-scans

As expected there is a sharp drop off in energy for each principal component, with 50% of the cumulative energy held in the first 10 or so principal components. One would expect the decrease to be exponential. However, this graph is not showing a true exponential decay. It is believed that this is due to the normalisation routine maximising the null signal (which is effectively noise) when there is no steel block to be recorded, meaning that there is a lot of stochastic variation in the last 83 A-scans.

Nevertheless, it is clear that the first six principal components (equating to around 90% of the total cumulative energy) do exhibit features similar to the A-scans presented in Figure 5.5. The first principal component shows similar features to the A-scan (Figure 5.6a) of the steel block (Figure 5a), and the second principal component exhibits dual peaks (Figure 5.6b), similar to an A-scan of a bubble lying on the surface of the steel, as shown in Figure 5.5b.

The data can now be represented as a weighting vector of these principal

components. It is this vector that allows the computer to interpret the data and determine the content of each A-scan. By looking at the principal components in Figure 5.6, it was possible to see similarities between steel A-scans and the first principal component, and similarities between the bubble A-scans and the second principal component. Therefore, one would expect that there would be differentiation in the first two values of the weighting vector between these two different types of A-scan. In order to visualise this, a simple scatter plot is created of the full data set, using the first component of the weighting vector as the X-axis, and the second as the Y-axis. Such a plot is presented in Figure 5.8.

There are three main clusters of data points, and by relating each point in the scatter plot to an individual A-scan that comprised the B-scan in Figure 5.4, it is possible to group the visible clusters according to features. By doing this, it is possible to discern that the group of A-scans in the top left hand side of the plot come from the A-scans of the steel block. This is expected as by occuring in this area in the graph, a reconstructed trace would have a large peak in the trace (due to the large 1st component weighting), and no second peak (due to the almost negligible 2nd co-efficient peak, which contains the second peak due to bubbles).

The group of A-scans occupying the lower right hand area of Figure 5.8 are found to come from the areas of the steel block where bubbles have formed on the surface. This large negative weighting of the second component is due to this component presenting a dual peak form, and thus large weighting amplifies these in any reconstructed traces.

The last group of data points in Figure 5.8 are found to come from the area in the b-scan where there is no object to be scanned. These exhibit a large positive weighting of the first principal component, which in reconstruction would reduce the size of the large negative peak in the first principal component trace (Figure 5.6a). From the scatter plot it looks as if there are more data points in the

cluster belonging to this set than the steel set, however, this is just due to the resolution of the scatter plot. The points associated with the steel block are much closely grouped, due to the A-scans having much more similarity between each other. The A-scans associated with the recordings of no object have a much more random nature due to noise (which is amplified during the normalisation process), and these have a larger spread in the scatter plot.

What the scatter plot in Figure 5.8 does show is that given an A-Scan, the computer would be able to determine if the scan came from the steel block or steel block with bubbles by calculating its co-ordinates in this two-dimensional space. The data supplied in this example were just a set of 1D recordings of voltage against time, and the technique itself did not concern itself with the method of recording. Therefore this has shown that the technique has applicability for interpreting one dimensional data regardless of the information that it contains.

5.5 Conclusion

This chapter has introduced the technique of principal component analysis for the interpretation of one dimensional data. Through the example of a simple ultrasound B-scan of a steel block underwater, it has been shown that the technique can differentiate features in the image, without needing to know much about the actual data.

In simple terms, the principal component analysis technique took the A-scans, which were 2500 data points in length, and represented them in the form of two data points (the x and y axis respectively). From these two data points it was possible to detect what material was recorded in each A-scan.

The following chapter relating to the application of a fibre optic confocal microscope for diagnosing dental caries will apply PCA in order to interpret the data. The data recorded from the fibre optic confocal microscope is just one

dimensional voltage against time, and so the example above using one dimensional ultrasound data is transferable.

Bibliography

S. Costa and S. Fiori. Image compression using principal component neural networks. *Image and Vision Computing*, 19(9-10): 649–668, August 2001. doi: 10.1016/S0262-8856(01)00042-7. URL http://www.sciencedirect.com/science?_ob=ArticleURL&_udi=B6V09-43MMXCH-7&_user=10&_rdoc=1&_fmt=&_orig=search&_sort=d&_docanchor=&view=c&_acct=C000050221&_version=1&_urlVersion=0&_userid=10&md5=42db2e9db30d42f2cc86a26f8959aa39.

R.D. Dony and S. Haykin. Neural network approaches to image compression. *Proceedings of the IEEE*, 83(2):288–303, 1995. ISSN 0018-9219. doi: 10.1109/5.364461.

IT Joliffe and Bjt Morgan. Principal component analysis and exploratory factor analysis. *Statistical Methods in Medical Research*, 1(1):69–95, March 1992. doi: 10.1177/096228029200100105. URL http://smm.sagepub.com/cgi/content/abstract/1/1/69.

A Molckovsky, LM Wong Kee Song, M. G. Shim, N. E. Marcon, and B. C. Wilson. Diagnostic potential of near-infrared raman spectroscopy in the colon: Differentiating adenomatous from hyperplastic polyps*1, *2, *3. *Gastrointestinal Endoscopy*, 57(3):396–402, March 2003. doi: 10.1067/mge.2003.105. URL http://www.sciencedirect.com/science?_ob=ArticleURL&_udi=B6WFY-4F29BM9-11&_user=10&_rdoc=1&_fmt=&_orig=search&_sort=d&_

docanchor=&view=c&_acct=C000050221&_version=1&_urlVersion=0&_userid=10&md5=49ea0895ed91543ca9822ba26280da17.

K. Polat and S. Gunes. Computer aided medical diagnosis system based on principal component analysis and artificial immune recognition system classifier algorithm. *Expert Syst. Appl.*, 34(1):773–779, 2008. URL http://portal.acm.org/citation.cfm?id=1244586.

M Turk and A Pentland. Eigenfaces for recognition. *Journal of Cognitive Neuroscience*, 3(1):71–86, January 1991. doi: 10.1162/jocn.1991.3.1.71. URL http://dx.doi.org/10.1162/jocn.1991.3.1.71.

Chapter 6

FOCOM for the detection of caries

6.1 Introduction

In this chapter, a fibre optic confocal microscope utilising miniature aspheric lenses will be used to detect dental caries. Due to the assumption that the eventual end-user will not be an expert in analysis one dimensional FOCOM data, and the reduced resolution of the system compared with previous work, principal component analysis will be used to interpret the data. Therefore this chapter is to be seen as a culmination of previous chapters in to miniature optics and PCA.

It is useful to recap briefly what has been discussed before in order to best understand the experimental investigation of this chapter. A fibre optic confocal microscope (FOCOM) is a confocal microscope where a single mode optical fibre acts as the pinhole. This allows the scanning optics of the microscope to be detached from the rest of the system, and allows for greater miniaturisation and suitability for the oral cavity.

Previous work has shown that the technique is useful for the diagnosis of early dental caries. In this work, the lesions symptomatic of dental caries were shown to present themselves as series of peaks in the recorded measurements. Healthy tooth enamel presents itself as a single intensity peak, due to the refractive index mismatch between air and enamel. A lesion classified as a white spot lesion will have a dual peak due to the mismatch between air, enamel, and then during the course of the lesion, fluid and enamel. A brown spot lesion will present itself as a messy series of multiple peaks due to increased scattering from the randomly remineralised enamel structure.

The previous work made use of desktop sized optics, and while being able to achieve high resolutions (3μm), the dimensions of the system made it unsuitable for going in the mouth. As was shown in the previous chapter in to miniature optics, aspheric lenses are a good replacement for the bulk optics and do produce a confocal effect. However, due to the reduced diameter of the lenses which reduces

the NA of the system, the resolutions attained are not as high as previously reported. This means that from the start of using the system, the recorded data is worse than in previous reports and therefore new methods of interpreting the data are required.

Early on in this investigation, when faced with this problem, it was thought that the parameters of the recorded traces such as the number of peaks, full width half maximum and asymmetry (this is calculated by considering the peak as two half-peaks, and calculating a FWHM for both then taking the square of the difference) would be sufficient in order to make a diagnosis. However, these parameters rely on the recorded peak tending towards a Gaussian approximation, and especially in the case of brown spot lesions, this is not the case. In order to carry out a more in depth analysis and comparison between the recorded scans, it was decided that principal component analysis (as discussed in the previous chapter) would be a good candidate.

With principal component analysis, each FOCOM scan is considered a large set of random variables (in this case each variable is a voltage measurement for a specific location in the tooth). The values of these variables, once measured, produce the characteristic peaks of sound, white spot and brown lesions. However, for each FOOM scan there are several thousand random variables, and many contain little to no information. Principal component analysis serves to reduce this number to a more manageable amount and allows the data to be represented in a much simpler fashion to allow for easier interpretation of the data.

6.2 Methodology

In this investigation, a fibre optic system, similar to that of Rousseau et al. (2007), is used to record depth profiles through areas of enamel in clinically extracted teeth. The aim of the investigation is to demonstrate the combination of

miniature lenses and principal component analysis as a method for the detection and characterisation of caries lesions.

Even though the idea is to create a system suitable for the oral cavity, the system used in this investigation still makes use of a bulky translation stage for axially scanning the objective. Once the limitation in the size of the translation stage is conquered, the actual optics part of the system are transferable.

After recording the depth profiles, principal component analysis is used to produce a two dimensional 'map' of the recorded scans. From this, the clustering of the recorded scans (similar to that in the previous chapter) will be analysed in order to show the ability of principal component analysis to differentiate between sound and lesioned enamel. In order to strengthen this model, a further set of scans from sound enamel and lesions will be recorded and projected on to the map.

6.2.1 FOCOM

In order to collect FOCOM scans for this investigation, a laboratory based system was created similar to that of Rousseau et al. (2007). As shown in Figure 6.1, light from an 808nm laser source is coupled into a single mode optical fibre, making use of mirrors M1 and M2 for alignment and lens L1 for focusing. The light exiting from the SMF is collimated by an aspheric lens (L2, NA=0.27) and passed through an optical chopper (637Hz) in order to increase the signal to noise ratio and to enable the discrimination of the required signal from back reflections from the fibre.

The chopped light is then focused by an aspheric lens (L3, NA=0.55NA), acting as the objective, which is mounted on a axial translation stage. A signal generator drives this stage using a sinusoidal voltage output, allowing the lens L3 to scan its focal point back and forth through a sample typically at around 1.8 mms^{-1}. At this velocity, the lock-in amplifier is averaging the reflected signal

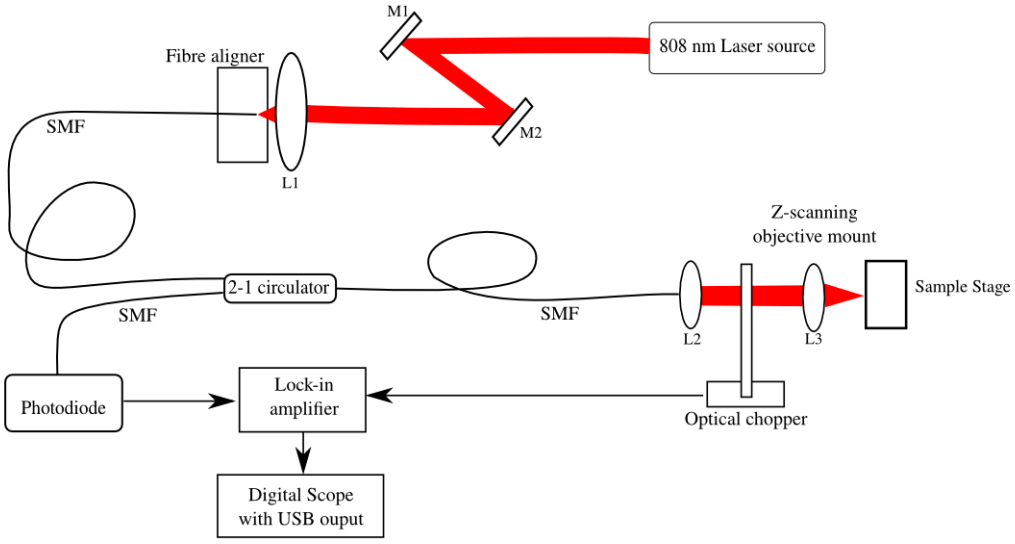

Figure 6.1: Desktop FOCOM system with aspheric lenses for scanning dental samples.

over roughly 1.8μm which equates to around 7 cycles of the chopper.

Light that returns from the focal point is then returned through the collimation optics L2 and delivered to a photodiode (Thorlabs, PDA 101). After signal processing through a lock-in amplifier (Femtolabs) the resulting signal is displayed on a digital oscilloscope (Tektronics) presenting the depth profile on it's display, and permitting the storage of the data to a USB memory stick, in the comma separated value (CSV) text format, for transfer to a computer for analysis. Analysis was carried out using SCILAB on a Linux workstation running Ubuntu Intrepid Ibex. Graphical representation of the data was later produced using an OpenOffice.org Spreadsheet. Statistical analysis was undertaken using the R programming language through the Rkward frontend.

6.2.2 Principal component analysis

One of the most important considerations of using principal component analysis is to make sure that the data is suitably aligned. There is no standard method for aligning the data from a FOCOM system, and so it was chosen that the data should be aligned to the front face of the scan. In order to achieve this, each scan

in the data set was normalised and then temporally shifted so that the first point at which the scan rose above 25% of the total height was aligned to a common point.

From this normalised and aligned data, the average FOCOM scan was calculated and subtracted in order to produce the mean-shifted data set. This was so that the mean of the total data set was zero and allows a useful covariance matrix to be produced. In order to find the eigenvectors of the covariance matrix, the more efficient method (derived in Chapter 3) was used. Then, using in built functions, the eigenvectors and eigenvalues of this matrix were then calculated and sorted with decreasing eigenvalue. The important eigenvectors were chosen from the energy contained in their respective eigenvalues and the principal components of the data set were calculated by multiplying these eigenvectors to the mean shifted data set.

Each FOCOM scan in the mean shifted data set was then projected on to these principal components to produce a set of weightings for each scan. These weightings were then used to analyse and represent the data in two dimensional scatter plots in order to assess clustering and distances in this new set of axis.

6.2.3 Dental samples

A variety of teeth (incisors and molars) that had been removed for orthodontic reasons were collected and stored in Thymol solution. Once ready to be scanned, the teeth were removed from the Thymol solution, rinsed in water and then air dried.

The tooth was then placed in the holder and then using the micrometer stage, the area of interest (sound enamel or lesion) was brought towards the focus of the objective using an infrared viewfinder for assistance. Once a suitable trace was displayed on the oscilloscope screen, the averaging function of the oscilloscope was turned on (N=4) and the trace was stored to the USB storage device in a

comma separated value format text file.

Two sets of data were recorded for this study. The first data set contained 6 sound enamel and 6 lesion scans, it is from these data that the 'reference' principal components are calculated. Afterwards, 17 sound enamel and 23 lesion scans are recorded. These scans are then analysed using the 'reference' principal components as an example of comparing 'unknown' scans to a known model, as would be case when using such a device in the clinic.

6.3 Results

Figure 4.15a shows the average recorded FOCOM scan from a mirror, and Figures 6.2a and 6.2b show the recorded FOCOM scans from sound and lesioned enamel respectively. All three scans have been normalised and aligned horizontally so that the point at which the signal first rises above 0.25 (i.e. 25% of the peak height) occurs at the same position.

This point of reference was chosen over the conventional centre peak-alignment because where lesions are concerned, it is difficult to choose a discernible peak due to the random nature of the lesions reducing the 'Gaussian' approximation of the recorded signal. In this method, the assumption is that the first peak that rises above 0.25 is the actual front surface of the sample, with following peaks due to subsurface structure.

The distribution of the FOCOM scans in FOCOM-space are shown in Figure 6.3, with the magnitude of each scan along the third principal component shown in Figure 6.4. The scatter plot shown in Figure 6.3 includes the second set of FOCOM scans that were recorded to verify the principal component model.

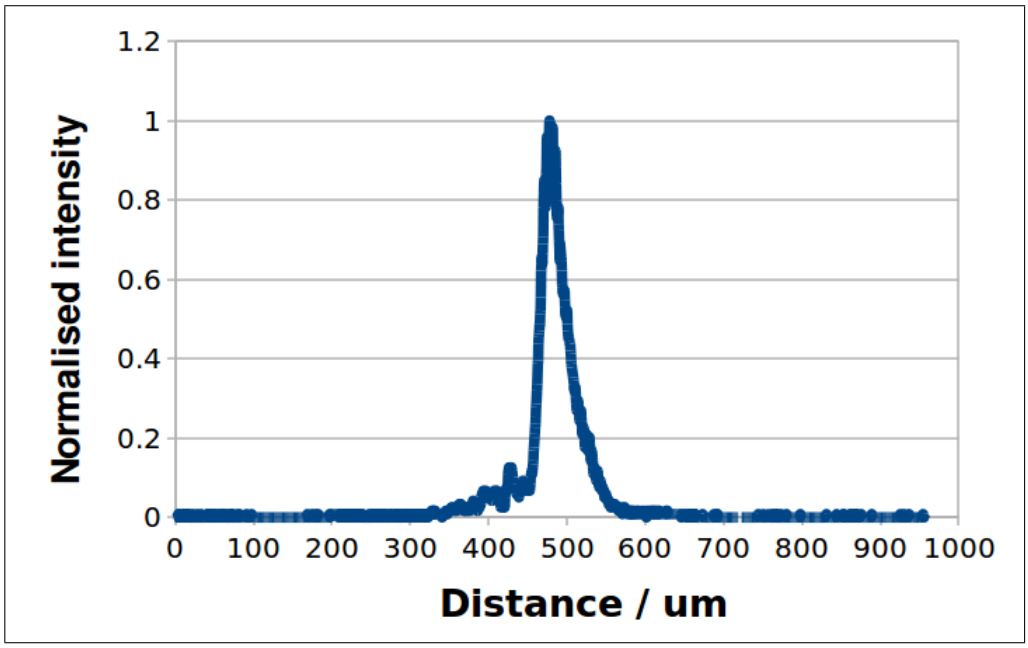

(a) Axial scan of a sound enamel surface

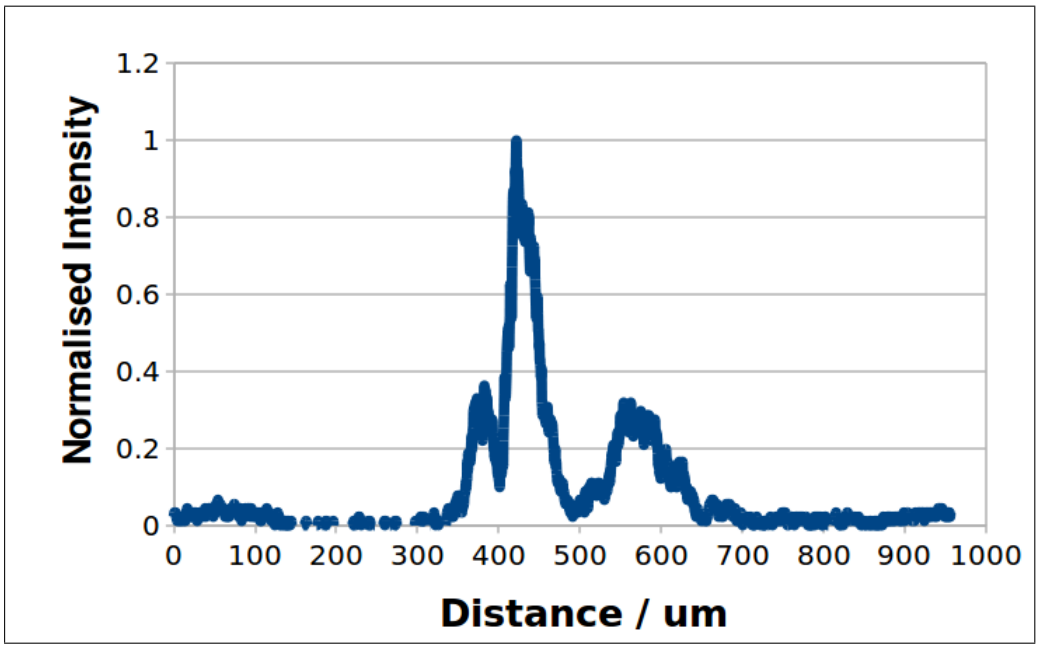

(b) Axial scan of lesioned enamel surface

Figure 6.2: Typical dental sample scans from the FOCOM system.

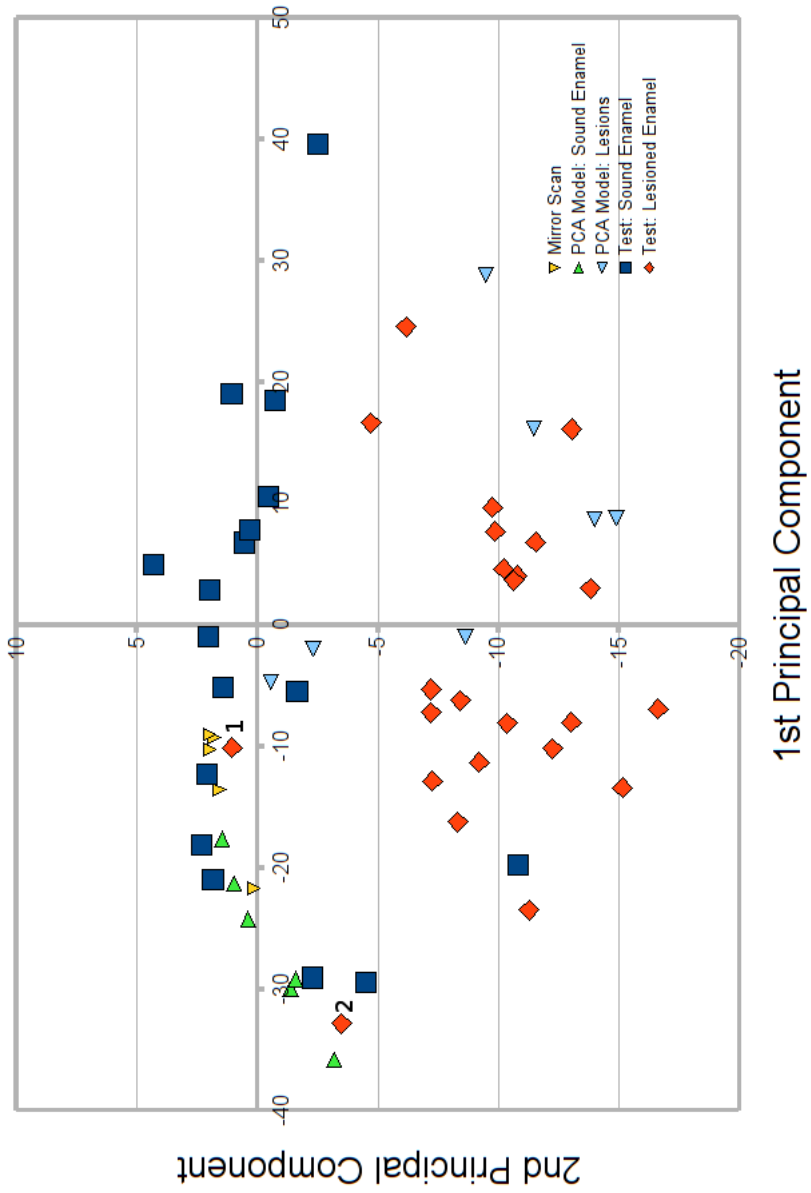

Figure 6.3: Distribution of weights of principle components from FOCOM data.

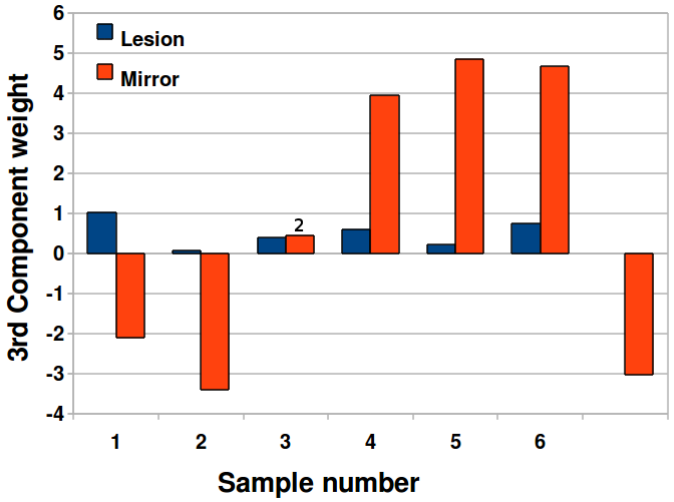

Figure 6.4: Magnitude of weighting of third principle component in FOCOM scan data

6.4 Discussion

In order to make the discussion easy to follow, the principal components that have been derived using the reference scans shall be discussed first. Afterwards, the 'test' scans shall be discussed.

6.4.1 Reference scan set

The scan shown in Figure 4.15a is an example of the simple test used to confirm that the confocal microscope is functioning properly (Zucker and Price, 1999) and also in order to allow comparison of the biological scans. This mirror scan has a FWHM of 52($\pm$0.08)μm and is very symmetrical in shape, except for the spherical abberation effects in the leading edge as mentioned in Chapter 4.

The scan presented in Figure 6.2a is that of an area of enamel that was visually inspected and deemed to be sound enamel. This has a similar shape to the mirror scan, except for a slight broadened FWHM of 54 ($\pm$0.08)μm. This is due to the enamel not being an ideal reflector, and due to the natural variation in the enamel structure.

Both the mirror and the sound enamel however are different to the lesion as shown in Figure 6.2b. This lesion shows a decreased signal to noise ratio, and the appearance of a second peak behind the front face peak. This is due to the light traversing an area of lower refractive index (water or air filled) and the encountering enamel again and thus the FOCOM detects the Fresnel reflection from this interface. The use of the FWHM as a measure of the 'soundness' of the enamel is now more difficult. The difference in the appearance in the lesion to that of sound enamel and the mirror is easy to see from a viewpoint of someone well versed in looking at FOCOM depth profiles, the use of principal component analysis is in order to see if the computer can be 'taught' to discriminate between sound and lesioned enamel in less obvious cases.

The scatter plot in Figure 6.3 of the 1st and 2nd components of the weighting vector for the reference FOCOM scans show a clustering of the sound enamel scans near the mirror scans. This is as expected due to the similarity in the shape of the FOCOM scans. It was shown using a Wilcox test that there was only a small significant difference between the 1st components of the reference sound scan and the mirror ($U=2$, $p<0.017$), and 2nd components of the reference sound scan and mirror scan ($U=3$, $P<0.03$).

FOCOM scans of lesioned enamel do not generally fall in the same location in FOCOM-space as that of sound, due to the increased number of peaks in the recorded FOCOM scan. Using the Wilcox test, it was shown that there is no real significant difference in the 1st component of the sound scan and the lesion scan ($U=0$, $p<0.001$), but a large significant difference in the 2nd component ($U=38$, $p<0.013$).

There are however two lesion scans that fall close to the mirror scans in FOCOM-space. One of these, labelled 1 on Figure 6.3, on inspection of the notes taken when collecting the scan, it was noted that the lesion was very small. Therefore, it might be concluded that the illumination from the FOCOM system

missed the white spot lesion, or hit both lesion and sound enamel, and that this is indeed sound enamel that has been scanned. This raises the need for a visible light to be added to the FOCOM system so that a user can see precisely where on the tooth the FOCOM is measuring, especially where small lesions are concerned.

The other lesion scan, labeled 2, falls further away from the mirror area in the first and second principal components, but much further away on the third component, as shown in Figure 6.4. The previously mentioned lesion scan has a much smaller component in the 3rd principal component, which was comparable in dimension to that of sound enamel.

This raises the question of the significances of the various principal components. By looking at the FOCOM scans of various points around the FOCOM space (as shown in Figure 6.5), one can infer a set of relations between position and features in a FOCOM scan. In the 1st principal component, one can see that the width of the recorded FOCOM scan becomes wider as the value on this component becomes more negative. This is backed up by looking at the widths of the mirror scans that are at either extremity of the mirror scan clusters, where the most negative mirror scan has a FWHM of 56.1μm, and the most positive mirror scan has a FWHM of 48.9 ($\pm$0.04)μm. The average mirror scan sits in the middle of this cluster, and as mentioned before has a FWHM of 52.2 ($\pm$0.04)μm.

By calculating the FWHM for the whole data set of mirror and sound scans (lesions can not be approximated by a Gaussian), there is a strong negative correlation (r=-0.98) between the FWHM and the position along the 1st principal component. As the value on the 1st component becomes more positive, there is increased 'activity' in the recorded FOCOM scan. This is thought to be related to high frequency noise components in the recorded scans, which would increase as the signal to noise ratio drops in the normalised FOCOM scan due to increased scattering due to the lesioned enamel.

In the second component, it is noticeable that as this component becomes more

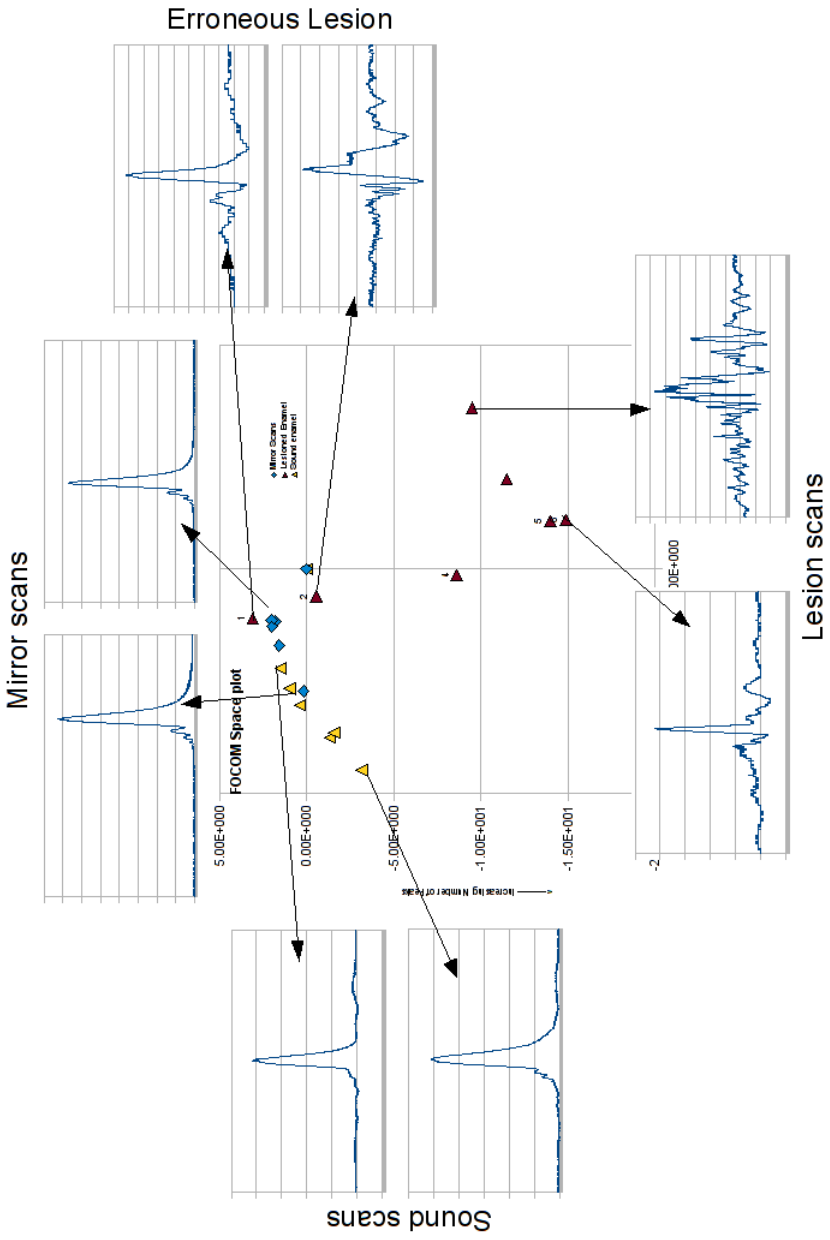

Figure 6.5: Distribution of scan morphology around PCA space.

negative, the number of peaks in the recorded scans increases, with scans lying well below the axis having several 'wide' peaks. These traces are characteristic of white spot lesions, as found by Rousseau et al. (2007). It was also calculated that there was a strong correlation between the 2nd principal component and the sharpness in the front rise of a FOCOM peak than with the back peak.

This may be useful for detecting defects in the enamel as lesioned enamel would typically have a more asymmetric FOCOM peak than sound due to the difference of materials in a lesion. In the early stages of the disease process the surface enamel, although intact, is more porous with some loss of mineral content, but not total loss of the rod like structure. It is believed that this is what is indicated here. Potentially this is a very important measure in relation to disease diagnosis and treatment planning.

The asymmetry of FOCOM peaks was calculated and shown to have a low correlation to the 2nd principal component (r=0.04) and a higher correlation with the 3rd component (r=-0.37). This weak relation is shown in the bar chart in Figure 6.4 where the lesions typically have a larger magnitude along the 3rd component. Sound enamel scans typically have a lower 3rd component due to a smaller, but not negligible, level of asymmetry.

However, it is naive to try and relate a specific principal component to a measurement that is normally used for comparing scans from the FOCOM, such as FWHM or asymmetry. This is because the method of using PCA compares the FOCOM scans is based upon the mathematical correlations in the scans as if they were a one dimensional data set with arbitary units; the algorithm doesn't know that the data is voltage measurements which may take on a Gaussian appearance. Therefore, while it is possible to state anecdotal relationships between the components and 'visual' attributes, the true relation is hidden much deeper in the samples.

6.4.2 Test scan set

As shown in Figure 6.3, the second set of 'sound' enamel FOCOM scans lie to the right of the reference set. This was unexpected as it was thought that they would lie to the left of the mirror scans due to the mirror scan being the hypothetical resolution limit of the system. A Wilcox test shows that there is a small significant difference in the weighting of the 1st component between the reference sound scan and the test sound scan ($U=10$, $p<0.002$). It is thought that this change in position is due to the fact that the measurements were recorded on different occasions. However, it was shown above that the 2nd principal component holds more significance when differentiating between sound and lesioned scans.

As expected the lesion scans lie in a much more negative position along the 2nd principal component in Figure 6.3. There is a very large significant difference between the 2nd component weighting of the test lesion scans and the original reference sound scans ($U=139$, $P<0.0001$). There is also a very large significant difference between the 2nd components of the test sound scans and test lesion scans ($U=407$, $p<0.0001$). This shows us that the method is able to differentiate between sound and lesioned enamel when using a reference set built up from previously taken scans.

In order to calculate the sensitivity and specificity of this technique, the 2nd principal component was used. A threshold of -5 was chosen whereby any scans with a 2nd principal component weighting of less than this were assumed to be diagnosed as coming from sound enamel. Those scans that had a larger 2nd principal component weighting than this were said to be diagnosed as lesioned enamel. This was compared to the visual inspection notes of the tooth surface in order to calculate the percentages of false positive and false negative diagnoses. This gave the sensitivity of the technique to be 0.96, with 22 out of 23 sound enamel scans correctly identified. The sensitivity was found to be 0.9, with 26 out of 29 lesion scans correctly identified.

The current commonplace methods for the detection of dental disease have been found to have lower sensitivity's than found here, with the dental explorer technique being found to have a sensitivity of 0.39-0.59 (McComb and Tam, 2001) and X-rays found to have a sensitivity of 0.5 (Selwitz et al. 2007). However, X-rays do have a similar specificity of 0.8 (Selwitz et al., 2007). In regards to an emerging optical technique, the figures for the FOCOM device are higher than those that have been found for the QLF (sensitivity=0.68, specificity=0.7) technique (Pretty, 2006).

6.5 Conclusions

By developing a FOCOM with miniature lenses, it has been shown that it is possible to detect dental caries by recording depth profiles of areas of enamel and classifying, or diagnosing, these using principal component analysis. Sensitivity of 0.96 and specificity of 0.9 have been calculated for this method by choosing a threshold of -5 along the 2nd principal component.

This has immediate applications in detecting interproximal caries where visual observation is difficult due to the tight spacings between teeth. In such cases, radiography is the prefered method of diagnosis. The FOCOM system would allow the characterisation of the inter-proximal surface in to sound or lesioned without the use of ionising radiation.

Such a system could be used by a dentist to make a more quantitative clinical assessment as to whether an area of enamel is sound or not. If found to be outside the area in FOCOM-space of the sound reference scans, the FOCOM tool can then be used to make a measurement on the lesion to determine it's size and activity as demonstrated in previous work (Rousseau et al., 2007). Further work is now under way to miniaturise the scan head further, including optics to increase the effective NA of the system, in order to produce a hand held scanning

device for use in clinical trials.

Bibliography

D McComb and L. E. Tam. Diagnosis of occlusal caries: Part i. conventional methods. *J Can Dent Assoc*, 67(8):454–7, 2001.

I. A. Pretty. Caries detection and diagnosis: Novel technologies. *Journal of Dentistry*, 34(10):727–739, 2006.

C. Rousseau, S. Poland, J. M. Girkin, A. F. Hall, and C. J. Whitters. Development of Fibre-Optic confocal microscopy for detection and diagnosis of dental caries. *Caries Research*, 41(4):245, 2007.

R. H Selwitz, A. I Ismail, and N. B Pitts. Dental caries. *The Lancet*, 369(9555):51–59, 2007. doi: 10.1016/S0140-6736(07)60031-2. URL `http://www.sciencedirect.com/science/article/B6T1B-4MRGVD0-13/2/73cdc9abd2a8177a4bdf4445b6d2dee9`.

Robert M. Zucker and Owen T. Price. Practical confocal microscopy and the evaluation of system performance. *Methods*, 18(4):447–458, August 1999. doi: 10.1006/meth.1999.0812. URL `http://www.sciencedirect.com/science/article/B6WN5-45S48FT-5N/2/645a0d2a4f2f62a999e94dbb1839e32b`.

Chapter 7

Ultrasound and dentistry

7.1 Introduction

In the previous chapters, optical interactions with dental materials have been used to detect tooth decay. However, as good as the resolutions provided by microscopy are, the technique does not have the depth of field needed to accurately monitor dental erosion.

As stated in Chapter 2, one of the main problems of monitoring dental erosion is the lack of a reference point in the surface of the tooth. Ultrasound solves this problem by allowing depth profiles to be recorded up to depths of several millimetres, with a reference point arising in the form of the enamel-dentine junction.

In order to understand how this works, this chapter will introduce the concepts of ultrasonic waves, and in particular their propagation through and interactions with dental materials. This will be useful for the subsequent chapter where ultrasound is applied as a technology for the detection of dental disease.

7.2 Ultrasonic waves

A wave, by definition, is the transfer of energy without the transfer of mass. In the case of mechanical waves, it is the motion of particles in the medium that propagate the wave. The particles themselves do not actually propagate, they merely oscillate around their location. There are two classes of mechanical waves, transverse where the particles oscillate perpendicularly to the direction of the wave propagation and longitudinal where the particles oscillate parallel to the direction of the wave propagation.

In materials, the longitudinal oscillation of particles creates a pressure wave due to subsequent compressions and expansions of the material (as shown in Figure 7.1). Sound is a classic example of a pressure wave propagating through a medium (most commonly air) at a frequency that the human ear can detect.

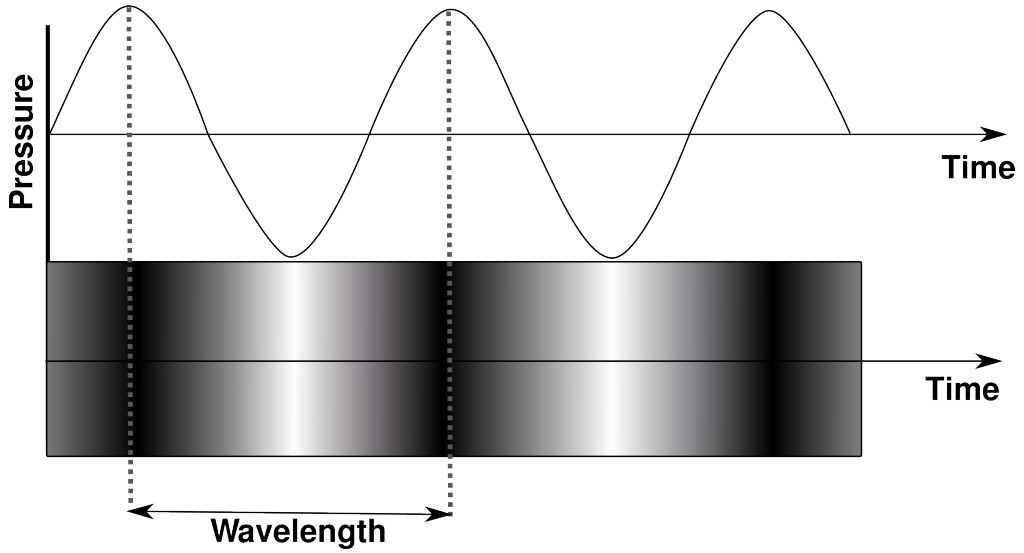

Figure 7.1: Longitudinal pressure wave in a material

Acoustic waves above the limit of human hearing are said to be 'ultrasonic' and 20kHz is commonly taken as the cut-off frequency for audible waves.

7.2.1 Ultrasonic propagation

Ultrasound travels through a medium as a series of compressions and expansions. The speed at which these actions can happen is dictated by the structure of the medium. The wavelength of a sinusoidal ultrasonic wave is the distance between a point of maximum pressure and an adjacent point of maximum pressure. It is related to the velocity and frequency of the wave as

$$c = f\lambda \tag{7.1}$$

The wave velocity depends on the compressibility of the medium (assuming it is isotropic), a property known as Young's Modulus, Y,

$$c = \sqrt{\frac{Y}{\rho}} \tag{7.2}$$

Where ρ is the density of the medium. It is important when considering diagnostic applications, where the wavelength partially dictates the resolution of an ultrasonic measurement system, to take into account that the constant velocity of ultrasound in an isotropic medium relates the wavelength to the frequency. For a specific material a higher frequency means a shorter wavelength and, as will be discussed later, leads to a higher resolution.

As longitudinal waves propagate through objects, it is common that they meet boundaries of different materials where the effects of reflection and/or transmission can occur. These effects are due to the difference in the properties of the materials leading to the concept of acoustic impedance. Acoustic impedance (Z) can be thought of as a resistance to 'carrying the wave' by the material and is defined as the product of the material density and the longitudinal wave velocity,

$$Z = \rho c \tag{7.3}$$

Since the acoustic impedance of a material governs the propagation of the ultrasound wave, the boundary between two materials of different acoustic impedance is very important. The Fresnel equation for intensity of reflection coefficients is written

$$R = \left(\frac{Z_1 - Z_2}{Z_1 + Z_2} \right)^2 \tag{7.4}$$

where R is the reflection coefficient, and Z_1 and Z_2 are the incident and subsequent materials' acoustic impedances. From this the amount of ultrasound energy reflected from (or transmitted through) a boundary can be calculated.

7.2.2 Ultrasonic pulses

Figure 7.1 shows a continuous pressure wave through a material, however, for ultrasonic imaging applications it is a pulsed wave that is commonly used. In order to understand how a pulsed ultrasonic wave may occur, consider a block of

rubber attached to a rigid frame at each end. If one were to pinch one area of the rubber and compress it, the rubber surrounding the pinched area would stretch due to the whole volume rubber being fixed in size by the rigid frame.

This causes an area of compression (high pressure) and surrounding expansion (low pressure). The elastic nature of rubber means that once the pressure is removed from the pinched area it will expand back to its normal size. However, it may over expand slightly in this reflex action, causing the surrounding area to compress. This compression/expansion action may repeat itself through the rubber causing a pressure wave to propagate away from the original site of the pinch.

These equivalent ultrasonic pulses are very useful for imaging because as a single pulse propagates through a medium there will be reflections and transmissions, due to different objects made of different materials, producing wavelets that can be recorded. By measuring the temporal separation of these wavelets and using the simple relationship between speed, distance and time, a linear map, known as an A- scan, of these objects can be created. After a brief discussion of how these ultrasound pulses are created, a generic ultrasound system will be described which could be used to create such A - scans.

7.3 Imaging considerations

Before introducing the methods of generating ultrasound and its applications, it is important to discuss the parameters that relate a useful ultrasound system to its application, and how these come about in a practical manner. The parameters to be discussed are axial and lateral resolutions and signal to noise levels.

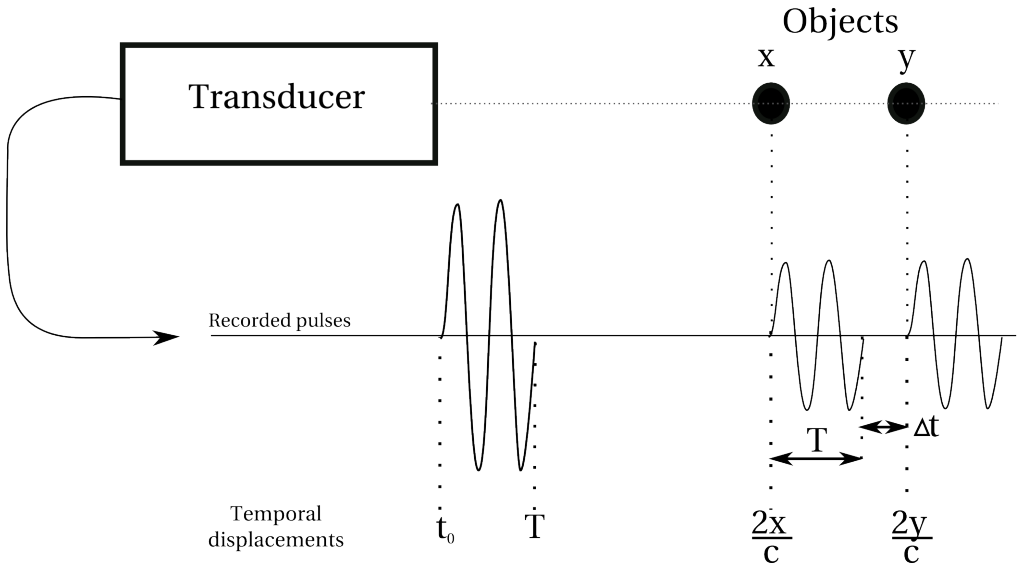

Figure 7.2: Axial resolution of an ultrasound transducer, adapted from Cobbold (2007)

7.3.1 Resolution

Generally speaking the resolution of an ultrasound system depends on how small the beam or pulse size is in relation to the object that is to be measured. The lateral resolution of an ultrasound system is dependent on the width of the beam, i.e., what is the size of the area over which the ultrasound energy is active. This is related to the physical dimensions of the source of the ultrasound and to the operating frequency of the ultrasound.

In terms of the axial resolution (the minimum resolvable axial separation of objects (Cobbold, 2007)), this is similar to the Rayleigh criterion that was discussed in the previous chapter on microscopy whereby the ability to distinguish two closely placed objects was reliant on the beam properties. This concept is shown in Figure 7.2 where a transducer at time to emits a pulse of ultrasound of period T (seconds). There are two objects at position x and y, which reflect this pulse. The recorded pulse-echo trace is displayed below, where the return pulses from the objects can be seen to occur at $\frac{2x}{c}$ and $\frac{2y}{c}$.

It is said that these two objects can be resolved if the difference between these

two times is greater than zero:

$$\delta t = \frac{2x}{c} + T - \frac{2y}{c} > 0 \tag{7.5}$$

If these temporal displacements are converted into distances, then one can see that under this assumption, these objects must be separated by a distance that is less than half the wavelength ($\lambda = \frac{c}{f} = cT$) of the pulse, as shown by

$$2x + cT - 2y > 0 \frac{\lambda}{2} < (y - x) \tag{7.6}$$

7.3.2 Signal to noise ratio

The signal to noise ratio (SNR) of an ultrasonic system is the ratio of the received signal amplitude to the background noise levels (Cobbold, 2007). It is very important to maximise the SNR of an ultrasonic measurement system because, if the SNR is too low, useful information can be lost in the background noise of the recorded data. The SNR can be stated as:

$$SNR = \frac{\text{Maximum instantaneous Signal Amplitude}^2}{\text{Noise Power}} \tag{7.7}$$

Under the assumption that the speckle noise can be neglected, and that the background noise is white over the bandwidth frequency, δf, then it is possible to show a relation between the transducer energy and SNR. The energy of a sinusoidal wave is $E = \frac{1}{2}TA^2$, where T is the period of the wave, and if the noise power density is said to be N, then through substitution into (7.7) we get

$$SNR = \frac{2E}{TN\delta f} \tag{7.8}$$

However, for accurate signal detection, the bandwidth of the system should be twice the operating frequency, and so a simple relation between the energy of

the signal to the noise density of the receiving electronics, given by:

$$SNR = \frac{E}{N} \tag{7.9}$$

Therefore, one can see that in order to increase the SNR, the useful energy of the signal must be maximised, while keeping the noise density of the receiving electronics at a minimum.

7.4 Transducers and the generation of ultrasound

Ultrasound waves are just high frequency sound waves and as such the generation of ultrasound is quite similar to the generation of sound. For low-frequency ultrasound, conventional speakers can be used, or even whistles (for example the high pitched whistles used for training dogs). For imaging applications, higher frequencies are desired for higher resolutions and different techniques are employed. Most modern ultrasound transducers employ materials which exhibit piezoelectric properties. A material is piezoelectric if it shows a relationship between stress and electric field. These materials can either produce an electric field under the influence of stress and strain, or change their dimensions under the influence of an electric field.

In order to produce ultrasound, the material is connected to a signal generator which varies the electric field across the material. The direct relationship between field and stress mean that the dimensions oscillate at the same frequency as the generator. By choosing the frequency and orientation of the motion carefully, the material can be made to disrupt its surrounding medium at ultrasonic frequencies and thus emit ultrasound.

The first materials demonstrated to be piezoelectric were crystals, notably quartz and Rochelle Salt, discovered in the late 19th century by Curie brothers. Nowadays however polymers and ceramics are common materials for transducers,

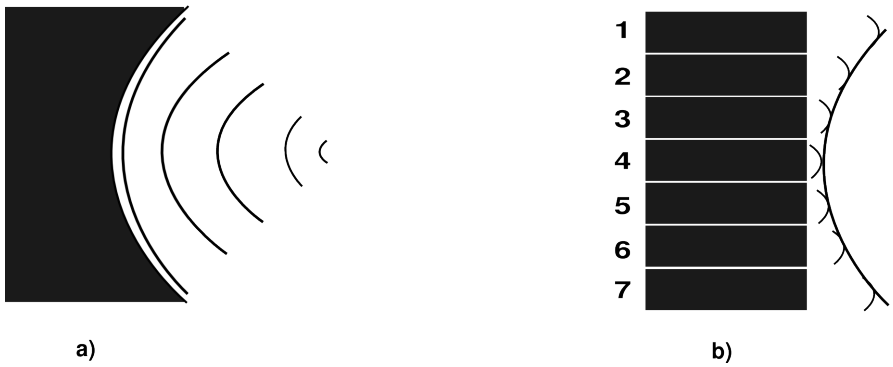

Figure 7.3: Focussing of an ultrasound beam using a) curved active face and b) by using a multiÂelement array

such as PVDF and PZT.

A transducer can be made to focus an ultrasound beam in three ways, firstly with a curved active face (Figure 7.3a), secondly by using an acoustic lens, and finally by incorporating several individual transducers into an array as shown in Figure 7.3b. In the former, the curved active face produces a curved wave front which converges to a point after a propagation distance. The focal distance of the transducer depends on the diameter and curvature of the active face. In the following chapter a transducer making use of this focussing technique shall be demonstrated for investigating dental samples.

The latter focussing technique of using an ultrasound array is much more complicated and requires the elements to produce their pulses of ultrasound in a phased manner in order to produce a time delay between wavefronts. In Figure 7.3b, elements 1 and 7 have been activated first, followed by elements 2 and 6, then 3 and 5 and finally the central element 4. The focussing arises by the resultant wavelets producing a curved wave front which converges to a point, as shown in Figure 7.3b. In much the same way as this focusing, an ultrasound array can also be used in order to steer an ultrasound beam in a specific direction.

7.4.1 Ultrasound system

Figure 7.4 shows the two common ultrasound system set-ups. In the first, there are two transducers where one transmits the ultrasound and the second receives it. This is known as a through transmission set up. The second arrangement, as shown in Figure 7.4b uses only one transducer whereby the transducer after transmitting the ultrasonic wave, switches to receiving circuitry and picks up any reflected signal. This is known as a "Pulse/Echo" arrangement. The time of arrival between the echoes and the velocity of sound in the material can be used to determine distances to the objects causing the echoes. This allows ultrasound to be used as a non-invasive imaging and measuring tool.

7.5 Ultrasound as a diagnostic tool

As is the case with many technologies, ultrasound emerged as a useful tool from research carried out during wartime. Paul Langevin is widely credited as the father of the ultrasonics field with his pioneering work into echolocation. Through his work, he demonstrated ultrasound as a tool for locating submerged submarines (Cheeke, 2002) and also showed it as a method for probing materials (Hendee and Ritenour, 2002). However, it would not be until the Second world war that Langevin's work would prove to be a useful and practical solution.

In the years between the two world wars, the Russian scientist Sokolov demonstrated ultrasound as a tool for non-destructive testing applications (Hendee and Ritenour, 2002). It was also around this time that ultrasound was being used as therapeutic aid for cancers and physical therapy which was enabled by the era's work into the development of high intensity sources (Cheeke, 2002).

The first example of ultrasound being used for a diagnostic medical purpose was in 1953 at MIT, where engineers showed that the gall bladder was able to be detected using a pulsed ultrasound system (Ludwig and Struthers, 1949).

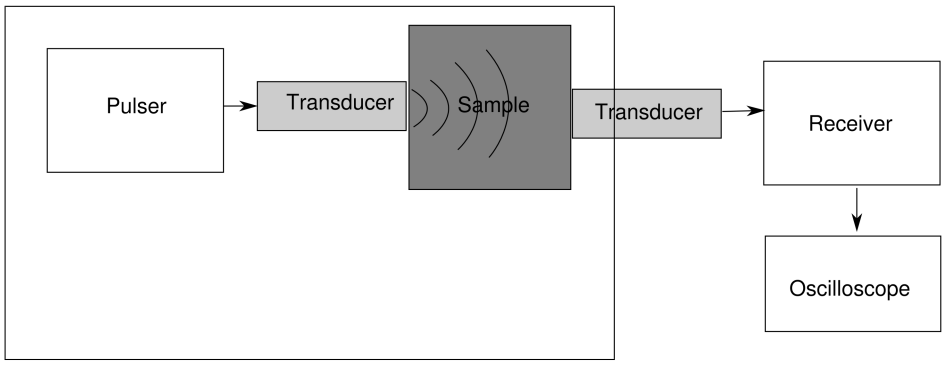

(a) Through transmission ultrasound

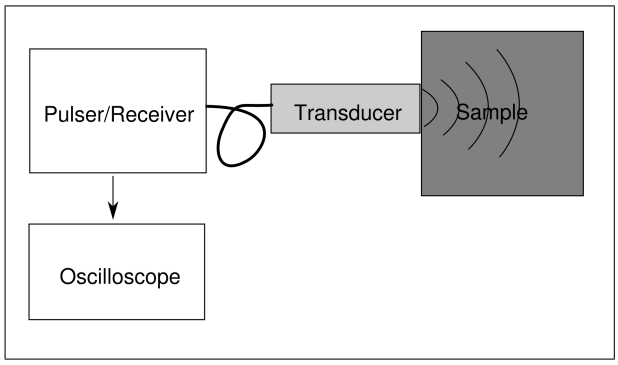

(b) Pulse-echo ultrasound

Figure 7.4: Modes of operation of an ultrasound system, a) pulse-echo and b) through-transmission

1954 saw work being carried out in Sweden where researchers used an ultrasound system to monitor heart activity thus creating the field of echo-cardiology (Edler and Hertz, 2004).

However, one of the earliest and most important papers in the field of ultrasonography came out of Scotland. In 1958 engineers at Babcock, led by clinician Ian Donald (Donald et al., 1958) placed a bag of butchers meat underwater and showed that an ultrasound system was capable of visualising the bones inside the meat. This was followed up with more clinical applications (Donald and Brown, 1961) where interfaces between body tissues were imaged in-vivo, and such techniques are now common-place in hospitals worldwide.

With the improvement in technology since the early days of ultrasonography in medicine, the number of different applications has increased, the most well known being the imaging of the foetus in order to monitor its growth. Other applications include Doppler ultrasound for monitoring blood flow (Aaslid et al., 2009) and for monitoring of the placement of spinal injection needles (Galiano et al., 2005). The vast number of applications of ultrasound in medicine is outside the scope of this chapter. However, any textbook on biomedical ultrasound will serve as a good reference such as that of (Cheeke, 2002) and (Cobbold, 2007).

In order to appreciate the difficulties in applying ultrasound to dental materials, it is helpful to discuss the behaviour of ultrasound waves in these constituent materials. Through this discussion, an appreciation should arise that the observation of the internal structures of teeth has more similarities to industrial ultrasound than conventional biomedical ultrasound.

7.6 Ultrasound behaviour in dental materials

The nature of the materials in teeth raise issues in transfering the technique from conventional biological applications to dentistry. One of the most obvious

differences in dental materials to conventional biological tissues is that of size. Teeth are typically much smaller than the usual targets in the medical ultrasound field, such as foetuses and cancer tumours. Therefore consideration should be made that higher resolutions are required in order to provide useful measurements.

It should also be appreciated that due to the hardness of the enamel and dentine, much higher velocities of ultrasound occur. Biological applications typically use a figure of 1540ms^{-1} for the velocity of ultrasound, whereas in the dental tissues the velocities are much higher (v_{enamel}=6500ms^{-1}, $v_{dentine}$=4500ms^{-1}) (Ng et al., 1989).

However, one of the main problems in applying ultrasound to dental materials is that of signal amplitude reduction due to acoustic impedance. With the conventional tissue (Z=1.5MRayl), an ultrasound beam propagating from source and through a standard coupling agent (Z=1.48 MRayl) is incident on a waterlike-tissue boundary. At this boundary the reflection co-efficient can be calculated using the Fresnel's expression (Equation 7.4) to be 0.05%, meaning that 99.995% of the ultrasound energy is transferred into the sample. Compare this to the dentistry situation whereby the acoustic impedance of enamel is much higher (Z=17 MRayl, taken from (Ng et al., 1989) than standard coupling agents, and it can be calculated that only 29.5% of the ultrasound energy is transferred in to the sample.

In order to record an A-scan from an ultrasound sample, one must be able to record the pulse that has been reflected off internal structure and exited the sample. In conventional biological ultrasound imaging, differences in acoustic impedence between soft tissues result in only 5% of ultrasound energy being reflected to the detector. In the case of dental ultrasound, the enamel-dentine-junction (EDJ) will reflect around 8% the pressure wave amplitude.

From an application's viewpoint, the difference is that there are currently gel-like coupling agents that bridge the gap between the transducer and soft tissue.

This allows greater transfer of energy in to conventional soft targets, than with a dental target where most energy is lost before entering through reflection at the surface of the hard enamel. There will be a short discussion on some research in to coupling agents for the dental application in the following section on previous work carried out in dental ultrasound.

The other loss mechanism for ultrasound is that of attenuation, however, this effect is much lower in dental tissues than biological tissues due to the ordered microstructure of the dental materials (compared to the non-homogenous tissue structure). Also, the effect of attenuation is a function of depth, and the dimensions of a tooth are generally smaller than that of conventional biological targets so the effect is reduced.

7.7 Ultrasound as a diagnostic technique in dentistry

7.7.1 Introduction

Although ultrasound has been explored for diagnostic applications in medicine since the mid 1950s, it has not developed into a mature diagnostic technique in dentistry. In the early 1960's it was shown that dental structures could be observed using ultrasound. However, further work has been sporadic despite ultrasound images having been utilised in both the longitudinal and transverse modes for probing the inner structures of teeth.

The following is a review of ultrasound as a diagnostic technique in dentistry, and specifically observing the internal structures of the actual tooth. For a more complete review including ultrasound as a tool for cleaning and also diagnosing periodontal disease, (Ghorayeb et al., 2008) is a useful reference.

7.7.2 Early work

The first ultrasound investigations into dental structures were in the early 1960s when Baum used a 15 MHz transducer to produce a B-scan image of the jaw, allowing them to image the pulp chambers of some of the teeth (Baum et al., 1963). Such images were crude due to the technology available at the time, but did show promise.

The ground breaking work by Lees and Barber in 1968 reduced the frequency back to 4 MHz, but showed that is was possible to distinguish between the front face of the tooth and the enamel dentine junction in their recorded A-scans (Lees and Barber, 1968). The resolution of these experiments was very low, and in contrast to the paper by Baum, who stated that frequencies above 30 MHz should be used for useful measurements (Baum et al., 1963). While Baum used an underwater scanning technique using a custom ophthalmic ultrasound device, Barber and Lees used a thin rod of aluminium as the coupling medium and a custom PZT transducer.

A further and more in depth report by Barber et al expanded their investigation into pulse echo measurements in human, canine and bovine incisors (Barber et al., 1969). This work was carried out with a resolution of 0.5mm, although the authors believed that layers of around 0.3mm in thickness might be visible. In contrast to the work of Baum, Barber et al found no difference in the recorded echo signals between ex vivo and in vivo teeth.

Most of the early work considered indirect coupling through media such as water(Baum et al., 1963), aluminium rods (Lees and Barber, 1968; Barber et al., 1969) and even mercury but one of the major breakthroughs of later work was that the data was able to be collected by direct coupling in some cases without surface preparation. This has major implications where diagnostic clinical applications are to be considered.

The work by Barber et al (1969) also presented the first velocity measurements

of ultrasound in dental tissues, giving the velocity of sound to be 6250ms^{-1} (in human enamel) and 3500ms^{-1} in dentine (Barber et al., 1969). The use of ultrasound as a method of determining the properties of enamel (both healthy and diseased) was furthered in a report by Peck et al who introduced scanning acoustic microscopy (SAM) as a method (Peck et al., 1989). This is a destructive technique, but invaluable for collecting parameters that would be used in later work.

7.7.3 Mid-work

Much of the work published in the mid 1980's to 90's concerned the material properties of dental tissue and ultrasound propagation. Out of this period, one of the most cited papers is that of Ng et al. (1989)â which concerned the velocity of ultrasonic waves in dental tissue. In this paper, the velocity of ultrasound in enamel was found to be 6500 ($\pm$190)ms^{-1} and 4050 ($\pm$30)ms^{-1} in dentine (Ng et al., 1989).

The velocities that were reported in this paper agreed closely with those by Barber et al. (1969), and later work by Maev et al. (2002). An earlier paper by Maev's group on the changes of the enamel through demineralisation showed that different acoustic impedances (measured values of Z were shown to vary by around 57%) arise due to demineralisation, pointing towards a technique for the detection of caries (Ng et al., 1989) with a later conference paper detailing the technique (Ng et al., 1993).

The work carried out by Lost's group used velocity information as a method of characterising dental tissues, producing two-dimensional velocity charts that enabled the distinguishing of enamel and dentine (Lost et al., 1992; John et al., 1994). These results also showed that there was variation in the velocity of ultrasound in dentine depending on how deep in the dentine it was observed (Lost et al., 1992). This finding would be investigated in further work by this

group into the anisotropy of dental materials for ultrasound propagation (John, 2004) where they found that the direction of the incident ultrasound was very important, but that the micro-structure of the enamel was too small to produce appreciable diffraction effects in images.

Mezawa et al used a similar technique to Lost et al in order to characterise teeth, noting that ultrasound provided a good non-destructive technique for investigating the thickness of tooth enamel (Mezawa et al., 1999). Through this work they investigated the relationship between the hardness of the tooth and its acoustic properties, such as degree of calcification, distribution of dentinal tubules, and density of the dentin matrix (Mezawa et al., 1999).

Also around this time, Bab et al developed an ultrasonic caries detector (UCD) based on surface wave interactions around caries lesions (Bab and Feuerstein, 1999). This device was later shown to have a higher sensitivity than radiographs, but a lower specificity (Matalon et al., 2007). This was in contrast to an earlier study which showed that the device had a higher specificity during in-vitro studies (Matalon et al., 2003), with the decrease thought to be due to moisture in the oral cavity.

In an example of the intra-disciplinary nature of bringing ultrasound to diagnostic dentistry, one paper from 1996 reported on its use from an archeological viewpoint (Yang, 1996). In this report, it was noted that ultrasound provided an excellent non-destructive technique for classifying teeth.

7.8 Current developments

By the turn of the century the acoustic microscope had also been shown to be useful for measuring enamel thickness (Maev et al., 2000). The technique, however, still required sectioning as it was based on the two-dimensional velocity diagrams produced earlier. However, by 2002, Maev was able to show that,in some cases,

surface preparation was not needed for detecting caries and other properties of dental tissues with their microscope (Maev et al., 2002).

Later, the same group would report in a book chapter that a 50 MHz acoustic scanning microscope would be able to accurately measure the thickness of enamel and dentine, and also show subsurface signs of disease (Denisova et al., 2007). However, in the book chapter, inadequate statements of methodology is given and as such the analysis of some of the presented B-scans is questionable. Images of bisected teeth are presented without proper scale bars, and as a result, it's difficult to compare the temporal B-scan data to the thickness of the enamel shown.

The Maev group went on to publish work using the 50 MHz system to measure the adhesion of restorations at the cemento-dentine junction (Denisova et al., 2009). This paper featured work presented in Denisova et al. (2007) but with an expanded description of methodology. With the 50 MHz probe, a resolution of 0.07mm was achieved. The probe was used to record C-scans of the surface of a tooth with an underlying restoration. Poor adhesion showed up as a larger reflection in the C-scans (due to an acoustic impedance mismatch across the boundary), with close agreement with microscope images.

The early 21st century saw a large number of papers published on the clinical applications of ultrasound in dentistry. Huysmans showed that ultrasound was a good technique for monitoring enamel thickness with little surface preparation (Huysmans and Thijssen, 2000). This work was carried out using a 15 MHz commercial ultrasound transducer producing a 0.4mm resolution. The ultrasound measurements were compared to microscope measurements with good agreement ($p=0.9$), with good reproducibility between examiners shown in a later paper by the same group(Louwerse et al., 2004). Furthermore, with the resolution available at 15 MHz, they estimated that it should be possible to diagnose dental erosion within 1 to 1.5 years in children from the first measurement and that increasing

resolution would improve this(Huysmans and Thijssen, 2000).

Echodentography was the name coined by Ghorayeb in 2002 for observing the internal structures of teeth with ultrasound (Ghorayeb and Valle, 2002). This work used a 10 MHz ultrasound probe successfully to verify PSpice models of teeth from earlier work by the group. One of the more important parts of this paper examined the safety of ultrasound in diagnostic dentistry, where they found that the non-complicated aspect of the setup and the inherent non-ionising nature of ultrasound were in harmony with FDA guidelines (Ghorayeb and Valle, 2002).

The dental ultrasound group at UCLA published a number of interesting papers on recording B-scans of teeth for quantitative measurement (Culjat et al., 2003) and crack detection (Culjat et al., 2005). In the former, a 10 MHz probe was used to record a circumference scan of a tooth, showing the EDJ in 360 degrees, which showed very good agreement to the bisected tooth (Culjat et al., 2003). The coupling agent used in this experiment was water. However the group also undertook some work on a novel couplant based on solder for dental applications (Culjat et al., 2005). This material allows a better matching of the acoustic impedance of the transducer to the tooth. Studies with mice also showed that the couplant has a low level of toxicity (Culjat et al., 2005).

A Turkish group of dentists also attempted to use ultrasound for the monitoring of dental erosion with limited success (Bozkurt et al., 2005). An industrial transducer was used to measure the thickness of an area of the tooth's enamel before being ground away with abrasive paper. The measurement was then repeated and verified against a sectioned image taken with a polarised microscope. The technique was also tested for intra-examiner correlation, in which the measurements were repeated by a second examiner. The value for this correlation was found to be 0.479 ($p>0.050$). The authors of the paper were mostly practising dentists, and stated that this moderate correlation was due to the repeated readings on the device not being "the exact same numbers". This suggests there

is an issue of non-technical users finding difficulty in using a commercial probe designed for another purpose, in this case the airline industry (Bozkurt et al., 2005).

This group also turned attention to detecting caries with their ultrasound system. They found that an 11 MHz commercial ultrasound thickness gauge (Novascope, Israel) was capable of an 86% specificity and an 88% sensitivity for detecting white spot lesions (Yanikoglu et al., 2000). This thickness gauge had a 1.5mm circular contact face, the small size being found to be useful for recording readings on curved surfaces with no preparation, using a glycerine coupling agent. A later paper also showed that the ultrasound technique had 'positive' correlation between examiners (Tagtekin et al., 2008).

7.9 Summary

The literature has shown that ultrasound is a plausible and safe method for the monitoring of enamel thickness, which has implications for the monitoring of dental erosion. Limited data also exists on the use of ultrasound for diagnosing dental caries. However, the use of this is more complex due to the size of early caries lesions limiting the detection in the pulse-echo mode. For caries detection, the acoustic properties of the dental materials must be considered and the amplitude of the return signal considered.

From the literature one can see the obvious advantages of the high frequencies available through SAM. However, the technique itself is much more complex than that of conventional pulse-echo ultrasound in terms of sample preparation. Where sample preparation has been reduced, the system is still a long way from being miniaturised for use in the oral cavity.

The research also shows that any ultrasound device that is to be made available to the dental practitioner should have this application in mind. It has been

shown that there is only a moderate agreement between examiners using the ultrasound technique, and it is the belief of this writer that this is because of non-technical users.

The following chapter reports on work on a novel miniature focused high frequency ultrasound (35 MHz) transducer primarily for the diagnosis of dental erosion. The aim with this transducer was to bridge the gap between the previous lower frequency work and the SAM work, with a view to add more quantifiable results to the field.

Bibliography

R Aaslid, T M Markwalder, and H Nornes. Noninvasive transcranial doppler ultrasound recording of flow velocity in basal cerebral arteries. http://thejns.org/doi/abs/10.3171/jns.1982.57.6.0769, May 2009. URL http://thejns.org/doi/abs/10.3171/jns.1982.57.6.0769.

I Bab and O Feuerstein. Device and method for the ultrasonic detection of dental caries (Patent), February 1999.

F E Barber, S Lees, and R R Lobene. Urasonic pulse-echo measurements in teeth. *Archives of Oral Biology*, 14(7):745–760, July 1969. ISSN 0003-9969. URL http://www.ncbi.nlm.nih.gov/pubmed/5257202. PMID: 5257202.

G Baum, I Greenwood, S Slawski, and R Smirnow. Observation of internal structures of teeth by ultrasonography. *Science*, 139(3554):495–496, February 1963. doi: 10.1126/science.139.3554.495. URL http://www.sciencemag.org/cgi/content/abstract/139/3554/495.

F. O Bozkurt, D.A. Tagtekin, O Hayran, G. K. Stookey, and F.C. Yanikoglu. Accuracy of ultrasound measurement of progressive change in occlusal enamel thickness*1. *Oral Surgery, Oral Medicine, Oral Pathology, Oral Radiology, and Endodontology*, 99(1):101–105, January 2005. doi: 10.1016/j.tripleo.2004.05.013. URL http://www.sciencedirect.com/science?_ob=ArticleURL&_udi=B6WP1-4D58BSW-5&_user=10&_rdoc=1&_fmt=&_orig=search&_sort=d&_docanchor=&view=c&_searchStrId=

961790146&_rerunOrigin=scholar.google&_acct=C000050221&_version=1&_urlVersion=0&_userid=10&md5=7ea0027d0bc6c41496ff796aad74d088.

J. David N. Cheeke. *Fundamentals and applications of ultrasonic waves*. CRC Press, 2002. ISBN 0849301300, 9780849301308.

R S C Cobbold. *Foundations of biomedical ultrasound*. Oxford University Press US, 2007. ISBN 0195168313, 9780195168310.

MO Culjat, RS Singh, DC Yoon, and ER Brown. Imaging of human tooth enamel using ultrasound. *Medical Imaging, IEEE Transactions on*, 22(4):526–529, 2003. ISSN 0278-0062. doi: 10.1109/TMI.2003.809141.

MO Culjat, RS Singh, ER Brown, RR Neurgaonkar, DC Yoon, and SN White. Ultrasound crack detection in a simulated human tooth. *Dentomaxillofac Radiol*, 34(2):80–85, March 2005. doi: 10.1259/dmfr/12901010. URL http://dmfr.birjournals.org/cgi/content/abstract/34/2/80.

L. A. Denisova, R.G. Maev, V.K. Leontjev, A Denisov, G.C. Grayson, F.S. Rusanov, E. Y. Bakulin, D. Y. Gavrilov, and T. V. Grineva. A study of the adhesion between dental cement and dentin using a nondestructive acoustic microscopy approach. *Dental Materials: Official Publication of the Academy of Dental Materials*, 25(5):557–565, May 2009. ISSN 1879-0097. doi: 10.1016/j.dental.2008.10.011. URL http://www.ncbi.nlm.nih.gov/pubmed/19297016. PMID: 19297016.

L.A. Denisova, R.G. Maev, F.S Rusanov, A.R. Maeva, A.F Denisov, D.Yu. Gavrilov, E.Yu. Bakulin, and F.M. Severin. Fundamental potential for acoustic microscopy evaluation of dental tissues. In *Acoustical Imaging*, pages 81–88. 2007. URL http://dx.doi.org/10.1007/1-4020-5721-0_10.

I Donald and T G Brown. I. demonstration of tissue interfaces within the body by ultrasonic echo sounding. *Br J Radiol*, 34(405):539–546, September

1961. doi: 10.1259/0007-1285-34-405-539. URL http://bjr.birjournals.org/cgi/content/abstract/34/405/539.

I Donald, J MacVicar, and T G Brown. Investigation of abdominal masses by pulsed ultrasound. *Lancet*, 1(7032):1188–1195, June 1958. ISSN 0140-6736. URL http://www.ncbi.nlm.nih.gov/pubmed/13550965. PMID: 13550965.

I. Edler and C. H. Hertz. The use of ultrasonic reflectoscope for the continuous recording of the movements of heart walls. *Clinical Physiology and Functional Imaging*, 24(3):118–136, 2004. URL http://dx.doi.org/10.1111/j.1475-097X.2004.00539.x.

Klaus Galiano, Alois Albert Obwegeser, Gerd Bodner, Martin Freund, Herbert Maurer, Florian Stefan Kamelger, Reinhold Schatzer, and Franz Ploner. Real-time sonographic imaging for periradicular injections in the lumbar spine: A sonographic anatomic study of a new technique. *J Ultrasound Med*, 24(1): 33–38, January 2005. URL http://www.jultrasoundmed.org/cgi/content/abstract/24/1/33.

S.R. Ghorayeb and T. Valle. Experimental evaluation of human teeth using noninvasive ultrasound: echodentography. *Ultrasonics, Ferroelectrics and Frequency Control, IEEE Transactions on*, 49(10):1437–1443, 2002. ISSN 0885-3010. doi: 10.1109/TUFFC.2002.1041085.

S.R. Ghorayeb, C.A. Bertoncini, and M.K. Hinders. Ultrasonography in dentistry. *Ultrasonics, Ferroelectrics and Frequency Control, IEEE Transactions on*, 55 (6):1256–1266, 2008. ISSN 0885-3010. doi: 10.1109/TUFFC.2008.788.

William R. Hendee and E. Russell Ritenour. *Medical imaging physics*. John Wiley and Sons, 2002. ISBN 0471382264, 9780471382263.

M. C. D. N. J. M. Huysmans and J. M. Thijssen. Ultrasonic measurement of enamel thickness: a tool for monitoring dental erosion? *Journal of*

Dentistry, 28(3):187–191, March 2000. doi: 10.1016/S0300-5712(99)00063-9. URL http://www.sciencedirect.com/science?_ob=ArticleURL&_udi=B6T86-3YF3VVT-4&_user=10&_rdoc=1&_fmt=&_orig=search&_sort=d&_docanchor=&view=c&_searchStrId=961701155&_rerunOrigin=scholar.google&_acct=C000050221&_version=1&_urlVersion=0&_userid=10&md5=7ac35eaf65033607698819f1a9324706.

C John. The corono-apically varying ultrasonic velocity in human hard dental tissues. *The Journal of the Acoustical Society of America*, 116(1):545–556, July 2004. doi: 10.1121/1.1738454. URL http://link.aip.org/link/?JAS/116/545/1.

C John, K M Irion, W NÃ$\frac{1}{4}$ssle, and C LÃ¶st. [The resolution of a 2-dimensional ultrasonic velocity profile of human tooth sections]. *Schweizer Monatsschrift FÃ$\frac{1}{4}$r Zahnmedizin = Revue Mensuelle Suisse D'odonto-Stomatologie = Rivista Mensile Svizzera Di Odontologia E Stomatologia / SSO*, 104(1):25–30, 1994. ISSN 1011-4203. URL http://www.ncbi.nlm.nih.gov/pubmed/8108688. PMID: 8108688.

S Lees and F E Barber. Looking into teeth with ultrasound. *Science*, 161(3840):477–478, August 1968. doi: 10.1126/science.161.3840.477. URL http://www.sciencemag.org/cgi/content/abstract/161/3840/477.

C. Lost, K M Irion, C John, and W Nussle. Two-dimensional distribution of sound velocity in ground sections of dentin. *Dental Traumatology*, 8(5):215–218, 1992. doi: 10.1111/j.1600-9657.1992.tb00246.x. URL http://dx.doi.org/10.1111/j.1600-9657.1992.tb00246.x.

C. Louwerse, M. Kjaeldgaard, and M. C. D. N. J. M. Huysmans. The reproducibility of ultrasonic enamel thickness measurements: an in vitro study. *Journal of Dentistry*, 32(1):83–89, January 2004. doi:

10.1016/j.jdent.2003.08.007. URL http://www.sciencedirect.com/science?_ob=ArticleURL&_udi=B6T86-49PYNKC-1&_user=10&_rdoc=1&_fmt=&_orig=search&_sort=d&_docanchor=&view=c&_searchStrId=961699544&_rerunOrigin=google&_acct=C000050221&_version=1&_urlVersion=0&_userid=10&md5=46cd98c72b14c4c868a49cde18b5cf74.

G Ludwig and F Struthers. CONSIDERATIONS UNDERLYING THE USE OF ULTRASOUND TO DETECT GALLSTONES AND FOREIGN BODIES IN TISSUE, June 1949.

R.G. Maev, Y.M. Maximovksy, L.A. Denisova, Y.Y. Maeva, A.A Denisov, T.D Chirkova, and D.A Domyshev. Acoustic microscopy: a new method for investigation of dental tissues. *Stomaologiia*, 5:14–19, 2000. ISSN 0039-1735.

R.G. Maev, L A Denisova, E Y Maeva, and A A Denissov. New data on histology and physico-mechanical properties of human tooth tissue obtained with acoustic microscopy. *Ultrasound in Medicine & Biology*, 28(1):131–136, January 2002. ISSN 0301-5629. URL http://www.ncbi.nlm.nih.gov/pubmed/11879960. PMID: 11879960.

S Matalon, O Feuerstein, and I Kaffe. Diagnosis of approximal caries: bitewing radiology versus the ultrasound caries detector. an in vitro study. *Oral Surgery, Oral Medicine, Oral Pathology, Oral Radiology, and Endodontics*, 95 (5):626–631, May 2003. ISSN 1079-2104. doi: 10.1067/moe.2003.164. URL http://www.ncbi.nlm.nih.gov/pubmed/12738956. PMID: 12738956.

S Matalon, O Feuerstein, S Calderon, A Mittleman, and I Kaffe. Detection of cavitated carious lesions in approximal tooth surfaces by ultrasonic caries detector. *Oral Surgery, Oral Medicine, Oral Pathology, Oral Radiology, and Endodontology*, 103(1):109–113, January 2007. doi: 10.1016/j.tripleo.2006.07.023. URL http://www.sciencedirect.com/science?_ob=ArticleURL&_udi=

B6WP1-4M63RX5-7&_user=10&_rdoc=1&_fmt=&_orig=search&_sort=d&_docanchor=&view=c&_searchStrId=961205686&_rerunOrigin=scholar.google&_acct=C000050221&_version=1&_urlVersion=0&_userid=10&md5=f6b3c30cf057b35686ea2b57841f03db.

S Mezawa, T Kawato, K Yoshida, H Nozaki, T Saito, K Tamura, and M Onozawa. Evaluation of human tooth structure with the ultrasonic imaging technique. *Journal of Oral Science*, 41(4):191–197, December 1999. ISSN 1343-4934. URL http://www.ncbi.nlm.nih.gov/pubmed/10693297. PMID: 10693297.

S Y Ng, P A Payne, N A Cartledge, and M W Ferguson. Determination of ultrasonic velocity in human enamel and dentine. *Archives of Oral Biology*, 34(5):341–345, 1989. ISSN 0003-9969. URL http://www.ncbi.nlm.nih.gov/pubmed/2688612. PMID: 2688612.

S.Y. Ng, P.A. Payne, and M.W.J. Ferguson. Ultrasonic imaging of experimentally induced tooth decay. In *Acoustic Sensing and Imaging, 1993., International Conference on*, pages 82–86, 1993.

S.D. Peck, J.M. Rowe, and G.A.D. Briggs. Studies on sound and carious enamel with the quantitative acoustic microscope. *Journal of Dental Research*, 68(2): 107–112, February 1989. doi: 10.1177/00220345890680020201. URL http://jdr.sagepub.com/cgi/content/abstract/68/2/107.

D. A. Tagtekin, G Ozyoney, M Baseren, M Ando, O Hayran, R Alpar, S Gokalp, F. C Yanikoglu, and G .K Stookey. Caries detection with DIAGNOdent and ultrasound. *Oral Surgery, Oral Medicine, Oral Pathology, Oral Radiology, and Endodontics*, 106(5):729–735, November 2008. ISSN 1528-395X. doi: 10.1016/j.tripleo.2008.05.010. URL http://www.ncbi.nlm.nih.gov/pubmed/18656396. PMID: 18656396.

Zhizong Yang. Tooth enamel thickness measurement by ultrasound imaging

method. *The Journal of the Acoustical Society of America*, 100(4):2710, October 1996. URL `http://link.aip.org/link/?JAS/100/2710/4`.

F. Taliskan Yanikoglu, F. Ozturk, O. Hayran, M. Analoui, and G.K. Stookey. Detection of natural white spot caries lesions by an ultrasonic system. *Caries Research*, 34(3):225–232, 2000. ISSN 0008-6568. URL `http://www.karger.com/DOI/10.1159/000016595`.

Chapter 8

High frequency ultrasound and dental erosion

8.1 Introduction

As mentioned in Chapter 2, acid erosion is the irreversible loss of dental material due to acidic environments, and currently there are no quantitative methods for monitoring it. This is due to the lack of suitable reference points on the tooth surface. If one considers acid erosion as a simple layer thickness problem (progressive thinning of the enamel layer), then the possibilities of using ultrasound from its successes in the field of NDT are apparent.

This is because it allows the use of the enamel-dentine junction as a reference point. Ultrasound also has an advantage over the optical techniques discussed in the previous chapters, because, while having better axial resolutions, they are unable to image deep enough to be of use for quantitatively measuring enamel thickness.

In this chapter a 35 MHz focussed ultrasound transducer shall be utilised to produce a B-scan of a specially prepared dental sample in order that a number of thickness measurements be recorded. The sample is prepared in such a way that it exhibits an enamel layer that becomes progressively thinner along the scan line. It is designed in this way to simulate the progressive thinning of enamel through erosion. These measurements will then be compared against a gold standard technique from dentistry.

The transducer will then also be used to two imaging applications. Firstly, a three dimensional B-scan will be recorded to assess the performance of ultrasound for recording 3D representations of the tooth. And finally, the transducer will also be used to record a B-scan across a caries lesion in order to assess its suitability for this application.

8.2 High frequency transducer and advantages

The axial resolution of an ultrasound system increases proportionally with the centre frequency of the system if the relative bandwidth remains constant. Therefore, by using high frequency ultrasound transducers dental structures should be more clearly resolved. However, this comes at a cost of ultrasonic attenuation, which is also proportional to frequency. As mentioned in the previous chapter, the early dental ultrasound experiments were based on a 4 MHz transducer (Lees and Barber, 1968) while more recent published results have increased the operating frequency to between 10 and 15 MHz (Culjat et al., 2003; Ghorayeb and Valle, 2002; Huysmans and Thijssen, 2000).

The layer of incisor enamel is at most 1.5 mm thick and therefore it is possible to estimate the frequency required to observe a variation in thickness of 10%, for example during early decay or acid erosion. By taking the velocity of sound in enamel to be 6500 ms^{-1}(Ng et al., 1989), it can be calculated that such a variation requires a minimum frequency of around 22 MHz:

The transducer that is used for this study was measured to operate at a centre frequency of approximately 35 MHz.

By using a frequency of 35 MHz the axial resolution in enamel is around 180μm. This is a very significant improvement on previous work, in particular by Louwerse et al. (2004), who found that the limiting factor in their investigation was the 0.5 mm resolution of their system which operated at 15 MHz.

The transducer, shown in Figure 8.1, used for this investigation is a novel single element focused transducer with a centre frequency of 35 MHz as noted above, and a -6 dB bandwidth of 24 MHz (MacLennan et al., 2007). The transducer was manufactured with a 1-3 connectivity PZT piezoceramic - polymer composite (Button et al., 2005), the functional advantages of which are widely recognised (Abrar et al., 2004). The present device had a curved active face causing focusing without the need for a lens. The transducer was built into an SMA connector

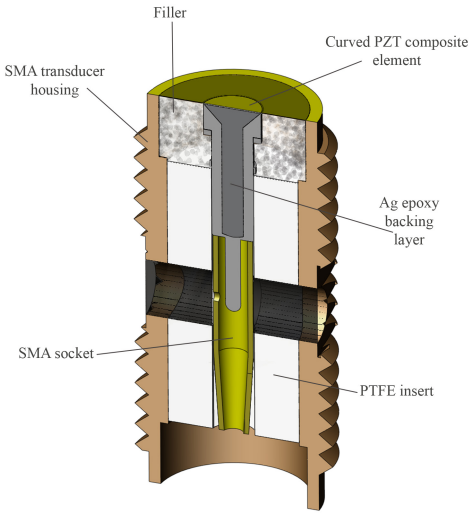

Figure 8.1: Diagram of high frequency focused transducer used in this investigation

and has an aperture diameter of around 1.6 mm.

Similar transducers are manufactured using PVDF but these tend to have low capacitance and are thus not well matched to conventional pre-amplifiers which have a high input capacitance, making the combination unsuitable for high frequency measurements (Cannata et al., 2006). Furthermore, PVDF has a very low thickness mode electromechanical coupling coefficient compared with piezo-composite and the transducer utilised here thus also has much higher sensitivity (MacLennan et al., 2007).

The transducer utilised here has a focal length of 6.5mm, with a theoretical focal spot size of 110μm in enamel. When considering that the dimensions of the microstructure of enamel are of the order of 4μm, it is assumed that this allows a high degree of localisation without distortion from scattering effects (John, 2006).

In the present investigation, the transducer was used to record a B-scan of an enamel sample in a pulse-echo configuration. This result was then compared with a series of x10 magnification images produced by a serial- grinding-imaging (SGI) technique (Longbottom, 2003).

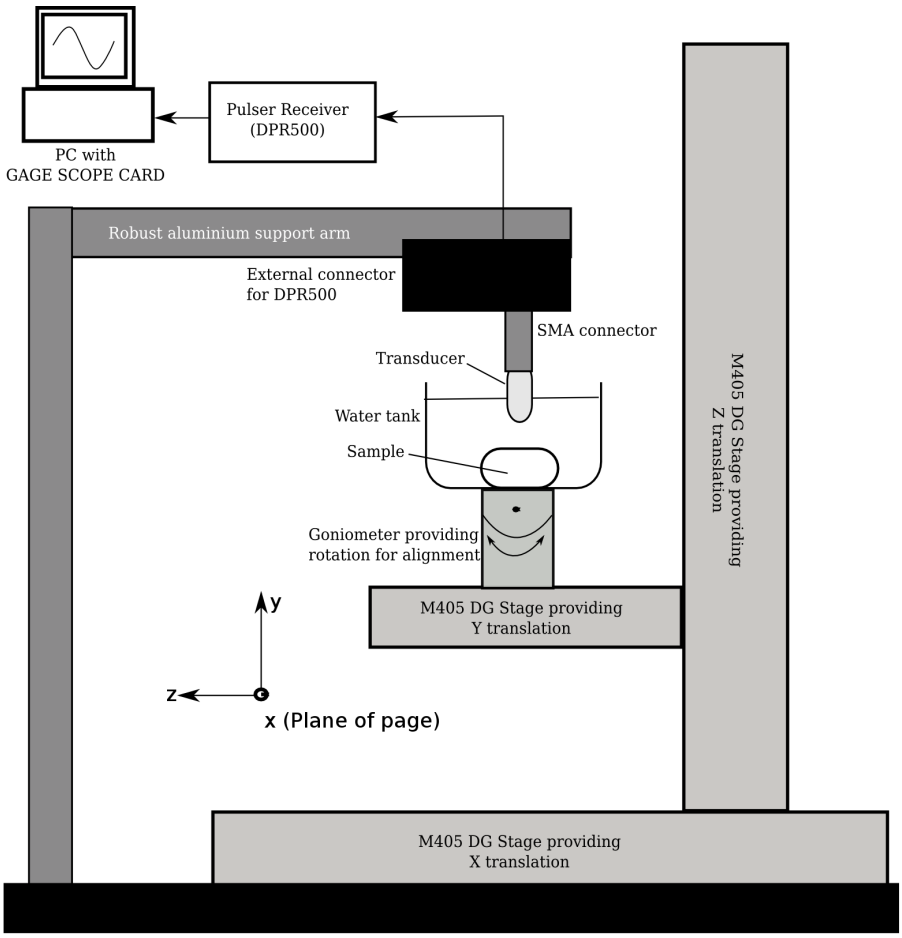

Figure 8.2: Schematic of high frequency ultrasound scan system

8.3 Experimental method

The dental sample was mounted on a two-dimensional goniometer to allow adjustment and optimisation of the angle of incidence of the ultrasound, as shown in Figure 8.2. The stage and sample were then placed in a water bath located on a one-dimensional translation stage. This allowed the sample to be moved along a line vector and a B-scan to be recorded by recording an A-scan at each position along the scan. The focused high-frequency transducer was attached to a rigid aluminium support and was adjusted in height so that the enamel surface lay within the focusing zone of the transducer.

The transducer was driven by a DPR500 pulser-receiver (JSR Ultrasonics, New York, USA) which provided a spike excitation of amplitude -210 V with

a +80 V overshoot before returning to zero. The pulser-receiver also provided a parallel damping resistor of 100Ω and a band pass filter with cut-off frequencies of 5 and 300 MHz. A PC controlled the translation stages (three orthogonally arranged M405-DG translation stages (Physik Instrument, Karlsruhe/Palmbach Germany) through a serial controller (C862.10, also by Physik Instrument). The PC also recorded the pulse-echo signal with a PC C8500 oscilloscope card (Gagescope, Lockport, USA) as shown in Figure 8.2.

The scanning system translation stage had a minimum programmable increment of 8.5 nm. However, the reproducibility in position was specified to be limited to 100 nm. Control of the system was achieved through a MATLAB script (The Mathworks Ltd, Cambridge, UK), with the translation stage moved in increments of 70μm, much larger than the positional reproducibility and more than satisfying the Nyquist spatial sampling limits for the transducer's lateral spatial resolution (Bushberg et al., 2003).

In order to verify the resolution and operating characteristics of the transducer, the scanning system was first used to produce a B-scan of a set of submerged tungsten wires, presented in Figure 8.3. These wires had a diameter of 5μm and were positioned so that each was at an increasing distance away from the transducer, starting at a distance less than the focal distance. The data was then processed so that it's intensity values were normalised to unsigned 8bit resolution (values of 0 to 255), and then displayed as pixel intensities. Figure 8.3 indicates that the transducer is functioning as expected, with an axial resolution of better than 100μm and a lateral resolution better than 250μm. For the dental investigation, the previously discussed complexities of the tooth were reduced by preparing an enamel sample which contained only one layer each of enamel and dentine as shown in Figure 8.4. The enamel layer was then polished and the sample was encased in epoxy, with an area of the enamel surface exposed as shown in Figure 8.4. This allowed easy mounting to the scanning system. The tooth, an

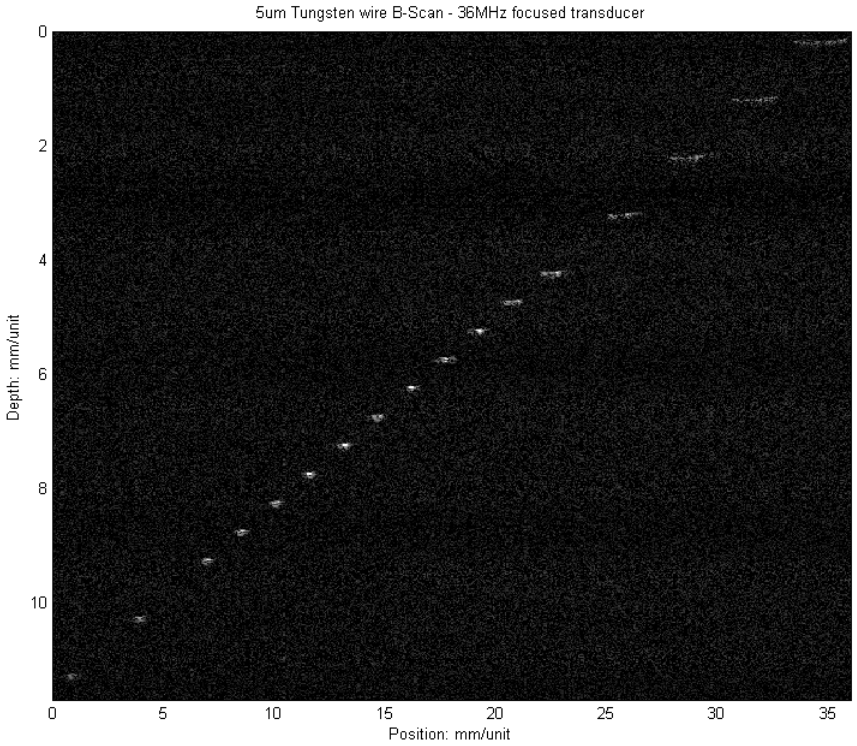

Figure 8.3: Tungsten wire scanning showing focussed ultrasound transducer performance

upper central incisor, had been collected (with the patient's consent) and stored in thymolised physiological saline solution.

3D Imaging

After a B-scan had been collected for the erosion measuring work, the scan system was then set to record multiple B-scans by also scanning in the orthogonal direction. This produced a three dimensional data set which was used in the imaging program ImageJ to produce a three-dimensional representation of the dental sample(Hughes et al., 2007).

The B-scans were recorded in the XY plane with a step size of 70μm, and adjacent B-scans recorded in steps of 70 μm. The total area scanned was 98 mm^2 (14 mm in the primary and 7 mm secondary scan direction)

After data collection, each B-scan was manually visually inspected firstly for the dental sample, and secondly for the EDJ. In each B-scan, the enamel surface was shaded in red, and the EDJ was shaded in blue. ImageJ then produced a rotating projection of the image data in RGB, showing the morphology of the enamel surface relative to the EDJ in the surrounding epoxy.

8.3.1 Signal processing

After the collection of the scan data, they were enhanced with signal processing algorithms implemented with the Scilab mathematical program (1989-2007. INRIA ENPC). The individual A-scans were first processed to remove noise by applying a high pass digital filter with a cut-off frequency of 5 MHz. Subsequently a moving average filter was applied,

$$y(i) = \frac{1}{M} \sum_{j=0}^{N-M} x(i+j) \tag{8.1}$$

For this, a value of M = 5 was chosen due to the high resolution requirement

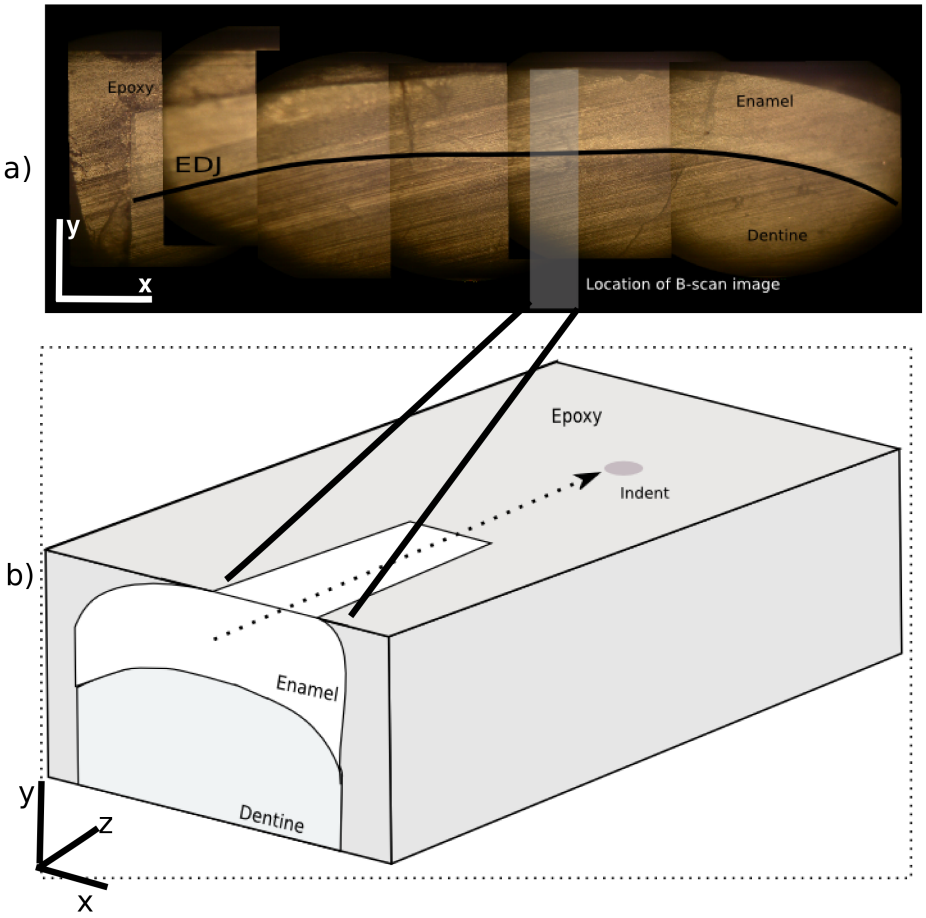

Figure 8.4: Composite photomicrograph of the dental sample showing enamel dentine junction end on (a) and the schematic of the dental sample (b). The dotted line in b) indicates the direction of the b-scan.

of the present work: if a higher value of M is chosen a larger temporal section of the A-scan is averaged which causes any oscillating signal present within the window defined by M to tend to zero. Large values of M are thus effective for slowly-varying signals where the period of the signal is greater than M. However, with high-frequency signals this is not the case.

The widths of individual peaks in the present scan data were measured to be around 20ns, corresponding to a frequency of 50 MHz and to M = 10 ($f_{sampling} = 500MHz$). Therefore, for the most suitable temporal resolution, M = 5 was chosen. This leads to a theoretical 40% reduction in the noise levels.

Trigger jitter and tilting of the flat enamel surface in the B-scan were corrected using an algorithm based on maximisation of correlation between neighbouring A-scans. This algorithm works by shifting an A-scan successively in time and calculating the correlation between the A-scan with that time shift and its neighbour. The A-scan is then permanently shifted to the position in which the highest correlation is recorded, and the process repeated until it has been applied to all the A-scans. This is a useful technique in that it allows easier analysis and comparison of the shape of underlying layers with a straight reference plane without affecting any underlying properties of the data.

8.3.2 B-scan and Water fall plots

In order to visualise the ultrasound data in two dimensions, two plots are used. The more common of these is the B-scan image, as shown in Figure 8.3. In this image, each column of pixels is an individual A-scan that has been rectified and plotted as a gray scale pixel intensity value.

A less common method of visualising the same data is the waterfall plot. In this type of plot, each A-scan is plotted as a line offset along the x-axis (or y-axis dependent on the orientation of the plot) with a value prescribed by the position of the transducer at the recording of the A-scan. Waterfall plots are

used because it is sometimes easier to pick out features that the human eye may miss with limited contrast in B-scan images. An example of a waterfall plot is shown in Figure 8.8 in the results section.

8.3.3 Sequential Grind and Image technique

The SGI technique (Longbottom 2003)â used for comparison with the ultrasound measurements involves placing the sample in a custom-made jig, photographing the 'face' of the sample with a digital camera (at x10 magnification) and subsequently grinding a specified thickness of material from the surface using a PM5 machine (Logitech, Glasgow, UK); the jig is then repositioned in the camera set-up and re-photographed and the sequence repeated until the sample is completely ground away. In the present study this provided a series of standardised photographs at 100 μm intervals through the sample. The cut face in this case was chosen to show the enamel and dentine thickness from the incisal end of the sample to the cervical end.

The images were analysed using software which allows the placing of a grid of known dimensions onto the individual images below the enamel/dentine, so that a trained operator can place measurement points on the outer surface of the enamel and the corresponding point, vertically in the image, on the EDJ at specific intervals laterally along the image of the sample. The software automatically computes the length of the straight line between the two points corresponding to the thickness of the enamel. Reproducibility studies were carried out to determine the extent of the errors involved in this technique.

The distance of the lateral edge of the sample from the edge of the resin block was known, as was the position and width of the scan beam in relation to the lateral edge of the sample. Hence the SGI measurements corresponding to the volume of the sample scanned with the ultrasound beam could be identified for comparison purposes.

8.3.4 Thickness from A-scan data

In order to measure the thickness of the enamel layer from the ultrasound measurements each A-scan was characterised separately. A simple approach is to use $v_{enamel}(t_{dentin} - t_{enamel})$, where $t_{dentine}$ and t_{enamel} are the times of arrival of reflections back at the transducer from the dentine and enamel respectively. However, a more accurate method is to use the transducer as a common frame of reference and calculate the distances from the transducer to both the enamel and dentine layers separately. The thickness of the enamel can then be calculated by the difference between these distances.

As expected, the pulse shapes recorded from the transducer were not ideal impulses, and therefore a decision was made to use the centre point of each pulse as the location of the boundary between two media. A spreadsheet was created which contained the values for the front face pulse start time, front face pulse end time, EDJ pulse start time, and EDJ pulse end time. A calculated column was then produced which held the time locations of centre points of the pulses. Each centre point time value was then converted to a distance in the transducer's frame of reference. The thickness of the enamel layer was then calculated to be the distance between the centres of the front face and EDJ pulse. The enamel layer was assumed to have a linearly decreasing thickness and therefore a linear trend line was fitted to the data, with this linear trend line compared to the SGI measurements. This approach was adopted due to the oversampling of the ultrasound spatial measurements and to reduce errors due to outliers in the ultrasound measurement data.

The comparison between the SGI and ultrasound measurements was performed using the open source R statistical programming language (http://www.r-project.org/). A Pearson pairwise correlation was calculated between the SGI and ultrasound trend line data points with 3 digits of precision.

8.3.5 Caries investigation methodology

In order to test the ultrasound transducer as a possible method of detecting dental caries, a series of B-scans was recorded in order to see if it was possible to observe a white spot lesion in an ultrasound image. As this investigation was carried out at a later date to the erosion data, the scan system, while the same in principle, had some altered components.

Namely, the stages had been replaced by Shot C-602 (Sigma-Koki) translation stages (providing 100μm reproducibility position), and the data acquisition was now handled by a USB oscilloscope (Picoscope, sampling at 2ns intervals). Due to these changes, the control software was re-written using Labview to make use of high speed USB data access.

The data output from the scan system was still stored in the same format as text files with comma separated values so that the original Scilab scripts were able to be used for subsequent data processing. This was limited to using the moving average filter as discussed before and a function for creating the water fall plots.

As shown in Figure 8.5a, the transducer was scanned linearly from the root to the crown to create b-scans of the tooth at different locations. Figure 8.5b presents a simplified map of where the three B-scans of this study were recorded from a molar exhibiting a white spot lesion which had been extracted for clinical reasons and stored in Thymol. Each B-scan was recorded over a distance of 4 cm, with a step size of 80μm. By including as much of the tooth as possible in the B-scan, it made the interpretation of the B-scan in relation to the actual tooth much easier. Each B-scan was thus composed of 500 A-scans.

Unprepared dental samples were used in order to keep the investigation as close to the real situation as possible. The tooth that was chosen had the lesion in a place such that there was sufficient flat enamel either side of the lesion that the lesion and the healthy enamel closely surrounding it would remain in focus

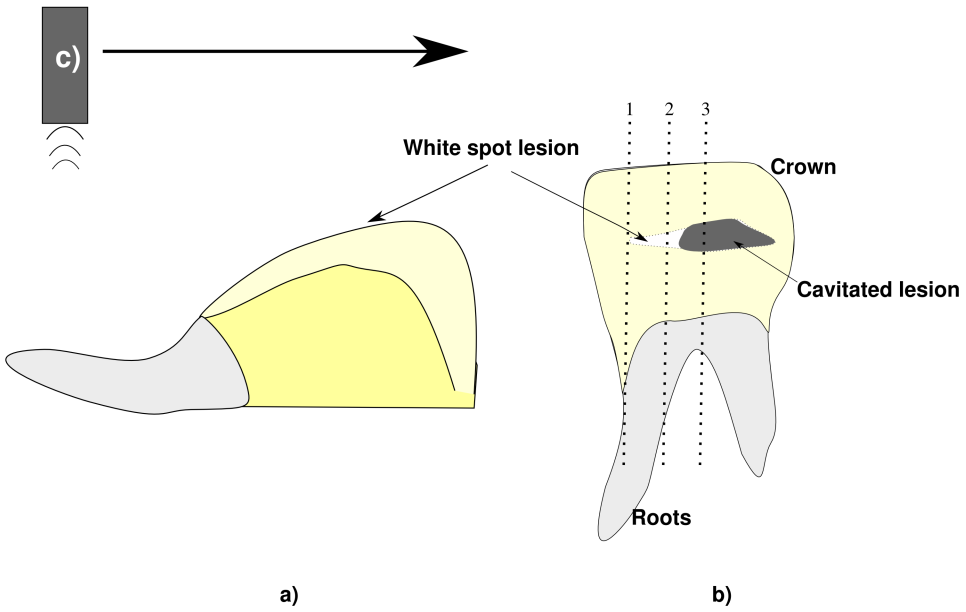

Figure 8.5: Schematic showing orientation of transducer to caries scan sample, and location of each b-scan (numbered 1,2,3).

during the scan.

8.4 Results and Discussion

To try and keep the discussion of the results in this chapter clear, this results and discussion section has been split up so that the enamel erosion data is discussed separately from the caries data. After this has taken place, the two sets of data shall be compared in a final conclusion section.

8.4.1 Enamel Thickness Results

Figure 8.6 shows a typical A-scan recorded for the enamel sample. The A-scan clearly shows the front face of the sample (FF), and also the enamel-dentine junction (EDJ). The time difference between these locations is 160 ns, which corresponds to a spatial distance of 0.52 mm, assuming a speed of sound of $6500 \mathrm{ms}^{1}$(Ng et al., 1989).

The output from the B-scanning, prior to processing, is presented in Figure

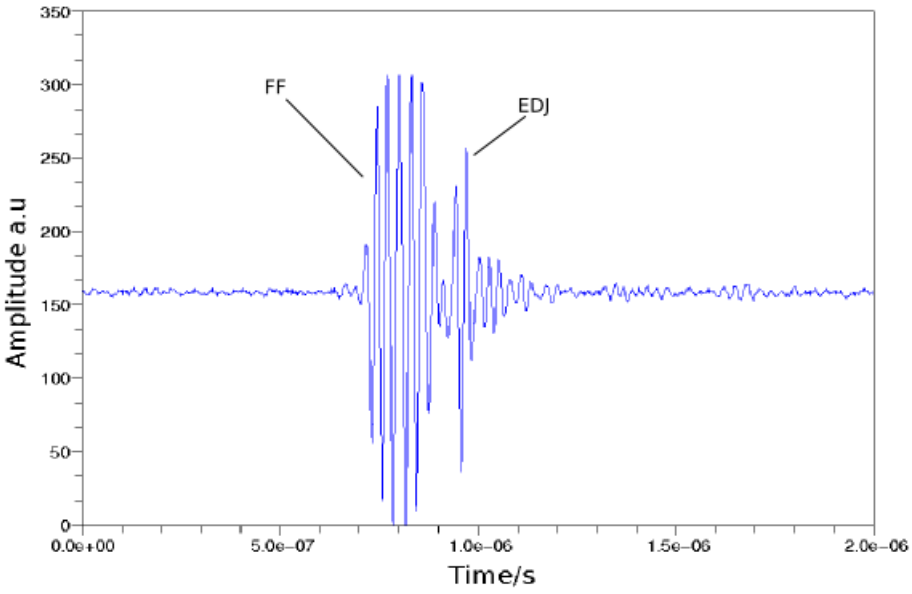

Figure 8.6: Ultrasonic A-scan of dental sample showing front face and enamel dentin junction (EDJ) reflections

8.7, with the processed image shown in Figure8.8. In order to aid understanding of the images, an annotated version of Figure 8.8 is given in Figure 8.9. The major improvement caused by the processing can be seen in the orientation of the imaged region in Figure 8.8, and also in the region between the FF and EDJ where the noise level has been much reduced. This makes it easier to observe the changing distance between the FF and EDJ, or in physical terms, the change in the thickness of the enamel layer.

It can be seen that the EDJ appears only around 2 mm into the waterfall plot shown in Figure 8.8. However, in Figure 8.4, the dentine layer is of the same length as the enamel. The discrepancy is believed to exist for two reasons, firstly the angular alignment of the transducer probe relative to the enamel sample and secondly the angular alignment of the dentine layer relative to the enamel layer. Both these effects cause problems with effective echogenicity and the return path of the ultrasound from the EDJ to the transducer. Therefore enamel thickness measurements can only be recorded from a distance of 0.5 mm inside the enamel

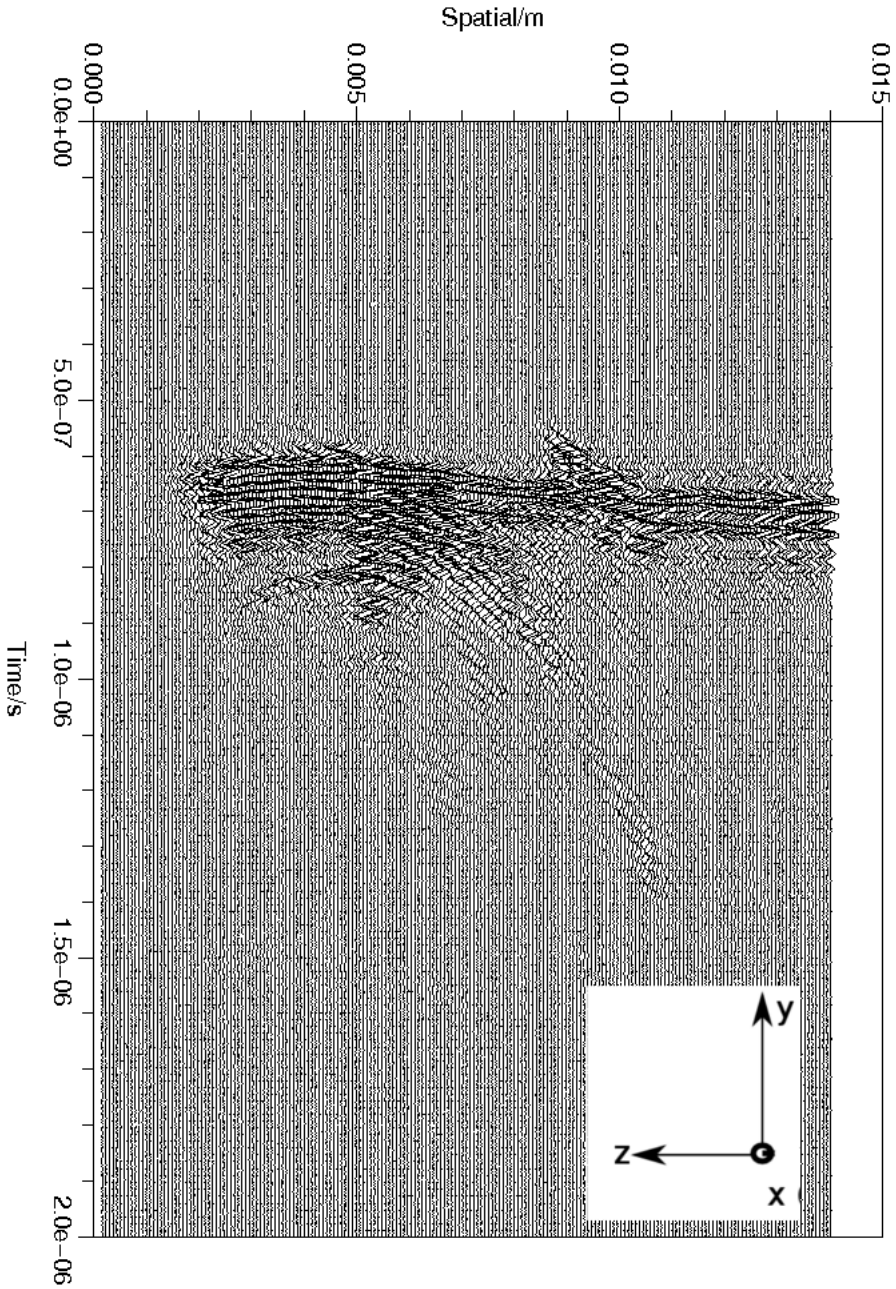

Figure 8.7: Raw data waterfall plot of dental erosion sample.

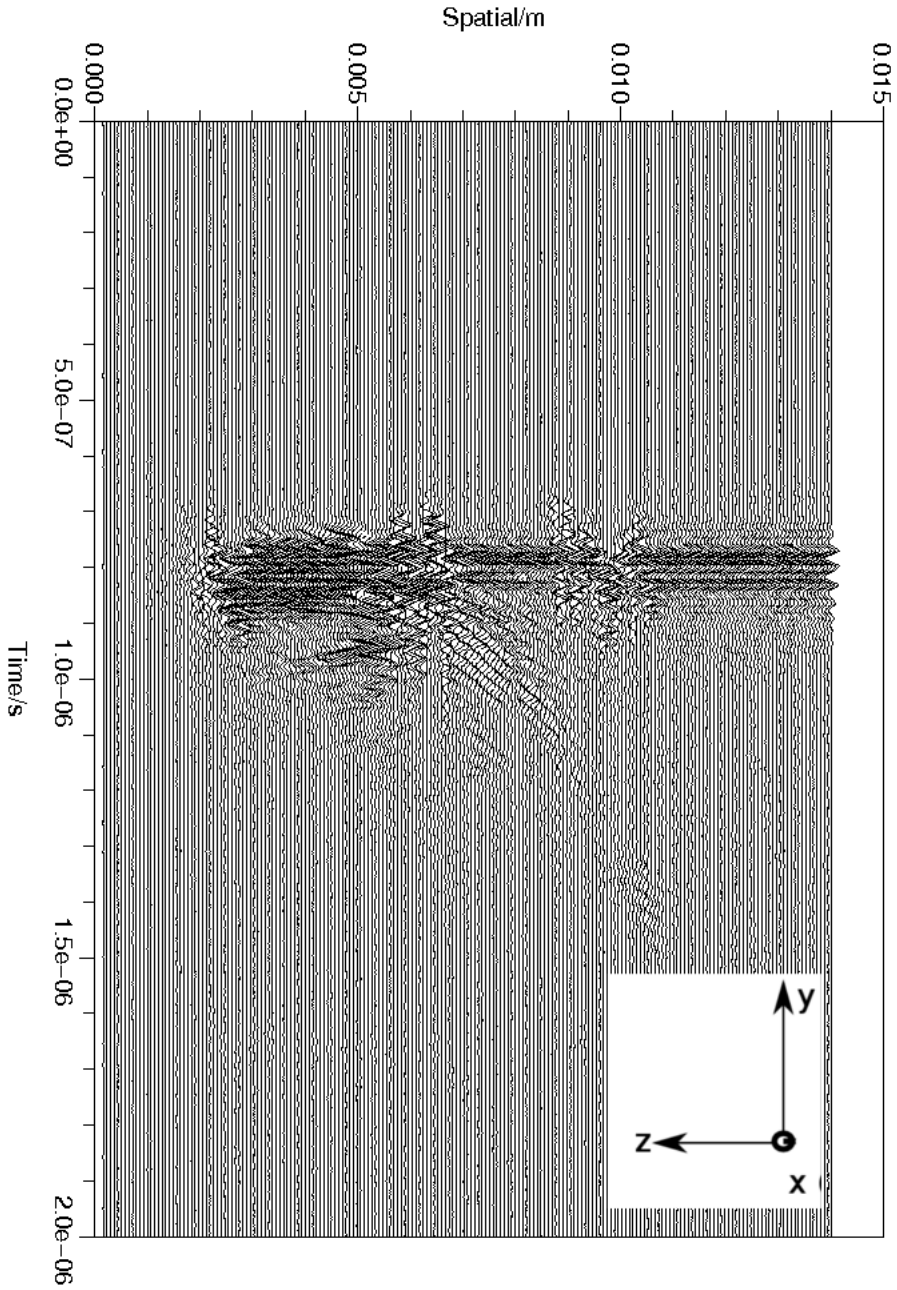

Figure 8.8: Waterfall plot of dental erosion sample after correlation shifting.

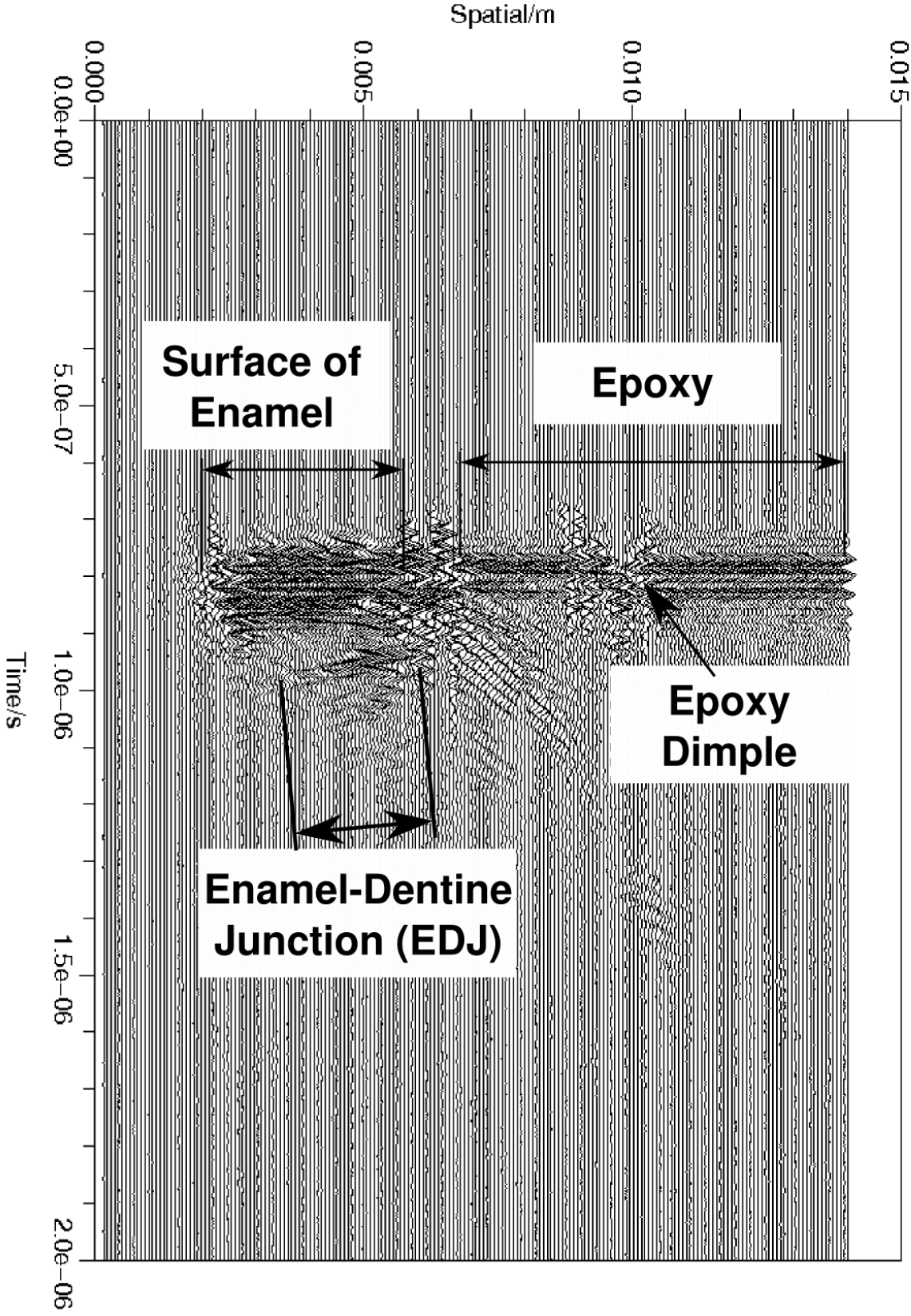

Figure 8.9: Annotated b-scan image of erosion sample.

surface along the B-scan vector.

From the results in Figure 8.10a, the enamel thickness can be seen to decrease along the B-scan vector. This observed decrease in enamel thickness is verified with the results of the SGI method (Pearson correlation value of 0.894 with confidence window of 1%) as shown in Figure 8.10b. The correlation plot is displayed as an inset in Figure 8.10b), indicating a positive correlation.

The error in the ultrasound measurements has been taken to be $\pm 90\mu$m on account of the uncertainty in the wavelength of sound in enamel. It has previously been reported in the literature that enamel is an anisotropic material (John, 2005) and therefore the velocity of sound in enamel is not constant (Maev et al., 2002; John, 2006; Ng et al., 1989). This could also explain the deviations from the trend line because a constant velocity of sound was assumed in this study.

The work carried out by Huysmans and Thijssen (2000) found a Pearson correlation value of 0.9 for enamel thickness measurements to a histological gold standard (Huysmans and Thijssen, 2000). While the histological method was similar to that presented here, with the samples sliced and then a microscope used to measure the thickness, the ultrasound setup was different. Huysmans and Thijssen used a commercially available industrial thickness gauge with a contact probe which is sold as a proprietary unit, compared to the system here which is a novel system using laboratory equipment.

Whereas in this study the SGI measurements were compared to the ultrasonic trend data, the previous work compared thickness measurements in the same area. The diameter of the active face of the contact probe, after the delay line, was reported to be 2 mm. When considering that the surface of a tooth is no more than approximately $2cm^2$, this appears to be large for this purpose. The system presented here used a focused ultrasonic beam which was incident on the enamel surface with a lateral resolution of 250μm. This will clearly allow a more localised thickness measurement to take place.

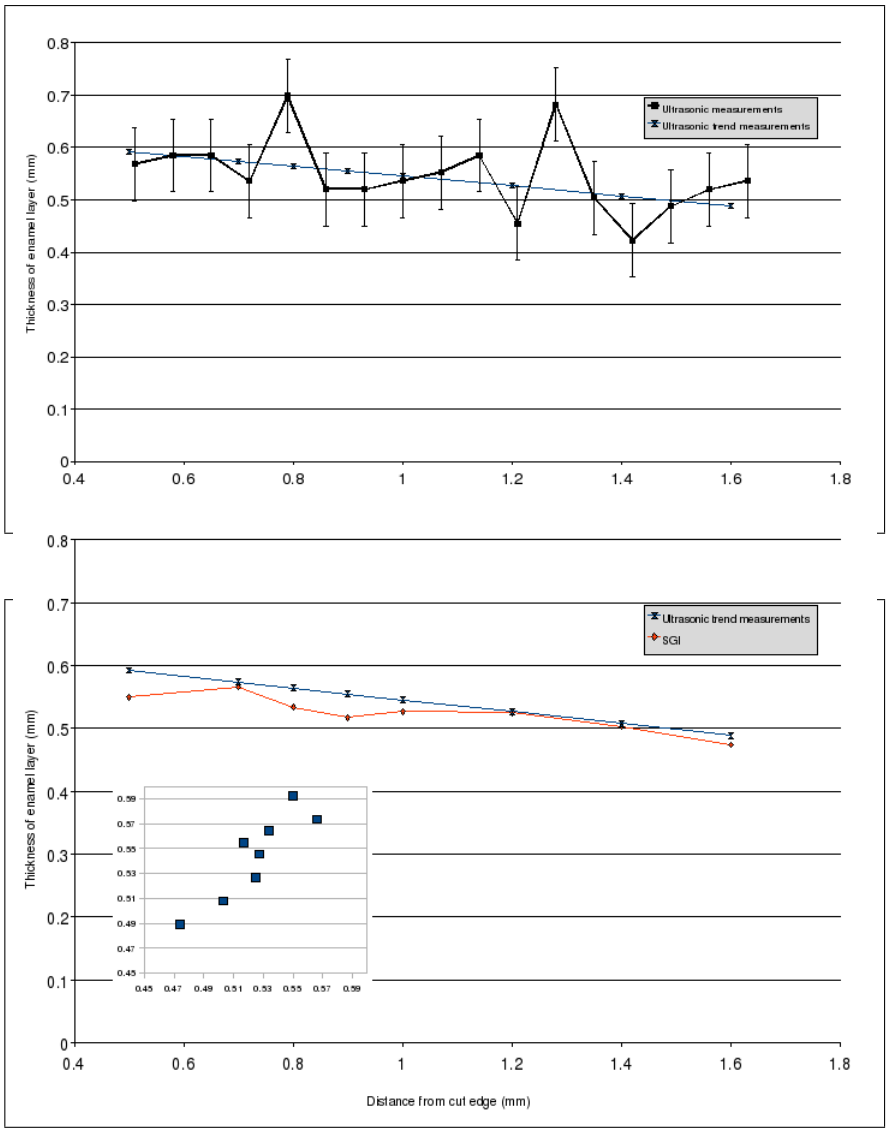

(b) Thickness measurements

Figure 8.10: Ultrasonic thickness measurements from b-scan data (a) and subsequent verification against the SGI method (b). Inset image in (b) shows the correlation relationship between the two techniques.

8.4.2 3D imaging results

Figure 8.11 shows a rendering of the three dimensional ultrasound scan of the dental sample. One can see the red enamel surface above the blue EDJ and the relative morphology. The rendering has been carried out using maximum projection algorithm and therefore the surrounding epoxy makes the image fairly noisy.

The data was collected using a sample scanning method, whereby the sample stage was moved for every data point. THis is a slow process that would have to be sped up if it were to be used in a dental clinic. Multiple element arrays as discussed in the previous chapter can allow imaging without sample scanning by scanning the beam instead. This is a direction that future improvements to the technique could take.

8.4.3 Caries results

Attention shall now be turned to the results of the investigation into using the same high frequency transducer to observe dental caries. Figures 8.12,8.13 and 8.14 presents the three grey scale B-scans that were recorded over three different locations on the tooth.

The resolution acheivable with the high frequency ultrasound is around 100μm and therefore it is thought that quantitative measurements (thickness and/or depth) of an early carious lesion is unobtainable. Therefore, the measurements presented here are given a qualitative analysis with a view to discussing indirect observations that may lead to a diagnosis of an early carious lesion.

The B-scan presented in Figure 8.12 is of an area of the tooth that had no caries visible on the surface. The crown of the tooth is to the right of the image, and it is at this level that the focus of the transducer was positioned. This means that there is a stronger return amplitude from this area in the B-scan image, and also appearance of the underlying enamel dentine junction (EDJ) in the pixel

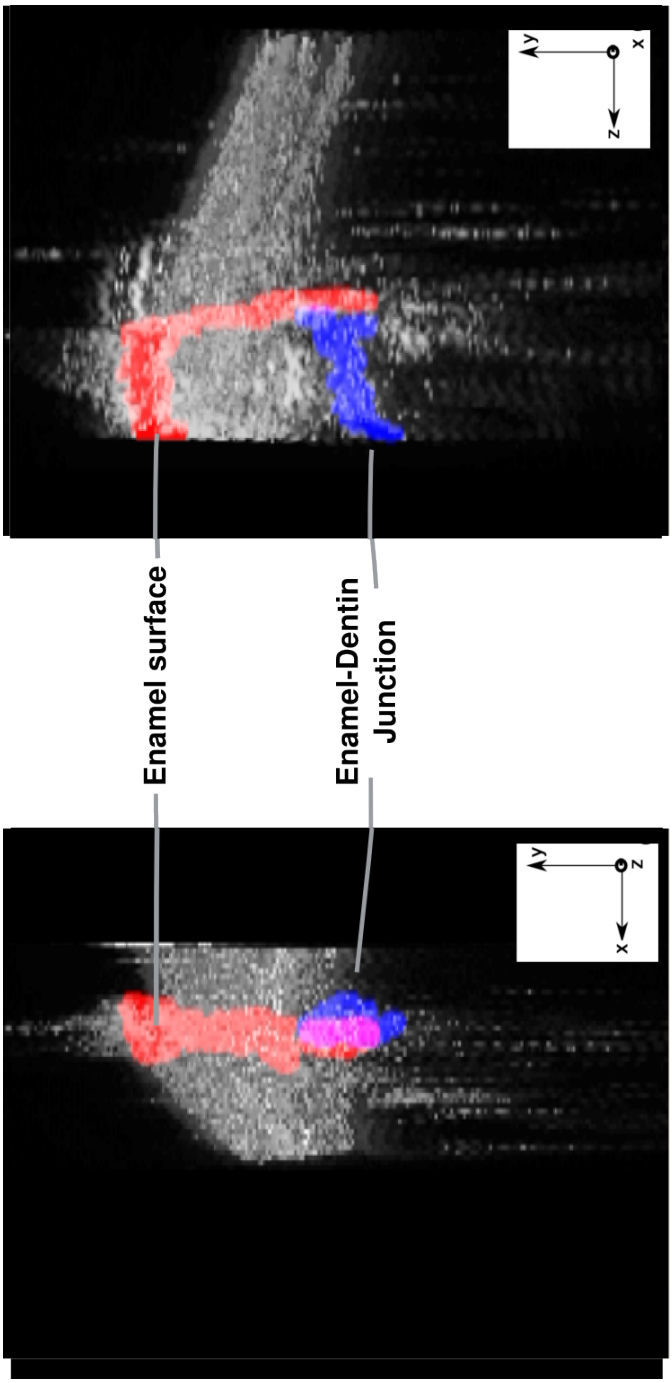

Figure 8.11: Three dimensional image of dental sample recorded using ultrasound. Image shows two views orthogonal to each other.

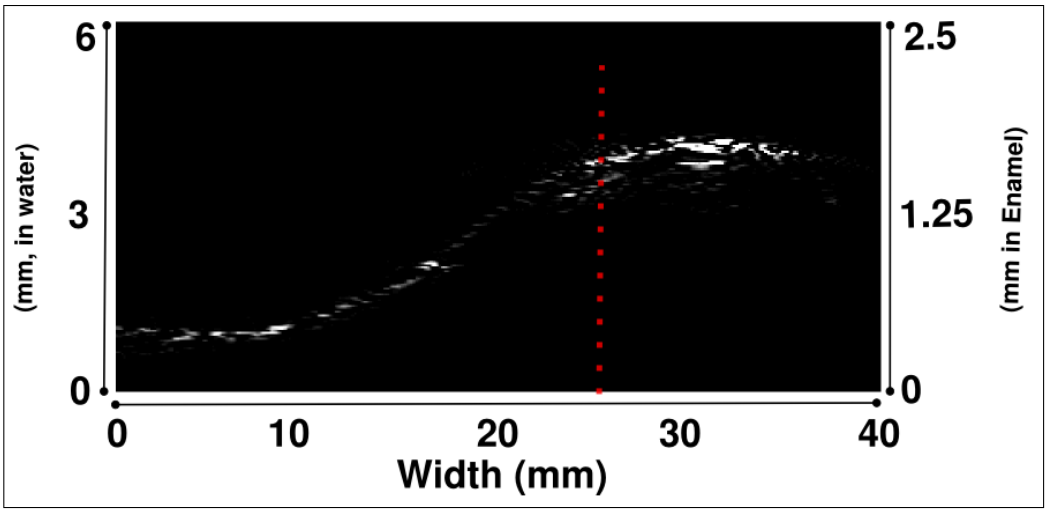

(a) Sound enamel b-scan

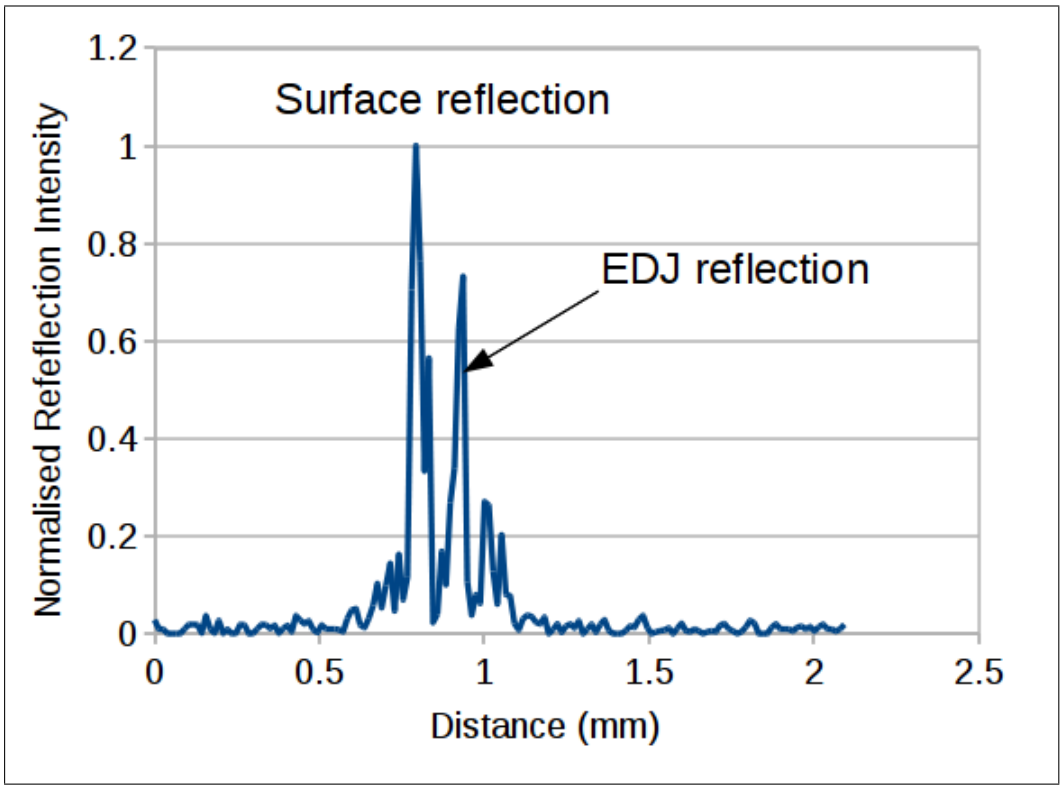

(b) Sound enamel intensity profile

Figure 8.12: Ultrasonic B-scan (a) recorded at location '1' of sample depicted in Figure 8.5. Red dotted line shows location of pixel intensity profile shown in (b)

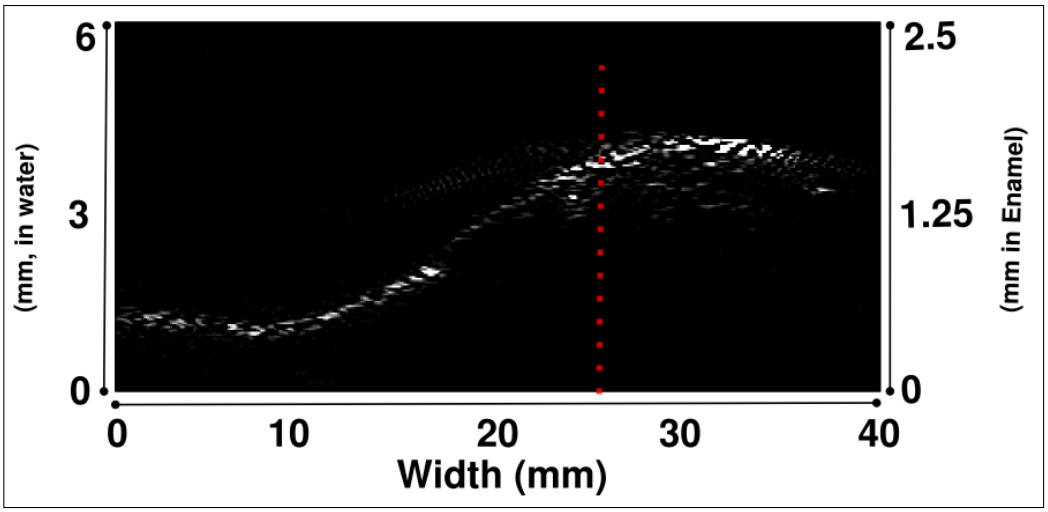

(a) Sound enamel b-scan

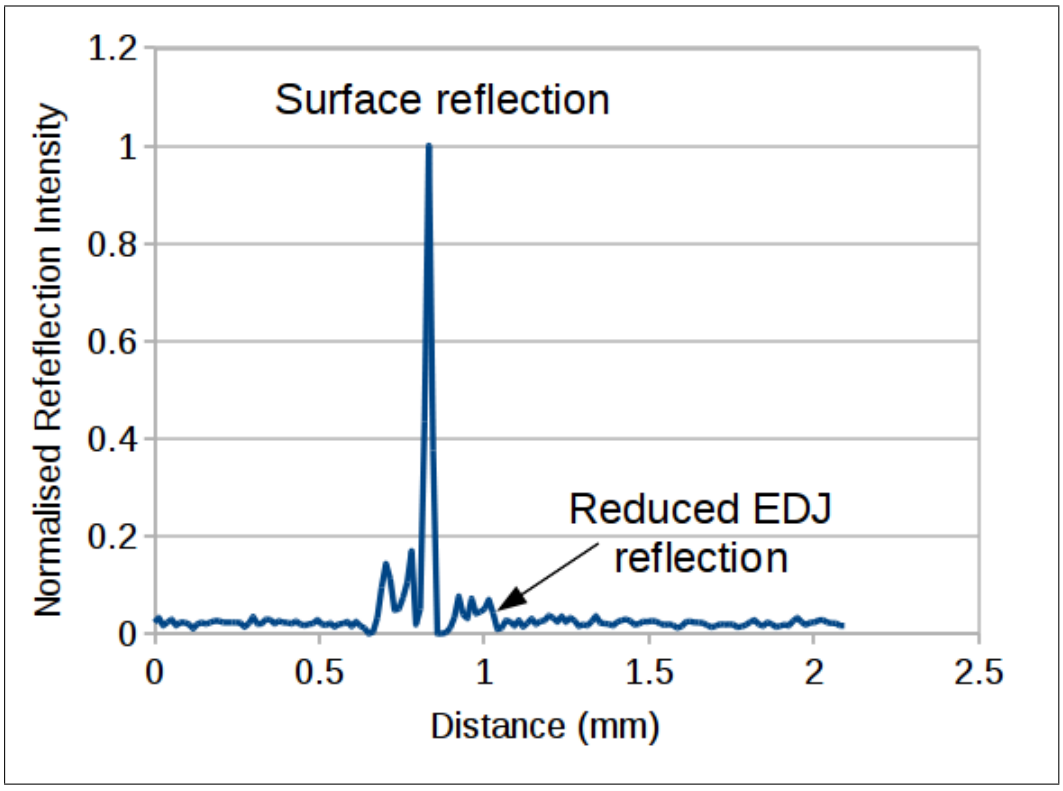

(b) Sound enamel intensity profile

Figure 8.13: Ultrasonic B-scan (a) recorded at location '2' of sample depicted in Figure 8.5. Red dotted line shows location of pixel intensity profile shown in (b)

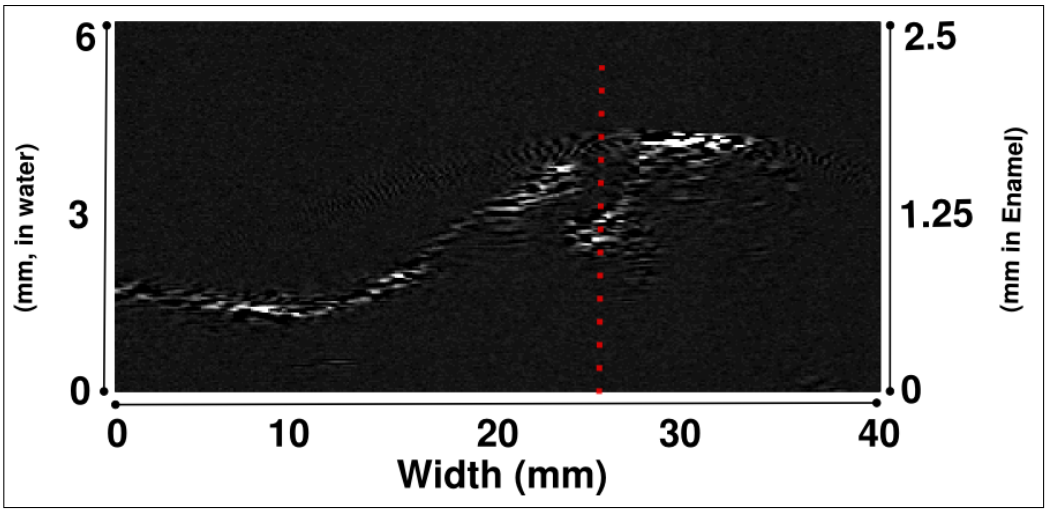

(a) Sound enamel b-scan

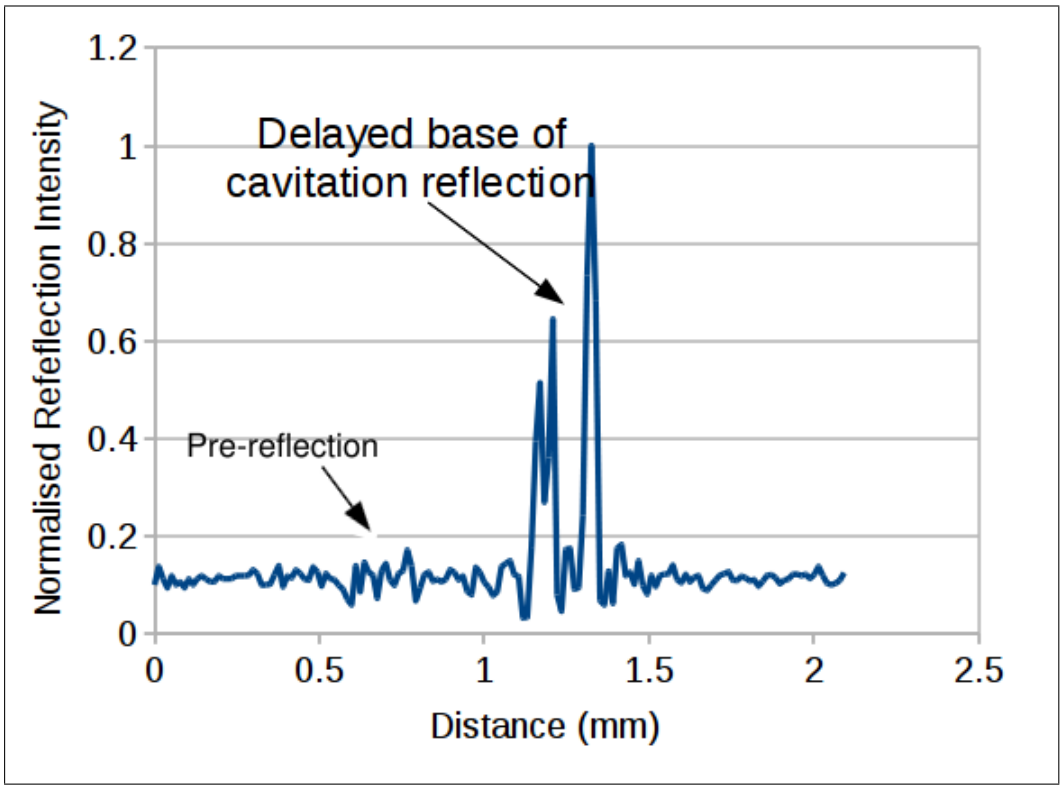

(b) Sound enamel intensity profile

Figure 8.14: Ultrasonic B-scan (a) recorded at location '3' of sample depicted in Figure 8.5. Red dotted line shows location of pixel intensity profile shown in (b)

intensity profile, Figure 8.12b.

Figure 8.13a shows a recorded B-scan from an enamel surface containing a section of white spot lesion. Again, the EDJ is visible in the pixel intensity profile of the B-scan, Figure 8.13b, but at a much reduced amplitude. The recorded signal from the surface containing the lesion is much more reduced in width than of the same area in Figure 8.12a; it is thought that this is due to the lesion causing a rough surface, which scatters the reflected ultrasound away from the detector. This is also the reason for the reduced signal from the EDJ in 8.13b. The resolution of the ultrasound system, as previously stated is too low to quantify the lesion, and therefore detection of early stage white spot lesions would rely on indirect observations such as these.

The reduction in amplitude shown in Figure 8.13b is thought to be due to the white spot lesion and not to the rotation of the surface because the area of enamel marked is of a similar tilt to that of the lesion and has a larger reflection amplitude. These images imply that an area of dental caries could be detected by imaging a suspected area and comparing it with the surrounding area for changes in reflected intensity profile for both the surface and the EDJ reflections.

It is possible to see some change in the reflected pulse from from the B-scan shown in Figure 8.13a, however, the resolution of the ultrasound (90μm at 35MHz) makes it difficult to give a quantified measurement of the thickness of the lesion at this point. Comparing this to the FOCOM system of earlier chapters, one can see appreciable differences in the techniques in terms of resolution and depth of view. The FOCOM technique was able to resolve features with a resolution of around 50μm, where as the ultrasound technique has a resolution of around 110μm. However, the FOCOM system had a much shorter field of view ($<$500μm) due scattering where as the ultrasound system is able to record structures at depths of over a millimetre.

In order to be sure of the location of the white spot lesion, a B-scan was

recorded that imaged the area of the white spot lesion at which the surface has been destroyed and a cavity had formed (as shown in Figure 8.14a). In this Figure, one can see the reflection from the base of the cavitation (which occurs at a later time to the surface reflections in Figures 8.12 and 8.13), and also the absence of a secondary EDJ peak. The reflection from the base of cavitation takes the form of a double peak. This is more clearly seen in the A-scan presented in Figure 8.14b than the b-scan because of the normalised contrast scale used in the b-scan. In the abscence of sectioning the sample to visually inspect the cavity, it can only be speculated at the source of this layered structure. It could be due to debri from the surface collapsing lying at the base of the cavity, or a subsurface fault. The depth of the cavity rules out this being the EDJ.

One can see from Figure 8.14b that the depth of the cavity is around 1mm, and by using Figure 8.12a, to see that the EDJ was located around 250μm below the surface of the enamel, one can assume that the small pre-reflection in 8.14b is an artifact of the scanning process where by the edges of the cavity are showing up in the A-scans. This occurs if the size of hte cavity is less than the ultrasound beam diameter.

8.5 Conclusions

The results presented in this chapter demonstrate ultrasonic thickness measurements of enamel via identification of the EDJ with an accuracy corresponding to within 50μm of SGI measurements on the same sample. This accuracy is approximately 10% of the enamel thickness in most cases. In comparison with current non-destructive methods of monitoring erosion, such as dental explorers, and X-ray radiographs, these results show promise for the use of ultrasound as an erosion monitoring technique.

Ultrasound has been shown to be a non-invasive method for observing the

internel structures of tooth. This chapter presented a simple three dimesional rendering of the enamel dentine junction under the enamel surface. From these results it can be concluded that by refining the technique, fractures and cracks in the EDJ could be visualised using ultrasound. However, issues such as speed of collection and signal to noise ratio have to be addressed before the technique could be used in the dental clinic.

The preliminary results for the caries lesion investigation also show promise, however, the main drawback to using a single element transducer for this purpose is the length of time it takes to produce a scan. This is because the transducer has to be manually moved in order to scan an area, which also raises problems in creating a miniature scan head suitable for the oral cavity.

With these limitations in mind, work is now under way to adapt research into high frequency ultrasonic arrays made from the same type of piezocomposite for dental applications. This will open up the opportunity to create an ultrasound probe that could image an area of the tooth around a suspect carious lesion, and without moving the probe allow comparison with the surrounding healthy enamel.

Bibliography

A. Abrar, D. Zhang, B. Su, T. W. Button, K. J. Kirk, and S. Cochran. 1â3 connectivity piezoelectric ceramicâpolymer composite transducers made with viscous polymer processing for high frequency ultrasound. *Ultrasonics*, 42(1-9):479–484, April 2004. doi: 10.1016/j.ultras.2004.02.008. URL `http://www.sciencedirect.com/science?_ob=ArticleURL&_udi=B6TW2-4BT1XX3-1&_user=10&_rdoc=1&_fmt=&_orig=search&_sort=d&_docanchor=&view=c&_acct=C000050221&_version=1&_urlVersion=0&_userid=10&md5=46e23af62f247d284521cdf2e4baa0a8`.

Jerrold T. Bushberg, J. Anthony Seibert, Jr. Leidholdt, John M. Boone, and Jr. Goldschmidt. The essential physics of medical imaging. *Medical Physics*, 30(7): 1936, July 2003. doi: 10.1118/1.1585033. URL `http://link.aip.org/link/?MPH/30/1936/1`.

T.W. Button, S. Cochran, K.J. Kirk, D. MacLennan, A. MacNeil, K. McDonald, C. Meggs, D. Rodriquez-Sanmartin, R. Webster, and D. Zhang. Net-shape ceramic manufacturing as an aid to realize ultrasonic transducers for high-resolution medical imaging. In *Ultrasonics Symposium, 2005 IEEE*, volume 3, pages 1625–1628, 2005. ISBN 1051-0117.

J.M. Cannata, J.A. Williams, Qifa Zhou, T.A. Ritter, and K.K. Shung. Development of a 35-MHz piezo-composite ultrasound array for medical imaging.

Ultrasonics, Ferroelectrics and Frequency Control, IEEE Transactions on, 53 (1):224–236, 2006. ISSN 0885-3010. doi: 10.1109/TUFFC.2006.1588408.

MO Culjat, RS Singh, DC Yoon, and ER Brown. Imaging of human tooth enamel using ultrasound. *Medical Imaging, IEEE Transactions on*, 22(4):526–529, 2003. ISSN 0278-0062. doi: 10.1109/TMI.2003.809141.

S.R. Ghorayeb and T. Valle. Experimental evaluation of human teeth using noninvasive ultrasound: echodentography. *Ultrasonics, Ferroelectrics and Frequency Control, IEEE Transactions on*, 49(10):1437–1443, 2002. ISSN 0885-3010. doi: 10.1109/TUFFC.2002.1041085.

D.A. Hughes, T.W. Button, S. Cochran, J. Elgoyhen, J.M. Girkin, H. Hughes, C. Longbottom, C. Meggs, and S. Poland. 5B-2 3D imaging of teeth using high frequency ultrasound. In *Proc. Ultrasonics Symposium, 2007, IEEE*, pages 327–330, 2007. ISBN 1051-0117. doi: 10.1109/ULTSYM.2007.92.

M. C. D. N. J. M. Huysmans and J. M. Thijssen. Ultrasonic measurement of enamel thickness: a tool for monitoring dental erosion? *Journal of Dentistry*, 28(3):187–191, March 2000. doi: 10.1016/S0300-5712(99)00063-9. URL `http://www.sciencedirect.com/science?_ob=ArticleURL&_udi=B6T86-3YF3VVT-4&_user=10&_rdoc=1&_fmt=&_orig=search&_sort=d&_docanchor=&view=c&_searchStrId=961701155&_rerunOrigin=scholar.google&_acct=C000050221&_version=1&_urlVersion=0&_userid=10&md5=7ac35eaf65033607698819f1a9324706`.

C. John. Directing ultrasound at the cemento-enamel junction (CEJ) of human teeth: I. asymmetry of ultrasonic path lengths. *Ultrasonics*, 43(6):467–479, May 2005. doi: 10.1016/j.ultras.2004.10.001. URL `http://www.sciencedirect.com/science?_ob=ArticleURL&_udi=B6TW2-4DM23RY-1&_user=10&_rdoc=1&_fmt=&_orig=search&_sort=d&_docanchor=&view=c&_searchStrId=`

961700928&_rerunOrigin=scholar.google&_acct=C000050221&_version=1&_urlVersion=0&_userid=10&md5=f79f775b92950fcd5f0f3ff1d817e9a0.

C John. Lateral distribution of ultrasound velocity in horizontal layers of human teeth. *The Journal of the Acoustical Society of America*, 119(2):1214–1226, February 2006. URL http://link.aip.org/link/?JAS/119/1214/1.

S Lees and F E Barber. Looking into teeth with ultrasound. *Science*, 161(3840): 477–478, August 1968. doi: 10.1126/science.161.3840.477. URL http://www.sciencemag.org/cgi/content/abstract/161/3840/477.

C Longbottom. ICDAS criteria: Application and validation. In *Early Detection of dental caries III*, University of Indiana, 2003.

D. MacLennan, J. Elgoyhen, T.W. Button, C.E.M. Demore, H. Hughes, C. Meggs, and S. Cochran. 2F-6 properties and Application-Oriented performance of high frequency piezocomposite ultrasonic transducers. In *Ultrasonics Symposium, 2007. IEEE*, pages 100–103, 2007. ISBN 1051-0117. doi: 10.1109/ULTSYM.2007.38.

R.G. Maev, L A Denisova, E Y Maeva, and A A Denissov. New data on histology and physico-mechanical properties of human tooth tissue obtained with acoustic microscopy. *Ultrasound in Medicine & Biology*, 28(1):131–136, January 2002. ISSN 0301-5629. URL http://www.ncbi.nlm.nih.gov/pubmed/11879960. PMID: 11879960.

S Y Ng, P A Payne, N A Cartledge, and M W Ferguson. Determination of ultrasonic velocity in human enamel and dentine. *Archives of Oral Biology*, 34(5):341–345, 1989. ISSN 0003-9969. URL http://www.ncbi.nlm.nih.gov/pubmed/2688612. PMID: 2688612.

Chapter 9

Conclusions and Further Work

The aim of this work was to investigate optical and ultrasonic methods for the detection of dental disease. In this chapter the various outcomes of the work shall be discussed, with an outlook to the further work that has emerged.

Before discussing the resarch outcomes, it is useful to compare the optical and ultrasound techniques against the hypothetical ideal device disccused in Chapter 2. This will help to gain a better feel for where the further work should lead from the current state of the art.

As mentioned in Chapter 2, the relative small size of the tooth gives rise to the need for high imaging resolutions for detecting disease. A value of around 50μm was given as being useful. The optical methods investigated in this work in their current forms have resolutions of around 50-60μm, and therefore are still lower than desired. However, it has been shown in Chapter 4 that the resolutions could be raised to more useful values with different setups. By incorporating a more complex lens system to the aspheric lens system, sub-10μm resolutions can be obtained allowing measurement and quantification of the early caries lesions.

At the current frequencies reported here, Ultrasound has an axial resolution limit of 180μm meaning that it is even more unsuitable for measuring the thickness of early caries lesions, however, as was shown, ultrasound can be used to detect caries lesions by looking at the reflection intensities rather than temporal information.

When considering the detection or diagnosis of dental erosion, the results presented in this thesis point towards ultrasound being more capable than the optical technique. This comes down to the issue of depth of field. The reference point used for measurement (Enamel Dentine Junction) can be several hundred microns up to a millimeter in depth. As shown in Chapter 4, as axial resolutions are increased with the optical systems, the focal length drops. This gives a limit on how deep (in the hypothetical absence of scattering) a device could scan. However, with scattering, the effective depth of field at the 808nm wavelength is

reduced to less than 200 μm.

However, ultrasound is very much capable of penetrating deep in to the tooth and, as shown in Chapter 8, the enamel dentine junction can be used as a source of temporal data for measurement.

Thus, it is the belief of the author that ultrasound is the prefered modality for diagnosing dental erosion, whereas the optical method is more suitable for dental caries.

Both techniques were designed with access to the oral cavity in mind. The optical system comprised of an aspheric lens handpeice with a diameter of 5mm, and the active unit of the ultrasound system was an SMA connector of less than a centimeter in diameter. However, when it comes to maneuverability the optical technique is possibly more useful. This is because it is easier to 'bend' a light beam by way of mirrors, than it is an ultrasound wave. Therefore, for measuring teeth at the rear of the mouth, it would be easier to envisage an optical handpeice.

Both techniques are standalone in that they only use their own sources and the intrinsic properties of the tooth to make a measurement. In the case of the optical method, the source being the 808nm laser and intrinsic properties being the ordered (and in case of lesions, unordered) tubular structure of enamel and dentine for scattering. With ultrasound, the active face of the transducer produces the high frequency ultrasound which interacts with the sold enamel and dentine material.

From the point of view of patient comfort, this is helpful because there is no pre-treatment neccessary to make a measurement (which reduces in clinic time, especially of concern for more nervous patients).

It can be assumed that the majority of end-users (the dental clinicians) for either technique will not have expert knowledge of interpretting FOCOM or Ultrasound A-scans. Therefore, principle component analysis was introduced as a method of teaching the computer to interpret FOCOM a-scans in order to make

a diagnosis. The end-user would not have to have knowledge of principle component, as it would be intended to use the technique as a 'black-box' unit which takes the scan and presents a user-friendly interface on the computer.

In terms of the erosion data, ultrasonic thickness gauges are commerically available for material characerisation. It is therefore not difficult to imagine a high frequency ultrasonic thickness gauge set-up for measuring the thickness of the enamel layer. Such a device would present the clinican with a quantified value which would be used to monitor the erosion over time. As a further extension of this, a PCA algorithm could be included to characterise the reflection signal as a way of diagnosing dental caries.

9.1 Research Outcomes

1. Computer simulation into the propagation of rays through GRIN lenses, showing the dependence of fibre grin spacing on resolution for a confocal application. Ultimately, the outcome of this part of the investigation showed that while GRIN lenses could be used for confocal applications, the resolution that was obtainable (50μm) was not sufficiently high for the dental application. It was thus shown that aspheric lenses would be more suitable for this application due to their hypothetical higher resolution (20μm) and the ability of incorporating an optical chopper for imcreasing the signal to noise ratio.

2. Principal component analysis is a method of clustering one dimensional fibre optic confocal microscope (FOCOM) scan data dependent on features. While the use of principal component analysis is widespread, this work presented its first use with FOCOM data. By using principal component analysis, it is possible to allow a computer to 'recognise' forms of FOCOM data which has applications where it is required that there is a reduced

emphasis on the user to interpret the recorded raw data.

3. The development of a fibre optic confocal microscope system utilising miniature lenses for the detection of dental caries (Hughes et al., 2009c). The combination of the FOCOM system and principal component analysis has given rise to a miniature optic system which can distinguish between areas of sound enamel and areas of lesioned enamel with sensitivity of 0.96 and specificity of 0.9.

4. This work also demonstrated a novel high frequency focussed ultrasound transducer as being suitable for measuring the thickness of the enamel layer to within 10% of the total enamel layer thickness, with applications in monitoring dental erosion (Hughes et al., 2009a). The technique was similar in resolution to scanning acoustic microscopy, but had the advantage in that no surface preparation was required.

5. The transducer was used to create, while crude, the first three dimensional ultrasound images of the internal structures of the tooth (Hughes et al., 2007).

6. Furthermore, the same high frequency ultrasound probe has been shown to be useful for the imaging of caries lesions (Hughes et al., 2009b). Comparison of the reflected signals from areas of sound enamel to that with a white spot lesion, differences in the shape and amplitude of the returned surface and EDJ reflections allow discrimination between healthy and diseased tissue.

9.2 Further developments

1. One of the main aims of this work from the start was to produce a fibre optic confocal microscope for use inside the oral cavity. While this work

has shown that it is possible to use a FOCOM system that incorporates miniature aspheric lenses for the detection of lesioned surfaces, the axial scanning motion is provided by a bulky piezoelectric stage.

Work was carried out into using a miniature stage (PI-635, Physike Instruments) that was intended for mobile phone camera autofocus applications. The small size and DC powered nature of the stage made it very attractive for this application.

A prototype hand-held FOCOM system was built, but it was found that the translation stage suffered from a number of problems. The major issue was that the motion suffered from a lot of jitter, and this meant that depth profiles were inaccurate. The translation stage also had no method of recording the position of the stage at a certain time, and therefore with the jitter problem, this lead to poor reproducibility of scans.

If these problems were overcome, using the same translation stage or using another scanning method (such as fibre scanning), then it is the authors belief that a commercially viable FOCOM system could be realised.

2. The ultrasonic portion of this body of work was carried out over a shorter length of time in comparison to the FOCOM work, and therefore there are many directions to progress with the work. The main focus of the future work is into array transducers made from the same material as the transducer used in this study. With these arrays, it is hoped that a system can be built that can produce B-scan images of a tooth without the need for moving the sample or transducer (as shown in conventional imaging with arrays).

   The current state of the art transducers from the group operate at around 50 MHz, which would result in higher resolution thickness measurements (65μm). Such a transducer would be able to record more high quality three

dimensional images than those previously reported by this group (D.A. Hughes et al. 2007)â , without the need for moving the transducer.

3. As well as producing three dimensional B-scan images with the array technology, the early results shown in this thesis into using the transducer to image caries lesion provides another application. While the resolution would still not be high enough to quantitatively measure the thickness of an early caries lesion, the acoustic impedance mismatch of healthy and lesioned enamel would allow detection to take place.

4. Ultimately, one of the main issues that needs to be resolved before ultrasound can be a clinical diagnostic tool is one of coupling. In all the experimental work reported in this thesis, water was used as the coupling medium. While water is a non-toxic and conformable material for this purpose, there are issues with how one might apply it in a clinical environment. A strong contender for this application may be the use of gel pads which could interface the transducer to the tooth.

Bibliography

D.A. Hughes, T.W. Button, S. Cochran, J. Elgoyhen, J.M. Girkin, H. Hughes, C. Longbottom, C. Meggs, and S. Poland. 5B-2 3D imaging of teeth using high frequency ultrasound. In *Proc. Ultrasonics Symposium, 2007, IEEE*, pages 327–330, 2007. ISBN 1051-0117. doi: 10.1109/ULTSYM.2007.92.

D.A. Hughes, J.M. Girkin, S. Poland, C. Longbottom, T.W. Button, J. Elgoyhen, H. Hughes, C. Meggs, and S. Cochran. Investigation of dental samples using a 35 MHz focussed ultrasound piezocomposite transducer. *Ultrasonics*, 49:212–219, 2009a. doi: 10.1016/j.ultras.2008.08.007. URL `http://www.sciencedirect.com/science/article/B6TW2-4TDC09Y-1/2/b73067076490f6f8bef656d61e53de3e`.

D.A. Hughes, C Longbottom, S. Cochran, and J. M. Girkin. Focussed ultrasound for early detection of tooth decay. In *(Accepted) Proc. Ultrasonics Symposium, 2009, IEEE*, 2009b.

D.A. Hughes, S P Poland, S. Cochran, C Longbottom, and J. M. Girkin. A fibre optic system for the detection of dental caries. In *Journal of Medical Devices*, volume 3, Minneapolis, 2009c.

Chapter 10

Appendix 1: GRIN simulation C code

```
#include <iostream>
#include <fstream>

#include <cmath>

using namespace std;

float g=.327; // gradient constant mm-2
float L; //length of GRIN mm
float n0=1.592; // refractive index at optic axis
float dz; // z step increments
float constant; // for quicker calculation

float n2x(float x)
{
//square of refractive index at point x away from optic axis

        float nx;
        nx=n0*(1-((pow(x,2)*g)/(2)));
        //cout<<nx<<"\n";

return pow(nx,2);
};



float D(float x)
{
  float result;
  result=constant*((pow(x,3)*pow(g,2))-2*x*g);

return result;
};
```

```
int main()
{
        int i,totalEntries,ray;
        float A,B,C,rootg,fp,ray1;
        float x0,t0,x,t,xn1,tn1;
        float FGD,NA_fibre;
        float exitAngle;
        char *filename = new char[30];

        float *rayData;

        cout<<"------------------------------\n-- GRIN lens ray path --\n";
        cout<<"-- David Hughes, 2008 --\n----------------------------\n\n";
        cout<<"Gradient index constant (A) : ";
        cin>>rootg;
        g=rootg*rootg;
        cout<<"Refractive index at optical axis, n0 : ";
        n0=1.592;
        cout<<"Length of Grin Lens : ";
        cin>>L;
        cout<<"z step increments : ";
        dz=0.05; // z step increments
        cout<<"------------------------------\n";
        cout<<"Filename :";
        cin>>filename;
        cout<<"Constant :"<<constant;
        cout<<"\nFGD:";
        cin>>FGD;

        NA_fibre=0.13;
        t0=asin(NA_fibre);

        totalEntries=(int)((FGD+L)/dz);

        rayData = new float [5*totalEntries];

        fstream f;
        f.open(filename,ios::out);
        for(ray=1; ray<=5; ray++)
        {
                x=0;
                x0=0;
                t0=ray*(asin(NA_fibre)/5);
                constant =pow(n0,2)/(2.0*n2x(x0)*pow(cos(t0),2));
                for(i=0; i<(FGD/dz); i++)
                        {
                                x=(i*dz)*sin(t0);
                                //f<<(dz*i)<<" "<<x<<" "<<t0<<"\n";
                                rayData[((ray-1)*totalEntries)+i]=x;
                                x0=x;
                        };

                t0=asin(sin(t0)/sqrt(n2x(x0)));

                x=x0;
                t=t0;
```

```
                for (i=0; i<(L/dz); i++)
                {
                        rayData[((ray-1)*totalEntries)+(i+(int)(FGD/dz))]=x;
                        A=dz*D(x);
                        B=dz*D(x+((dz/2.0)*t)+((1.0/8.0)*dz*A));
                        C=dz*D(x+(dz*t)+((1.0/2.0)*dz*B));

                        xn1=x+dz*(t+(1.0/6.0)*(A+2.0*B));
                        tn1=t+(1.0/6.0)*(A+(4.0*B)+C);
                        x=xn1;
                        t=tn1;
                xn1=0;
                tn1=0;


                };


                exitAngle=asin(sqrt(n2x(x))*sin(t));
                cout<<"Ray "<<ray<<" final angle is ";
                cout<<t<<" at position "<<x<<", Exit Angle is ";
                cout<<exitAngle<<". Focal Point is "<<x/tan(abs(exitAngle))<<"\n";
                if (ray==1) ray1=x/tan(abs(exitAngle));
                if(ray==3) fp=x/tan(abs(exitAngle));
        };
        cout<<"focal length: "<<fp<<", spread :"<<ray1-(x/tan(abs(exitAngle)))<<"/n";
        for(i=0; i<totalEntries; i++)
        {
                f<<i*dz<<" "<<rayData[i];
                f<<" "<<rayData[i+totalEntries];
                f<<" "<<rayData[i+2*totalEntries];
                f<<" "<<rayData[i+3*totalEntries];
;               f<<" "<<rayData[i+4*totalEntries]<<"\n";
        };
f.close();
return 0;
};
```

List of Figures

2.1 The tooth and its constituent materials 11

2.2 The dental caries cycle 15

2.3 Prevalence of dental erosion in previous years 27

3.1 Electromagnetic field propagating through time with perpendicular electric and magnetic fields 36

3.2 Optical interactions with matter. a) Transmission, b) Reflection, c) Scattering with transmission, d) Scattering with backscattering, e) Absorption, f) Fluorescence with transmission and g) Fluoresence with backscattering 38

3.3 Incident light being scattered through a section of healthy dentine (a) and diseased dentine (b) 42

3.4 Schematic of an OCT system 43

3.5 Image enlargement with a magnifying glass 49

3.6 Reduced diagram of magnifying glass showing angles of interest. . 50

3.7 Spherical aberations, with centre of confusion labeled C 51

3.8 Ray diagram of compound microscope 52

3.9 An airy disc, produced in ImageJ by performing an FFT on a circular aperture 53

3.10 Numerical aperture of an objective lens 54

3.11 Signal collection in conventional micorscope. 56

3.12 Signal detection in confocal microscope showing rejection of out of focus light. 58
3.13 Exaggerated diagram showing lateral (a) and axial resolution (b) for a Gaussian beam profile 59
3.14 A single mode optical fibre acting as pinhole in FOCOM. 63
3.15 Schematic of a FOCOM system showing the separation of the laser optics and the confocal hand piece 64
3.16 A single mode fibre acting as a pinhole can give either a) a lens or b) fibre dominated system 64
3.17 Basic desktop FOCOM setup as demonstrated in Rouseau et all (2007) 66

4.1 Focusing with a traditional lens 75
4.2 The curvature of a traditional (a) lens compared to that of an aspheric (b) lens 76
4.3 Diagram explaining the property of pitch for GRIN lenses 79
4.4 GRIN lens material with a pitch of 0.29 80
4.5 Diagram showing the relationship between ds, dz and and angle gamma 83
4.6 Simulation of single mode fibre through GRIN material 86
4.7 FOCOM system with GRIN lens objective 87
4.8 Glass holder for GRIN lens mounted on single mode fibre cladding. 88
4.9 Desktop FOCOM system with aspheric lens. 89
4.10 Simulated ray path of light through GRIN media 90
4.11 Simulated parameters of GRIN lens with varying distance between fibre and GRIN lens. 92
4.12 Simulated effect on parameters of GRIN lens with varying radial profile. 93
4.13 Effect of varying g on ray path through GRIN lens 94

4.14 Experimental results of testing the GRIN lens. 95
4.15 Experimental characterisation of aspheric lenses. 96

5.1 Decomposition of two shapes (a and b) into multiples of stars, circles and squares. 105
5.2 Formation of data matrix, A, from one dimensional FOCOM data 108
5.3 Ultrasound set-up to collect B-scan image of steel block underwater with bubbles on surface. 115
5.4 B-scan showing Steel block submerged in water with bubbles showing. 116
5.5 Choice ultrasonic A-scan's from steel block experiment 117
5.6 First six derived principle components from ultrasonic dataset. . . 118
5.7 Cumulative energy of principal components from Steel block data set. 119
5.8 First and second principal component weightings for steel block experiment, showing segmentation of A-scans 120

6.1 Desktop FOCOM system with aspheric lenses for scanning dental samples. 130
6.2 Typical dental sample scans from the FOCOM system. 133
6.3 Distribution of weights of principle components from FOCOM data.134
6.4 Magnitude of weighting of third principle component in FOCOM scan data 135
6.5 Distribution of scan morphology around PCA space. 138

7.1 Longitudinal pressure wave in a material 146
7.2 Axial resolution of an ultrasound transducer, adapted from Cobbold (2007) 149
7.3 Focussing of an ultrasound beam using a) curved active face and b) by using a multiÂelement array 152

7.4 Modes of operation of an ultrasound system, a) pulse-echo and b) through-transmission 154

8.1 Diagram of high frequency focused transducer used in this investigation 175
8.2 Schematic of high frequency ultrasound scan system 176
8.3 Tungsten wire scanning showing focussed ultrasound transducer performance 178
8.4 Composite photomicrograph of the dental sample showing enamel dentine junction end on (a) and the schematic of the dental sample (b). The dotted line in b) indicates the direction of the b-scan. . . 180
8.5 Schematic showing orientation of transducer to caries scan sample, and location of each b-scan (numbered 1,2,3). 185
8.6 Ultrasonic A-scan of dental sample showing front face and enamel dentin junction (EDJ) reflections 186
8.7 Raw data waterfall plot of dental erosion sample. 187
8.8 Waterfall plot of dental erosion sample after correlation shifting. . 188
8.9 Annotated b-scan image of erosion sample. 189
8.10 Ultrasonic thickness measurements from b-scan data (a) and subsequent verification against the SGI method (b). Inset image in (b) shows the correlation relationship between the two techniques. 191
8.11 Three dimensional image of dental sample recorded using ultrasound. Image shows two views orthogonal to each other. 193
8.12 Ultrasonic B-scan (a) recorded at location '1' of sample depicted in Figure 8.5. Red dotted line shows location of pixel intensity profile shown in (b) 194
8.13 Ultrasonic B-scan (a) recorded at location '2' of sample depicted in Figure 8.5. Red dotted line shows location of pixel intensity profile shown in (b) 195

8.14 Ultrasonic B-scan (a) recorded at location '3' of sample depicted in Figure 8.5. Red dotted line shows location of pixel intensity profile shown in (b) 196